6-2013

Organic Solar Cells Based on High Dielectric Constant Materials: An Approach to Increase Efficiency

Khalil Jumah Tawfiq Hamam

ORGANIC SOLAR CELLS BASED ON HIGH DIELECTRIC CONSTANT MATERIALS: AN APPROACH TO INCREASE EFFECIENCY

by

Khalil Jumah Tawfiq Hamam

A dissertation submitted to the Graduate College
in partial fulfillment of the requirements
for the degree of Doctor of Philosophy
Department of Physics
Western Michigan University
June 2013

Doctoral Committee:

Clement Burns, Ph.D., Chair
Paul Pancella, Ph.D.
Guda Ramakrishna, Ph.D.
Asghar Kayani, Ph.D.

ORGANIC SOLAR CELLS BASED ON HIGH DIELECTRIC CONSTANT MATERIALS: AN APPROACH TO INCREASE EFFECIENCY

Khalil Jumah Tawfiq Hamam, Ph.D.

Western Michigan University, 2013

The efficiency of organic solar cells still lags behind inorganic solar cells due to their low dielectric constant which results in a weakly screened columbic attraction between the photogenerated electron-hole system, therefore the probability of charge separating is low.

Having an organic material with a high dielectric constant could be the solution to get separated charges or at least weakly bounded electron-hole pairs. Therefore, high dielectric constant materials have been investigated and studied by measuring modified metal-phthalocyanine (MePc) and polyaniline in pellets and thin films. The dielectric constant was investigated as a function of temperature and frequency in the range of 20Hz to1MHz. For MePc we found that the high dielectric constant was an extrinsic property due to water absorption and the formation of hydronuim ion allowed by the ionization of the functional groups such as sulphonated and carboxylic groups. The dielectric constant was high at low frequencies and decreasing as the frequency increase. Investigated materials were applied in fabricated bilayer heterojunction organic solar cells. The application of these materials in an organic solar cells show a significant stability under room conditions rather than improvement in their efficiency.

ACKNOWLEDGMENTS

I would like to show my gratitude to people whom I worked with during my studying period here in the United States. First, I would like to forward my thanks to my advisor and thesis committee chair, Prof. Clement Burns, for his unlimited advice, suggestions and comments. I would like to acknowledge my appreciation to Dr.Gellert Mezei, Dr. Ramakrishna Guda from the chemistry department and Dr. Asghar Kayani from the physics department for letting me work on their facilities and for providing professional discussions and collaboration opportunities that i really appreciate. I am also grateful to my colleagues Dr. Nasser Hamdan, and Mohammad Al-Amar, for their participation in the experiments and discussions.

I would like to express my sincere thanks to the department of physics for their financial support for the entire period of my study. Also I would like to thank Dr. Dean Halderson for his understanding and support as a graduate advisor; the physics department secretary Lori Krum; Rick Welch for making necessary parts for our experiments; Eng. Allan Kern for his prompt help with electrical and vacuum parts on our machines. I am very grateful to Dr. Paul Pancella for being on my committee. I would also like to thank Dr. Valery Bliznyuk for his help in AFM work.

I would like to express my deepest appreciation and love to my wife Lara Alhurani and my kids for their love and patience during this period of my life in the United States. Without their understanding and support, it would be impossible for me to do this work.

Finally, I would like to thank my mom, my brothers and sisters for their unrestricted sincere love and support.

Khalil Jumah Tawfiq Hamam

TABLE OF CONTENTS

Table of Contents—continued

CHAPTER

Table of Contents—continued

CHAPTER

Table of Contents—continued

LIST OF TABLES

LIST OF FIGURES

CHAPTER I

INTRODUCTION

Environment and energy issues have become one of the most important areas of concern these days; they are connected each other. The world energy consumption nowadays is ~4.1×10^{20} joules/yr; this is equivalent to 15 terawatts (TW). Nowadays power sources are 16% hydro, 12.9% nuclear and 3.7% for wind, biomass and photovoltaic sources, but 67% of today's world energy resources are from burning fossil-fuels coal and peat 40.6%, oil 4.6% and natural gas 22.2%.[1]

Environmental degradation has been caused by gases from burning fossil-fuel, including the greenhouse effect, smog, acid rain, etc. which threatens human health. In addition, fossil fuel resources on Earth will not last forever. Due to increasing need for energy supplies and the concern of environmental pollution, alternative renewable, environmentally-friendly, and sustainable energy sources are needed. The best source of clean, abundant energy is the sun. The sun deposits 120,000 TW of radiation on earth's surface, which is more than 10,000 times what we use. The sun is the main natural power source of our planet; it powers the photosynthesis cycle of plant life which is the main source of food for life on earth, the cycle of water in nature and global wind. Generating energy from the sun through the photovoltaic effect by converting sunlight into electricity using solar cells would be the best solution to overcome both environmental and energy demand problems.

For the past decades, inorganic semiconductors (ISs) such as silicon, germanium and gallium arsenide have been the backbone of semiconductors in general and the photovoltaic industry in particular; the high production cost and the need of large area coverage means their usage has been limited. [2, 3, 4, 5] Recently, organic semiconductors (OS) gained scholars attention because of their potential to replace ISs solar cells due to 1) their lightweight and 2) low-cost fabrication, so this

offers the ability to fabricate devices over large areas on various flexible substrate such as plastic and paper through employing inexpensive roll-to-roll processes.

Over the past two decades the performance of organic light-emitting diodes (OLEDs) has improved, but organic solar cells (OSCs) remain unused compared to inorganic solar cells (ISCs). Estimates predict that renewable energy sources included photovoltaic will provide 1-2% of the world energy consumption by 2020 and around 15% in 2050. [6, 7] This means that we need around 100,000 Km^2 of photovoltaic cells to cover this huge area, which cannot be achieved by conventional inorganic photovoltaic technologies.[8] OSCs have great potential to replace ISCs in many applications which require inexpensive fabrication and large area coverage like OLEDs and OSCs. [9]

The first organic solar cell exhibiting reasonable power conversion efficiency was fabricated by Tang in 1986 using a vacuum deposited phthalocyanine (CuPc) and perylene derivatives (3,4,9,10-Perylene tetracarboxylic-bisbenzimidazole (PTCBI)) under simulated AM2 (75mW/cm^2) illumination. A power efficiency of η=0.95% was recorded. [10] Since that time an extensive effort has been made by researchers and scholars to study different materials and to engineer photovoltaic devices to reach reasonable efficiencies. The highest PCEs reported for small molecules OPV cells, containing CuPc recorded 4.4% for bilayer heterojunction devices[11] and 5.7% in a tandem cell under standard sun simulator AM1.5 (100mW/cm^2) fabricated by Forrest *et al*, they also calculated the theoretical prediction of the small molecules power conversion efficiency, where it can achieve 6.5% using a tandem structure. [12] In general, small molecule materials have the potential of better efficiencies. Recently a tandem structure of small molecular weight materials reached 12% efficiency as reported by Heliatek GmbH Company. [13]

Device efficiencies around 6.5% at illuminations of 200 mW/cm^2 have been reported in 2007 by Kim *et al*. with stability of over 1000h, using a tandem cell. [14] In 2010 Konarka and Sony companies recorded 9.3%, and 9.9% efficiencies using a polymer and dye sensitized materials[15] with low lifetime stabilities ~ 1000h under continuous illumination (encapsulated cells). [16] But OSCs still lag behind ISCs which has efficiency around 25% for single crystal silicon (1999) with

a lifetime longer than 25 years. Crystalline GaAs (2010) recorded 26.4% and 42.3% for InGaP/GaAs/InGaAs (2-terminal) tandem cells. [15] This implies that a large effort is still needed to take OSCs technology from the lab to market.

1.1 Purpose of the study

In ISC devices, incident photons of the proper energy will promote an electron to the conduction band and leave a hole in the valence band (i.e. a free electron and hole). The electric field formed in the depletion layer at the p-n junction interface is sufficient to drive electrons and holes to their respective electrodes. In the case of OSC devices, the incident photon will excite the active layer creating a mobile excited state called an exciton (an electron-hole pair bound by their attractive coulomb interaction) rather than form a free electron-hole pair. Excitons are electrically neutral and unaffected by electric fields. If the exciton doesn't break up it will recombine due to its limited life time, and short diffusion length of 5-70 nm. [4, 8, 17, 18]

The main goal of this study is to fabricate an efficient OSC device using materials with suitable dielectric constant. Investigate existing materials with particular physical, optical and electrical properties, was our approach. A group of materials which already proved to have those characteristics are based on phthalocyanine and polyaniline. Materials were either synthesized by our group or purchased from major chemical distributers. A full picture of their electrical, optical, and physical properties under pellets, thin film will give us a full and clear understanding to reach our goal of making efficient solar cell competitive with conventional cells.

1.2 Thesis outline

The main goal of this work was increasing the efficiency of organic solar cells. Generally, organic solar cells suffer from low power conversion efficiency due to many reasons. The major reason is the low dielectric constant of organic semiconductors. The theoretical basis will be discussed in detail in chapter 2, where we also present a comparison between organic and inorganic semiconductors. Basic definitions, operating principle and characterization of both inorganic and organic photovoltaics, dielectric materials properties, polarization mechanisms and ac conductivity will be discussed in this chapter as well. In chapter 3, we discuss the existence of organic materials

with high dielectric constant; different materials based on metal phthalocyanine modified with carboxylic and sulphonic groups were investigated, in addition to hyperbranched CuPc (dendrimer CuPc). Polyaniline (PANI) was also studied, including its physical and optical properties and it was used for solar cells. In chapter 4, the experimental procedure is introduced, as well as the tools and instruments used through the investigation, in addition to fabrication and the characterization of our organic solar cells. In chapter 5, physical and optical properties for materials under investigation are covered. The fabricated organic solar cells results are discussed in chapter 6. Finally, the conclusion is in chapter 7.

CHAPTER II

BACKGROUND

Basic background about how photovoltaic cells work and characterize is an important step before proceeding to the rest of this work. A comparison between organic and inorganic semiconductors in terms of their structure and the types of photogenerated charge carriers is necessary to understand the organic and inorganic solar cells and to understand the purpose of this study. Finally, the basic definition of dielectric constant, polarization mechanisms and ac conductivity are discussed.

2.1 Photovoltaic effect

Photo-voltaic means “light-electricity”. Photovoltaic (PV) consists of two terms "photo" which comes from the Greek word "phos" which means "light" and "Volt" comes from the name of Alessandro Volta (1745-1827). The conversion of light energy into electricity using a device called a solar cell is the photovoltaic effect-see fig. 2.1.

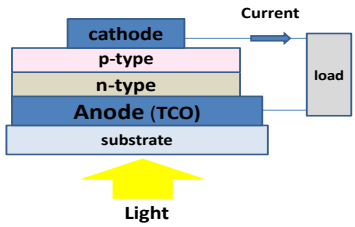

Figure 2.1 The photovoltaic effect, where TCO is the transparent conductive oxide.

In 1839 Edmond Becquerel demonstrated the first photovoltaic device; he discovered that an electrical current could be generated by exposing platinum electrodes covered with silver bromide in an aqueous solution to light. [19] However, to understand and explore this effect we need to usequantum mechanics. Solar cells respond to packets of energy called photons whose energy depends on their frequency. When the energy is sufficient to excite electrons into higher energy levels they will be free to move.

Another innovation, dependent on the first, is the development of semiconductor technology and science, which has been responsible for the electronics revolution and the photonics revolution. Photovoltaic energy conversion in solar cells consists of two major steps. First, absorption of light generates an exited state within the material. The electron and hole are then separated with electrons going to the cathode and holes going to the anode, generating electrical power. [20, 21]

2.2 Basics of photovoltaics

2.2.1 Solar spectrum

The solar absorption spectrum outside earth's atmosphere is shown in fig. 2.2. As sunlight is transmitted through the earth's atmosphere it changes due to absorption and scattering by certain atmospheric gases, mainly oxygen, ozone, water vapor, and carbon dioxide as well as dust which create dips in the absorption spectrum in certain wavelength regions.

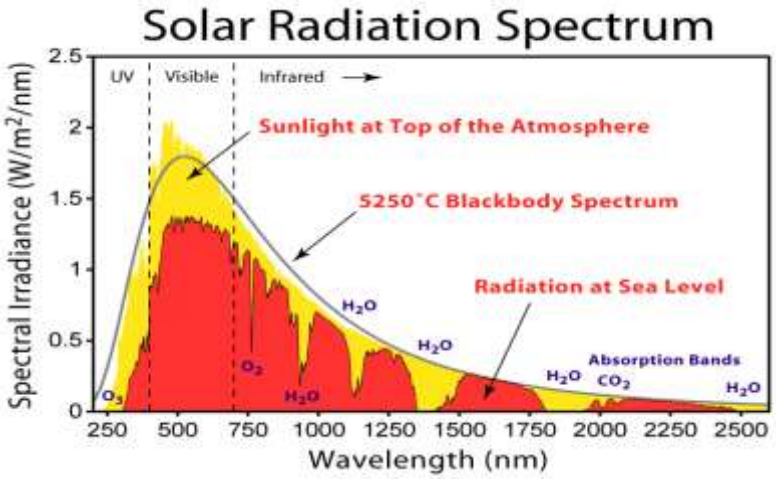

Figure 2.2 Solar absorption spectrum outside earth's atmosphere, at sea level and the blackbody spectrum at 5250 K. [22]

The amount of atmosphere that the light has to pass through before reaching the earth's surface is called the air mass (AM). The abbreviation (AM) followed by a numeric figure describes the spectrum obtained after passing through a certain air mass with a specific angle to the zenith. In the space outside the earth's atmosphere, the spectrum of the sun is undisturbed since there is no atmosphere. The integrated spectral radiance is 1366.1 W/m^2, and the spectrum is termed as AM0 according to the ASTM E490-00 standard (American Society for Testing and Materials).[23]AM factor is given by [21]

$$\mathbf{AM[number} = \frac{1}{\cos\theta}\mathbf{]} \tag{2.1}$$

Where θ is the angle the sun makes with the vertical line (the zenith angle) perpendicular to the horizontal plane (Fig. 2.3).

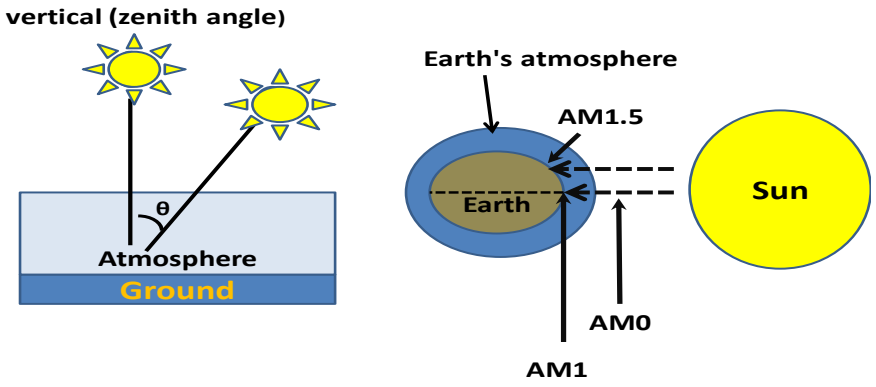

Figure 2.3 Illustration of AM0, AM1, and AM1.5.

The sun's spectrum is termed as AM1.0 when the sun light travels through the atmosphere to reach the surface of the earth and makes an angle of 0° with the zenith. At the higher latitudes most common in the Northern hemisphere like the United States, Europe and Canada, the sunlight has to travel longer distances through the atmosphere to reach the surface, and the air mass there is closer to AM1.5, which corresponds to a receiving surface tilted 37° toward the equator.

2.2.2 Equivalent circuit and power conversion efficiency [4, 5, 8 , 20, 21]

The real equivalent photovoltaic cell circuit is shown in fig. 2.4, where a potential difference has been developed across a load connected to the cell. This potential difference generates a current (J) in the opposite direction to the photocurrent (J_L), so the net current is reduced from its short circuit value. The reverse current is the dark current which flows across the device under bias voltage in the dark. Solar cells behave as diodes in the dark, where forward bias current (V>0) is much larger than the reverse bias current (V<0). For the dark current density J_D in an ideal diode

$$J_D = J_o(e^{qV_D/k_BT}-1) \quad (2.2)$$

Where J_0 is reverse saturation current, k_B is Boltzmann constant and T is the temperature in Kelvin.

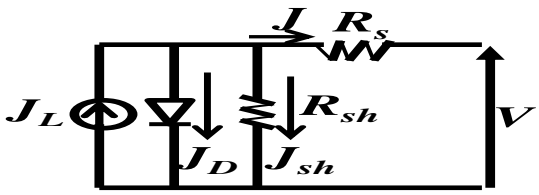

Fig. 2.4 Photovoltaic equivalent circuit where R_s represents the bulk resistance of the active materials and electrodes. R_{sh} represents the shunt resistance; J_{sh} is current across the shunt resistance.

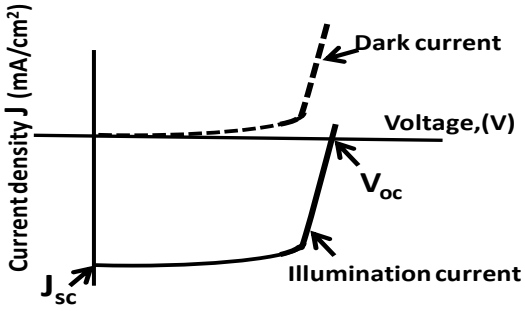

Figure 2.5 The J-V characteristic of the photovoltaic cell under illumination and when dark.

The total current density J in a real photovoltaic cell is given by

$$J = J_L - J_{sh} - J_D \tag{2.3}$$

$$J = J_L - J_{sh} - J_o(e^{qV_D/k_BT}-1) \tag{2.4}$$

$$J = J_L - \frac{V_D}{R_{sh}} - J_o(e^{qV_D/k_BT}-1) \tag{2.5}$$

but $V_D = V - J R_s$

$$J = J_L - \frac{V - J R_s}{R_{sh}} - J_o(e^{\frac{q(V-JR_s)}{k_BT}}-1) \tag{2.6}$$

The current–voltage curve for an ideal photovoltaic cell as in fig.2.5 when $R_s = 0$ and $R_{sh} \rightarrow \infty$ equation (2.11) becomes

$$J = J_L - J_o(e^{qV/k_BT}-1) \tag{2.7}$$

The maximum potential difference when the contacts are isolated will be the open-circuit voltage (V_{oc}); this is equivalent to when the dark current is equal to the photocurrent density (J=0). Equation (2.7) become

$$V_{oc} = \frac{k_BT}{q} \ln\left(\frac{J_L}{J_o} + 1\right) \tag{2.8}$$

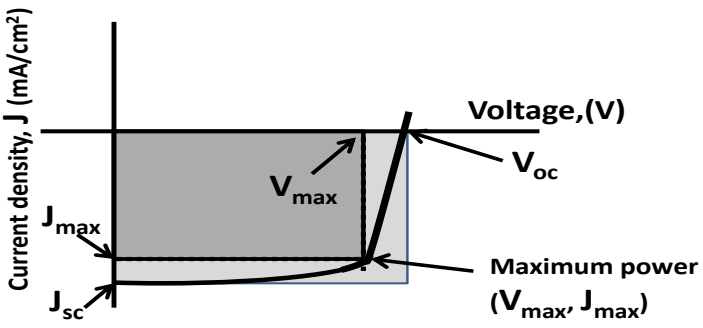

Figure 2.6 The open circuit voltage (V_{OC}), short circuit current (I_{SC}) and fill factor (FF).

The conversion efficiency (η) is defined as the ratio between the output power to the input power (the power in the light). The fill factor (FF) is defined as the ratio of the maximum possible

electrical power ($J_{max} \times V_{max}$) to the maximum theoretical electrical power output ($J_{SC} \times V_{OC}$). The maximum power point (P_{max}) of the cell (J_{max} , V_{max}) of the PV cell can be extracted from JV-curve by the maximum rectangle that can fit within the J-V curve (fig. 2.6)

$$\mathbf{FF} = \frac{J_{max}\, V_{max}}{J_{sc} V_{oc}} \tag{2.9}$$

$$\eta = \frac{P_{out}}{P_{in}} = \frac{FF \times J_{sc} V_{oc}}{P_{in}} \times 100 \tag{2.10}$$

2.3 Organic semiconductors

An intrinsic semiconductor can be defined as a material that is an insulator at absolute zero, but has a significant electrical conductivity at room temperature. The different between metals and insulators is given by band theory. Metals have a partially-filled conduction band (the valence and the conduction bands overlap or are partially full); an insulator is characterized by a filled valence band and an empty conduction band. The difference between a semiconductor and an insulator is not obvious but roughly speaking, a semiconductor is an insulator with a band gap small enough that its conduction band is significantly thermally occupied at room temperature. The most important thing about semiconductors is the ability to control their electronic properties by adding small amounts of chosen impurities, the doped semiconductors being known as extrinsic semiconductors.[41] In intrinsic semiconductors the Fermi energy level describes the equilibrium state of the electrons in the system, and it lies halfway between conduction and valence bands at absolute zero. The equilibrium concentrations of electrons and holes is [2, 21]

$$n_o = N_c\, e^{\frac{E_F - E_c}{KT}} \qquad\qquad p_o = N_v\, e^{\frac{E_v - E_F}{KT}} \tag{2.11}$$

If we set $n_o = p_o$, one can get

$$E_F = \frac{E_c + E_v}{2} + \frac{K_B T}{2}\, ln\left[\frac{N_v}{N_c}\right] \tag{2.12}$$

Where N_c and N_v are the effective density of states in the conduction and valence bands respectively, E_c and E_v are the energy of conduction and valence band respectively. While the doped semiconductor has localized energy levels close to the conduction (in the n-type doping) or valence (in the p-type doping) band edges as can be seen in fig. 2.7. As a result, the energy

required to promote an electron (a hole) to the conduction (valence) band is lowered to a level comparable with the thermal energy. The difference between intrinsic and extrinsic semiconductors is illustrated in fig. 2.7.

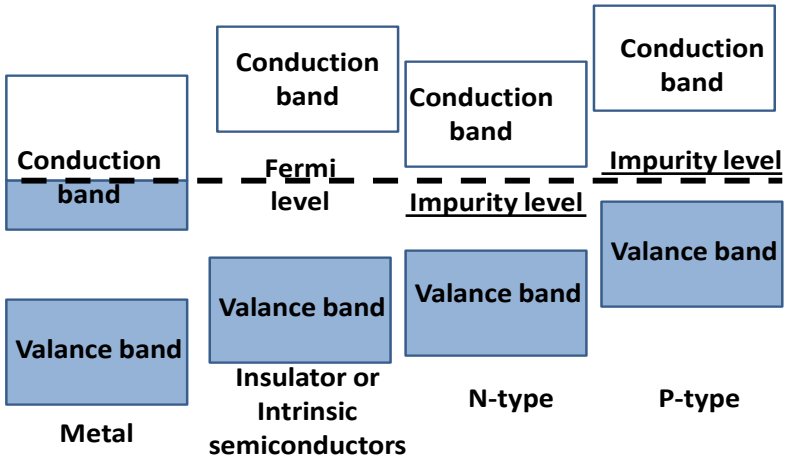

Figure 2.7 Energy levels for semiconductor, metals, and insulators.

In 1940 a new type of semiconductor was identified, the organic semiconductor. [3, 4] Organic semiconductors consist of two main types, low molecular weight materials (small molecules) and the large molecular weight materials (polymers). The electrical conduction of organic molecules originates from a delocalized π-bond generated from the overlap of the p_z orbitals. For example consider the basic ethylene (C_2H_4) molecule shown in fig. 2.8a. The sp^2 hybridization between carbon atoms form three co-planar σ-bonds (one with the other C atom and two with H atoms). In the σ-bond the electrons spend most of their time in the space between the two bonded atoms like C-C, that is why they are called localized electrons. The forth orbital p_z is perpendicular to the sp^2 hybridized orbital plane which leads to a π-bond between two neighboring carbon atoms. In a π-bond the electrons are moving in and out of the space between the two bonded atoms. The molecular orbitals split into bonding and anti-bonding states as in fig. 2.8b which are commonly

known as the highest occupied molecular orbital (HOMO) and lowest unoccupied molecular orbital (LUMO) respectively.

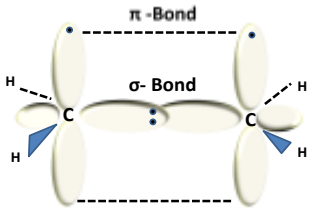

a

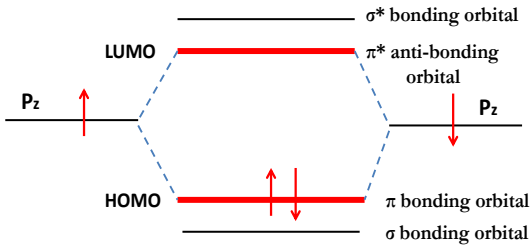

b

Figure 2.8 a) sp^2 hybridization in ethylene. b) Energy level splitting in the hybridized sp^2 states.

In the case of benzene there are six sp^2-hybridized carbon atoms and each sp^2-carbon has one unhybridized p-orbital containing one electron. These p-orbitals are close to each other so they overlap to form a π-bond. There are two modes for overlap of adjacent p-orbitals. Actually, each p-orbital overlaps equally with the p-orbital on two adjacent carbon atoms to form a donut shape, the π-electron cloud is above and below the plane of carbon and hydrogen atoms (fig. 2.9). The three π-bonds of benzene are another example of delocalized electrons.

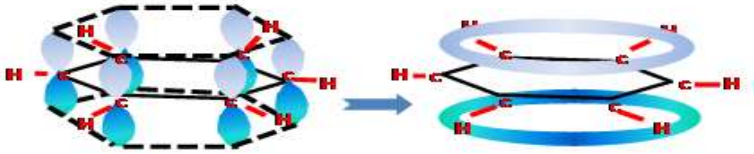

Figure 2.9 Delocalized electronic cloud in π-bonds of benzene distributed above and below the molecule plane.

The energy levels of organic materials can be linked to the energy levels of inorganic semiconductors as shown in fig. 2.10 The energy needed to promote an electron from the valence band of an inorganic semiconductor to the vacuum level is called the ionization potential, while the electron affinity denotes the energy gained when an electron transports from the vacuum level to the conduction band. Incident light with a suitable energy will promote electrons from valence band to conduction band as a free electron. On the other hand, in organic materials electrons can be prompted from the highest occupied molecular orbital (HOMO) to states lower than the lowest unoccupied molecular orbital (LUMO) called an exciton states. The main reason behind this is the Columbic attraction due to the low dielectric constant of organic molecules. The electronic bonds formed between the organic molecules are non-covalent. [5]

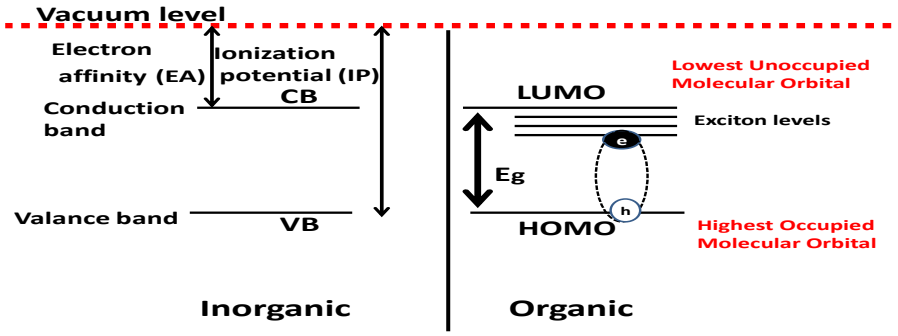

Figure 2.10 Energy level diagram for inorganic and organic semiconductors.

The optical absorption and charge transport in organic materials are dominated by partly delocalized π and π* orbitals. The optical absorption is narrow compared to the solar spectrum (visible region in blue or green areas, absorption in red or infrared is hard to reach).[4, 14, 24] The intra molecular Vander-Waals forces in organic solids are weak compared to bonds in inorganic crystals and much weaker than the intermolecular bonds. Therefore, electronic states are localized on each single molecule which forms narrow bands. Excitons do not transport any charge which means that they do not contribute to any electric currents (they do transport energy). The exciton type depends on the medium (dielectric constant) there are two major types of excitons, the Frenkel exciton (fig. 2.11a) which represents the strong Columbic attraction between the electron and hole, and this kind of exciton shows up on the same molecule. The other type is the Wannier exciton (fig. 2.11b) which represents the weak Columbic interaction, due to the high dielectric constant of the medium. This exciton extends over many molecules. [21, 41, 45]

Figure 2.11 a) Frenkel exciton and b) Wannier exciton represented by dashed circles (shaded circles represent atoms or molecules).

2.4 Organic solar cells

The first organic solar cell was sandwiched between two metal electrodes of asymmetric work functions.[24] Those devices had efficiencies less than 1% due to poor free-charge generation. Fig. 2.12 shows the simple energy structure of single layer organic solar cell, when two metals of different work functions are in contact. Exchange of holes and electrons begins until it reaches equilibrium. This exchange of holes and electrons takes place only in a small nanometer layer thick

unlike the depletion layer in the inorganic solar cell which can be microns. This layer will create an electric field extending through the film, causing the vacuum level of the organic material to be bent as shown in fig. 2.12. Consequently, photo-generated carriers are driven by the potential gradient to their energetically favorable electrode. But unfortunately, diffusion length of the generated excitons is small and the internal electric field is not strong enough to overcome the Coulomb attraction of the bound electron-hole pairs.

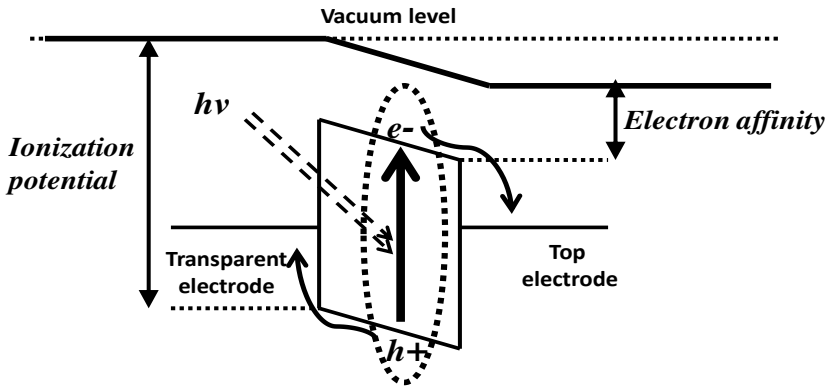

Figure 2.12 Energy structure of single layer organic solar cell.

Therefore, to dissociate excitons, the donor-acceptor (D-A) bilayer heterojunction concept was introduced by Tang in 1986. It leads to a significant improvement in the OPV cell efficiency since the recombination of excitons is reduced significantly. Tang's cell had the simplest structure for a bilayer organic solar cell which consists of a material with a low ionization potential (IP) given by the highest occupied molecular orbital (HOMO) level, called the donor, and a material with a large electron affinity (EA) given by the lowest unoccupied molecular orbital (LUMO) level, called the acceptor. Another type of OSC is the bulk heterojuction cell where active materials are blended together to form a continuous interpenetrating network to maximize the interface area. The phase separation is 10-20nm, which is generally less than or equal to the exciton diffusion length. To

obtain a high conversion efficiency of solar energy into electricity five successive processes should be occur:

(1) Absorption of incident light by donor material (photon absorption efficiency η_A) which promotes the electron to an excited state (exciton formation), the exciton in the donor material has an energy E_{ex} which is smaller than the HOMO–LUMO gap (E_{gap}). To achieve good absorption, the material absorption spectrum must match the solar emission spectrum and the active layer must have enough thickness to achieve complete absorption. Fortunately, the absorption coefficient for organic materials in general is very high ($>10^5$ cm^{-1} for CuPc) covering the visible region of the spectrum which means that 100nm thickness is enough to absorb the light (reduce the light intensity to 1/e times its original value using the Lambert-Beer law). [4, 45, 88]

(2) Exciton diffuses to the donor-acceptor (DA) interface (exciton diffusion efficiency η_{ED}); otherwise the electron-hole pair will decay (recombine) radiatively or (usually) non-radiatively.

(3) Exciton separation at DA (charge-transfer efficiency η_{CT}). In this process an electron is transferred from an electron donor (D) (small electron affinity) material to an electron acceptor (A) (high electron affinity). The difference between both electron affinity levels (Δ_{LUMO}) is the energetic driving force required for successful exciton dissociation which should be larger than the binding energy of the exciton. In a p-n silicon semiconductor under illumination, electrons flow from the p-type to the n-type semiconductor; in the same manner, under illumination of an organic heterojunction bilayer, electrons flow from the donor layer to the acceptor layer. Therefore the donor layer is denoted as the p-type layer and the acceptor layer as the n-type layer similar to a silicon p-n junction. Materials with a low ionization potential are p-type materials, while those with a high electron affinity are regarded as n-type.

(4) Charge transport to their respective electrodes: the electrical potential gradient present at the interface of a p-n junction (the band bending) is able to separate the photo-induced electrons from the holes effectively. In contrast to IPV cells in organic solar cells, after the charge transfer the electrons and holes are in close proximity to the interfacial area. Therefore there is a large

chemical potential gradient that drives the charge carriers away from the exciton dissociating interface. Separated electrons and holes continue their trip to be collected at electrodes.

(5) Charge collection (charge collection efficiency η_{CC}): Each of above steps contributes to the total quantum efficiency of the solar cell through the ratio of the electron generated (photocurrent) through the cell to the incident photons on the cell which called the external quantum efficiency η_{EQE}:

$$\eta_{EQE} = \eta_A \times \eta_{ED} \times \eta_{CT} \times \eta_{CC} \quad (2.13)$$

Fig. 2.13 shows the basic operation of OPV bilayer heterojunction cell.

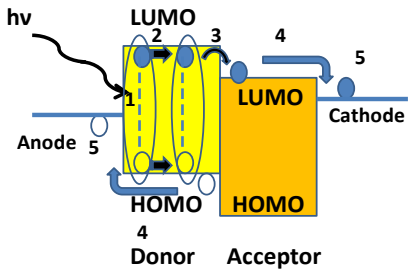

Figure 2.13 The operation of OPV cells 1) light absorption 2) exciton diffusion 3) charge dissociation 4) charge transport 5) charge collection.

2.5 Inorganic (conventional) photovoltaic devices

Photovoltaic cells have been extensively studied since 1954, when the first single crystalline silicon solar cell was reported by Chapin at Bell laboratories [2], with an efficiency of 6%. The efficiency has reached 24% for crystalline silicon solar cells, which is close to the theoretically predicted maximum value of 30%. [4, 8] Crystalline silicon solar cells are the prevailing type of silicon based solar cells compared to polycrystalline, single-crystal, and amorphous thin-film devices.

Practical conventional solar cells are made of a p-n junction. The p-type has an excess of the positive charges (holes), and were doped using materials like boron, while the n-type has an excess

of the negative charges (electrons), and were doped using materials like phosphorous. When p-type and n-type are in contact carriers begin to diffuse from region of high concentration to lower concentration. Holes from the p side migrate to the n side, since there are fewer holes than in the p side, while electrons from the n region migrate to the p side, where there are fewer electrons. As the migration continuous they leave behind the ionized impurities (dopants). An internal electric field created by the ionized impurities causes migrated carriers to drift back at the same rate as they diffuse away until the diffusion stop. A thin layer of high potential gradient region forms, called the depletion region as shown in the fig. 2.14. Electron and holes formed from light absorption are directed by the electric field towards the proper electrode.

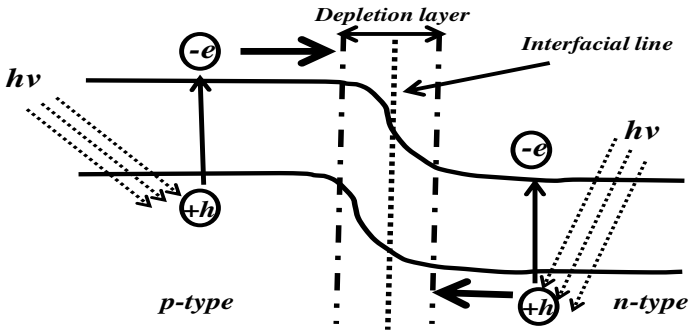

Figure 2.14 The p-n junction structure in the conventional PV cell.

2.6 Comparison between inorganic semiconductor (IS) and excitonic semiconductor (ES)

2.6.1 Charge transport

In IS the strong coupling between the constituting atoms and the long-range order lead to the delocalization of the electronic states and the formation of allowed valence and conduction bands, separated by a forbidden gap. ES which are usually organic semiconductors where the intermolecular forces (Van-der Waals force) are weak. These organic semiconductors typically have narrow energy bands, the highest occupied molecular orbital (HOMO) and the lowest unoccupied molecular orbital (LUMO), the molecular LUMOs and HOMOs do not interact

strongly to form a valence and conduction bands. Thus charge transport proceeds by hopping between localized states, rather than transport within a band. This means that charge carrier mobility in organic semiconductors is several orders of magnitude lower than inorganic semiconductors. [4, 9, 16]

2.6.2 Charge separation mechanisms

In ISs, photon absorption produces a free electron and a hole directly as shown in fig. 2.15a, while electrostatically bound charge carriers (excitons) are formed in ES. The exciton binding energy which is roughly the energy required to separate the electron from the hole ranges from 0.4–1.6 eV, [25] and is much higher than room temperature energy (k_BT=25 meV) [20, 21, 37, 41] as shown in fig. 2.15b.

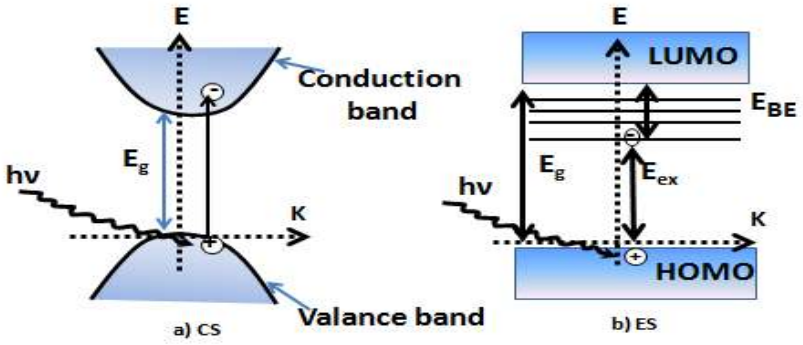

Figure 2.15 a) Photoexcitation in IS forming free charge carriers and b) in ES where an exciton forms rather than free charge carriers.

An exciton can be modeled as a positronium or a hydrogen-like atom.[4, 9, 37, 41, 26, 27, 28, 29, 30] The interaction between electron and hole can be described by the Schrödinger equation assuming an isotropic homogenous semiconductor material,

$$\left(-\frac{\hbar^2}{2M}\nabla_R^2 - \frac{\hbar^2}{2\mu}\nabla_r^2 - \frac{e^2}{4\pi\varepsilon_o\varepsilon\, r}\right)\Psi(R,r) = E\Psi(R,r) \qquad (2.14)$$

Where $r = r_e - r_h$ and $R = (m_e r_e + m_h r_h)/M$; M is the total mass $M = m_e + m_h$ and μ is the reduced effective mass of the electron (m_e) and the hole (m_h) system which is given by $\mu = \frac{m_e m_h}{m_e + m_h}$. By separation of the relative motion of the electron–hole pair and the motion of the center of mass we get the exciton binding energy levels:

$$E_{BE}^{n} = \frac{\mu e^4}{2\hbar^2 n^2} \frac{1}{\varepsilon^2} \tag{2.15}$$

The total exciton energy can be written as:

$$E_{ex} = E_g - E_{BE} \tag{2.16}$$

For the ground state, in terms of the Rydberg constant the exciton binding energy can be written as:

$$E_{BE} = R_y \frac{\mu}{m_o} \frac{1}{\varepsilon^2} = 13.6 \frac{\mu}{m_o} \frac{1}{\varepsilon^2} \text{ (eV)} \tag{2.17}$$

And the average distance between a bound electron-hole pair (excitonic Bohr radius) is given by:

$$r_B^{ex} = \frac{(4\pi \varepsilon_o \varepsilon \hbar^2)}{\mu e^2} = r_B \frac{m_o}{\mu} \varepsilon \tag{2.18}$$

Where ε is the dielectric constant of the surrounding medium, m_o is the mass of a free electron in a vacuum, and r_B =0.529A° is the Bohr radius for hydrogen atom.

Material	ε dielectric constant	m_e electron effective mass*	m_h hole effective mass*	μ reduced mass*	r_e^{ex} (A°) excitonic Bohr radius	Lattice constant (A°) At 300K	E_{BE} binding energy (meV) calculated	E_{BE} binding energy (meV) measured
Silicon(Si)	11.7 [41]	0.2 [41]	0.4 [26]	0.13	47.7	5.4 [30]	13.2	9.3 [41]
Germanium (Ge)	15.8 [41]	0.1 [41]	0.2 [26]	0.06	139.6	5.6 [30]	3.2	1.8 [41]
Gallium Arsenide (GaAs)	12.9 [35]	0.067 [29]	0.45 [29]	0.06	114	5.6 [29]	4.9	4.2 [31]
Copper-phthalocyanine (CuPc)	3.4 [32]	2.2 [33]	6.6 [33]	1.65	1.1	a=4 b=12.9 c=12 [34†]	1900	600 [35]

Table 2.1 Values of excitonic Bohr radius and ionization energy of electron-hole system to reach the continuum level for different materials. (* in terms of m_0, † ***α***–CuPc).

From table 2.1 the ionization energy of inorganic materials represented by silicon, germanium and gallium arsenide are less than the thermal energy, and the large excitonic Bohr radius of their wave function is more than the lattice constant, so that those materials in general have a Wannier exciton unlike organic materials, e.g., CuPc which has a Frenkel exciton. From equations (4) and (5) we can conclude that exciton binding energy and excitonic Bohr radius depend on:

a) **The dielectric constant (ε)**, where ε determines the magnitude of the coulomb interaction between electron-hole pairs and charge carriers as well as any fixed ionic charges in the lattice (screening effect). Equation (4) shows that **dielectric constant is more important due to it being squared,** as compared to the effective mass which has an exponent of one.

b) The effective mass, in IS is usually less than the mass of a free electron in vacuum but the effective mass in ES is greater than a free electron[6]. Effective mass decreases as the carrier becomes more delocalized and its transport becomes more wavelike.

To make organic materials behave like inorganic ones, the dielectric constant has to increase and the effective mass decrease. By doing simple calculations for CuPc molecule, we found out that the value of ε to have weaker attraction than thermal energy is ~17. Organic material based on the metal phthalocyanines with values of dielectric constant close to or higher than 17 have already synthesized by different scholars and measured in our lab.

Equations (1.4) and (1.5) are a rough approximation for several reasons: EC conduct mainly through π-orbitals rather than σ-orbitals. [3] So, they are low-dimensional materials: conductivity along one axis is often different than other axes.[32] Therefore, the parameters ε and effective mass do not have the spherical spatial symmetry implied by the derivation of above equations.

A tensor representation instead of a simple algebraic equation is needed for an accurate description for ESs. [29]

2.7 Properties of dielectric materials

2.7.1 Dielectric constant (relative permittivity)

The dielectric constant (ε) or relative permittivity of a material is the ratio between the permittivity of the material ε_m to that of the vacuum ε_0.

ε is related to the susceptibility by using the definition of electric displacement D and polarization P through:

$$D = \varepsilon_0 E + P = (1+\chi)\, \varepsilon_0 E \equiv \varepsilon_m \varepsilon_0 E \equiv \varepsilon E \quad (2.19)$$

Where $\varepsilon_m = 1+\chi$, $\varepsilon = \varepsilon_m/\varepsilon_0$, $\varepsilon_0 = 8.85\times10^{-12}$ F/m is the permittivity of vacuum, and E is the external (applied) field.

ε is a function of temperature, frequency and material structure.

$$\varepsilon(T,\omega) = \varepsilon'(T,\omega) + i\,\varepsilon''(T,\omega) \quad (2.20)$$

Where ε′, ε″ are real and imaginary parts of dielectric constant respectively and $\omega = 2\pi f$.

2.7.2 Dielectric loss tangent (dissipation factor)

The dissipation factor (tanδ) is the power dissipated in the sample. It is described in terms of the ratio of the imaginary part (ε″) to the real part (ε′) of the complex dielectric permittivity as:

$$\tan\delta = \boldsymbol{\varepsilon''/\varepsilon'} \quad (2.21)$$

For high device performance (higher efficiency and lower noise) a low dielectric loss is desired. Moreover, the frequency and temperature dependence of the dielectric loss provide important information on the charge transfer mechanisms operative in the materials.

2.8 Frequency dependent of dielectric constant (polarization mechanisms)

The electric polarization (dipole moment per unit volume; P) is the ability to respond to an applied electric field. The electric dipole moment can be induced in non-polar materials by the electric field or be permanent as in polar molecules. There are several microscopic mechanisms of polarization in a dielectric material which depend on the time variation of the electric field. [36, 37, 39]

2.8.1 The electronic polarization P_e (optical polarization)

The first type of polarization mechanisms is the electronic polarization P_e (optical polarization), which describes the displacement of the cloud of bound electrons with respect to the nucleus under an applied electric field. The electronic polarization mechanism is present in all atoms and covers a wide frequency range up to 10^{15} Hz. The time required to induce the electronic polarization is ~ 10^{-15} sec. The electronic polarization of one atom is given by: [38]

$$P_e = \alpha E = (4\pi\varepsilon_0 a^3) E = (3\,\varepsilon_0 V) E \quad (2.22)$$

Where α is the polarizability, a is the atom radius, and (V) is the atom volume.

2.8.2 The ionic polarization P_i

The ionic polarization P_i relates to the stretching or compressing the bond length by the electric field which changes the dipole moment of the molecule, it is operative up to infra-red frequency (10^{12}-10^{13} Hz) so its time response is slower compared to the first type. Ionic polarization is present only in materials made of two or more different kinds of atoms that form ions due to the sharing of the valence electrons. Since the response time for electronic and ionic polarization is so short they are considered as constant for all frequencies from 0 to about 10^{12} Hz and they are classified as induced dipole moments by electric fields. Ionic polarization is [39, 40, 60]

$$P_i = \alpha_i E = \{(Zq)^2 / (M_r (\omega_o^2 - \omega^2) - i\beta\omega)\} E \quad (2.23)$$

And for static field (ω=0)

$$P_i = ((Zq)^2 / M_r \omega_o^2)) E \quad (2.24)$$

Where M_r is the reduced mass, q is the electric charge; β is a damping or retarding force constant and ω_0 is the natural (lattice vibration) frequency.

2.8.3 The orientational polarization P_o (dipole polarization)

Orientational polarization P_o (dipole polarization) can be found in materials with an asymmetrical structure where randomly oriented permanent dipoles can be created in the absence of electric field. When an external electric field is present they have freedom to rotate and align with the field. Such phenomena exist in gases, liquids, and polymeric materials. It operates up to microwave frequencies (10^8 Hz), and its temperature dependence is, according to the Debye equation[39, 40]

$$P_o = N \frac{2\mu_s^2}{3k_B T} E \quad (2.25)$$

Where μ_s is the permanent dipole moment, N the number of molecules per cubic meter and E is the applied electric field.

Generally, orientational polarization is much larger than electronic or ionic polarization. Due to its temperature dependence, it can be easily distinguished from electronic or ionic polarization by the temperature dependence of the dielectric constant.

2.8.4 The interfacial polarization (space charge) P_{sc}

Interfacial polarization (space charge) arises as a result of local charge accumulation as they drift through the material. Charge carriers (electrons, holes, or ions), which may be injected from electrical contacts, may be trapped in the bulk or at interfaces. Generally it occurs at boundaries, inter-phase boundaries, and surfaces, where dipoles can orient to a certain degree under an electric field and contribute to the total polarization of dielectric materials. A lot of dielectric materials have very high dielectric constant at lower frequencies; the interface polarization contributes to the total polarization in low frequencies up to 10^4 Hz. [60, 39, 41]

Spontaneous polarization mechanisms occur only in single crystals or in polycrystalline materials whose crystalline structure exhibits electrical order. It is a fundamental characteristic of ferroelectric materials [35, 42] where electric polarization occurs spontaneously due to a phase transition in crystal structure where it change from non-polar to a polar structure as in $BaTiO_3$ at a critical temperature called the Curie temperature (T_c). The physical significance for these materials is that they possess a very high dielectric constant at temperatures $\leq T_c$ while above T_c the dielectric constant becomes normal. [39, 40] Upon the removal of the field, spontaneous polarization does not vanish but remains inside the material. The field polarization relation forms a hysteresis loop like to the hysteresis loop for ferromagnetic materials. Pohl and Hartman *et al*.[47] reported another type of mechanism called hyperelectronic polarization which has been found in long polymeric molecules which have an extensive region of electronic orbital delocalization due to pliant interaction of charge pairs of excitons. This type is active up to frequencies of MHz.

The total polarization of a medium under the effect of varying electric field can be given generally by:

$$P = P_e + P_i + P_o + P_{sc} \tag{2.26}$$

Note that we can add the spontaneous polarization mechanism to the net polarization if the material is a ferroelectric material. Fig. 2.16 is a summary schematic diagram where the relative magnitudes of different polarization mechanisms are shown. The lowest value of the dielectric constant is for P_e, the highest contribution is for P_{sc}, and P_o. The dielectric constant values depend

on the physical structure of the material and the symmetry of the molecules. From the figure we can notice the small contribution of ionic polarization P_i compared to space charge or orientational polarizations. At low frequencies we can see the contribution of all the polarization mechanisms, so the dielectric constant value is high because there is enough time to respond to the electric field. As the frequency increases the dielectric constant decreases as the relaxation time of the molecules is not able to follow the frequency of the field (it lags behind it) due to the inertia of molecules and ions. [24]

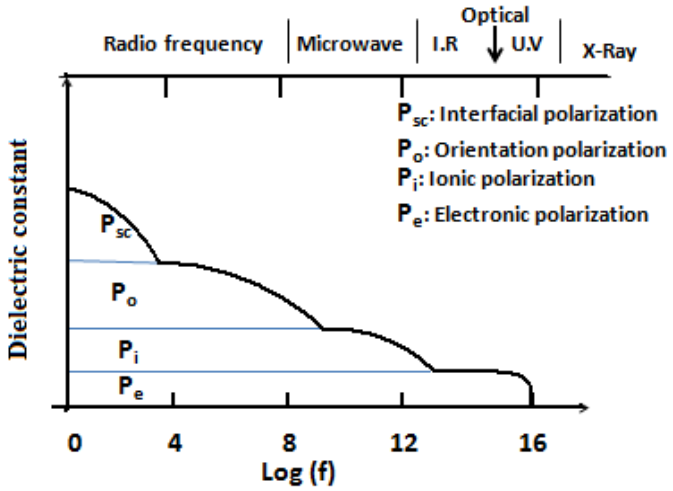

Figure 2.16 The frequency dependence of the dielectric constant and the polarization mechanisms.

2.9 AC conductivity

When he was doing his experiments, Johnscher [43] observed that the frequency-dielectric loss curves have the same behavior for a large number of polymers and materials; he came up with an empirical formula called the universal dielectric response "UDR" which is supposed to be applicable for all dielectric materials.

$$\sigma(\omega) = A\omega^{s} + \sigma_{dc} \qquad (2.27)$$

Where A is a constant and s is a frequency factor ($0 < s < 1$) s values depend on the material type; equation 2.27 shows how the electrical conductivity is described by two parameters one is the frequency independent dc conductivity and a frequency dependent term.

To understand the UDR, we should start from basic relations and definitions, equation 2.20

$$\varepsilon(\omega) = \varepsilon_\infty\{1 + \sum_\alpha \chi_\alpha{}'(\omega) - i\,\chi_\alpha{}''(\omega)\} \tag{2.28}$$

Where $\chi_\alpha(\omega)$ is the susceptibility contribution of various polarization mechanisms that play a role in the material, we can obtain the dielectric response at certain frequency like high frequency which commonly called as "fast" process frequency as

$$\varepsilon(\omega) = \varepsilon_\infty + \varepsilon_\infty[\chi'(\omega) - i\,\chi''(\omega)]$$

$$\varepsilon(\omega) = \varepsilon_\infty + \varepsilon_\infty\chi^*(\omega) \tag{2.29}$$

The response to sinusoidal excitation is given by the frequency-dependent dielectric susceptibility which is the Fourier transform of the response function f (t) which defines the time of the discharging current on sudden removal of the field

$$\chi^*(\omega) = \chi'(\omega) - i\,\chi''(\omega) = \int_0^\infty f(t)e^{-i\omega t}\,dt \tag{2.30}$$

The most basic form of the response function is that of independent non-interacting polarizing entities having the same, time-independent probability of relaxation from the stressed condition and thus satisfying the following differential equation:

$$\frac{dN}{dt} = -N/\tau \tag{2.31}$$

Where τ is a characteristic relaxation time, and is normally activated thermally with an activation energy E:

$$\tau = \tau_\infty \exp\left(\frac{E}{k_B T}\right) \tag{2.32}$$

The Fourier transformation for this function is given by

$$\chi^*(\omega) = \chi'(\omega) - i\,\chi''(\omega) = \frac{A}{1+i\omega\tau} = A\frac{1-i\omega\tau}{1+\omega^2\tau^2} \tag{2.33}$$

where A is a constant. This equation is known as the Debye dielectric relaxation in the frequency domain in a homogeneous material. From this equation we note that the ratio

$$\frac{\chi''(\omega)}{\chi'(\omega)} = \omega\tau \tag{2.34}$$

The most common formula used in terms of complex dielectric constant $\varepsilon*$ is

$$\varepsilon^*(\omega) = \varepsilon(\infty) + \frac{\varepsilon(0)-\varepsilon(\infty)}{1+i\omega\tau} \tag{2.35}$$

Where ε(0) and ε(∞) represent the static (relaxed) and high frequency (un-relaxed) values of dielectric constant we can rewrite 2.34 into its real and imaginary parts

$$\varepsilon'(\omega) = \varepsilon(\infty) + \frac{\varepsilon(0) - \varepsilon(\infty)}{1+\omega^2\tau^2} \tag{2.36}$$

$$\varepsilon''(\omega) = \frac{[\varepsilon(0) - \varepsilon(\infty)]\,\omega\tau}{1+\omega^2\tau^2} \tag{2.37}$$

which indicate that the loss is proportional to the frequency. We note this behavior for the ideal dielectric response of an isolated permanent dipole in a viscous medium, but Johnscher found experimentally that measurements for dielectric response do not follow "the ideal" Debye response. Instead, he found a fractional power law in time and in frequency.

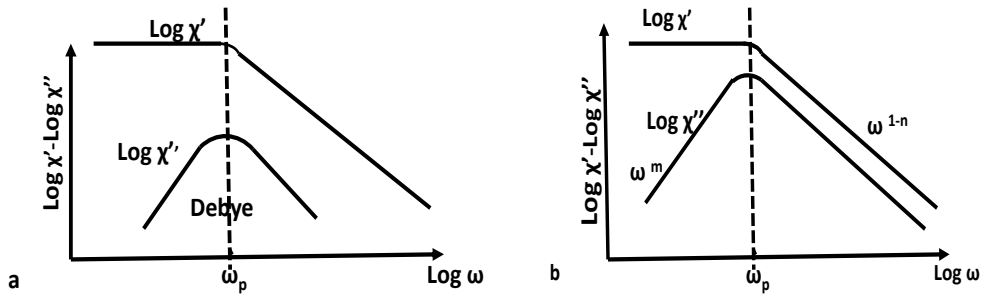

Figure 2.17 General dielectric response curves of a) an ideal Debye response and b) "UDR" behavior in dipolar materials. [40, 43]

Fig. 2.17 shows the general shape of the dielectric response of dipolar materials showing the two slopes m and 1-n. The peak frequency ω_p, and the shape of the ideal Debye response. In general, the dipolar response is showing a broader maximum than the Debye curve (symmetric and narrow about ω_p) and is given by two fractional power laws nearby the loss peak ω_p, at low frequencies $\omega \ll \omega_p$

$$\chi''(\omega) = \tan\left(\frac{m\pi}{2}\right)[\chi(0) - \chi'(\omega)] \propto \omega^m \tag{2.38}$$

Where 0<m<1and $\chi(0)$ is the limiting constant factor as $\omega \longrightarrow 0$, at high frequencies $\omega \gg \omega_p$ we have the UDR

$$\chi^*(\omega) \propto (i\omega)^{n-1} = \left[\sin\left(\frac{n\pi}{2}\right) - i\cos\left(\frac{n\pi}{2}\right)\right]\omega^{n-1} \quad (2.39)$$

With 0< n <1, we can rewrite the relationship between the imaginary part to real one as

$$\frac{\chi''(\omega)}{\chi'(\omega)} = \cot\left(\frac{n\pi}{2}\right) \quad (2.40)$$

The exponent either remains constant or decreases slightly with increasing temperature and the range mentioned is believed to suggest hopping of charge carriers between sites. The real part of the dielectric constant also increases due to conductivity. The increase in dielectric constant at low frequencies or high temperatures is possibly due to the hopping charge carriers and a much larger increase is attributed to the interfacial polarization (space charge).

The physical description related to hopping charges between two localized sites can be explained using fig. 2.17. A positive charge Q occupying site A can jump to the adjacent site B which is located at a distance d. The frequency of jumps between the two sites is the Debye relaxation frequency $1/\tau_D$ and the loss resulting from this mechanism is given by Debye equation for ε" (equation 2.37) where τ_D is a thermally activated parameter (equation 2.32).

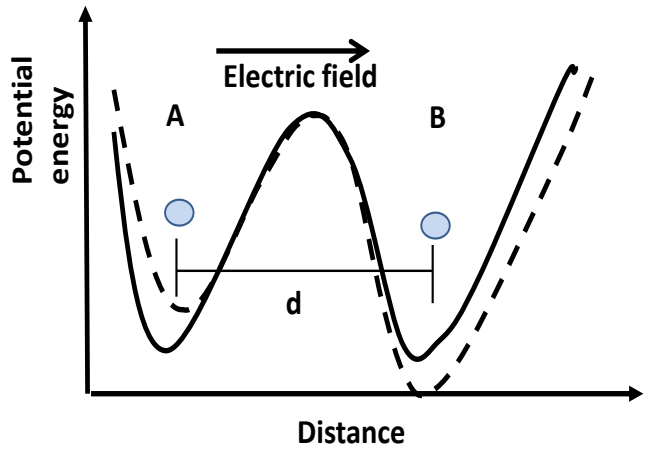

Figure 2.18 Hopping between two potential wells A and B, when the electric field is absence (the solid line) the charge spends equal time in each well. But when the electric field is applied, the wells are tilted to the direction of the field (the dashed line).

Let charge in site A be the source of potential; this potential repels charges having the same polarity and attracts those of opposite ones. In a solid the localized charges are not completely free to move, so the screening effect wouldn't be complete. The screening effect will reduce the effective charge under consideration due to the existence of the repulsive force between sites with the same polarity.

Now let's assume that the charge has already jumped to site B at t= 0. The screened charge is still at site A and the initial polarization is $P_0 = Qd$. The screening readjusts itself over a time period t; the time required for this adjustment is a relaxation time τ. As long as the charge remains in its new site longer than the relaxation time as defined in the above scheme, ($\tau < \tau_D$), there will be an energy loss in the system. The screening effect cannot follow instantly the hopping charge but reaches a time averaged occupancy between the two sites. The electric field affects the occupancy rates; site A occupancy will be reduced while site B will increase. The final value of polarization is accompanied by an energy loss. Materials obey the universal law of relaxation when a) charges hop over a distance of several sites, not over just adjacent sites, and b) charge screening can only adjust slowly to the rapid hopping. In crystalline and amorphous solids, the molecules are not completely free to change their orientations but they must assume a direction dictated by the presence of dipoles in the vicinity. Since the dipoles have finite length in real dielectrics they are more fixed, as in the case of a side group attached to the main chain of a polymer. These dipoles operate as if they are pinned at one end rather than completely free to be oriented. The swing of the dipole about its pinned axis is equivalent to the hopping of charge.

There are two different types of hoping mechanisms mentioned by Jonscher, by which the localized charges contribute to dielectric relaxation. In the first mechanism, the applied voltage results in a delayed current response which is explained in terms of the delayed release of localized charges to the appropriate band where they take part in the conduction process. If it was an electron it is released to the conduction band; and if it is a hole, then it is released to a valence band. The second mechanism is where the localized charge may just be transferred by hopping to another site when the field is applied, but not involving the conduction band or valence band

according to the two potential well's model described earlier. The hopping mechanism from site to site may extend throughout an interconnected network formed by these sites where charges can follow. The easier jumps because of the small distance between sites contribute to the dielectric relaxation while the more difficult jumps contribute to the conduction. This picture of hopping charges contributing both to the dielectric relaxation and conduction is considered possible because of the semi-crystalline and amorphous nature of practical dielectrics. With increasing disorder the density of traps increases and a completely disordered structure may have an unlimited number of localized levels. The essential point is that the dielectric relaxation is not totally isolated from the conductivity.

CHAPTER III

MATERIALS UNDER INVESTIGATION

Our endeavor to fabricate efficient organic photovoltaics based on an organic materials with high dielectric constant started with metal phthalocyanine materials reported by different scholars as a tetramer or oligomer metal phthalocyanine where the dielectric constant recorded was $>10^3$ at low frequencies. Dendimer or hyperbranched CuPc as it is called by T. Godson's group from University of Michigan where the dielectric constant was stable (constant) ~47 for the frequencies from 20 Hz to 1 MHz was the most promising choice to achieve our goal. The last material under investigation was the mixture of polyaniline (PANI) with CuPc_TS trying to improve the medium dielectric constant by adding PANI-salt.

Investigated materials were either synthesized by our collaborators in the chemistry department or purchased from major chemical suppliers like Alfa Aesar or Sigma Aldrich.

3.1 Metal phthalocyanine materials

Since 1948 when Eley discovered the semiconducting property of the phthalocyanines (Pc's), [44] these compounds have become one of the most investigated organic semiconductors, [45] due to their high chemical and thermal stability as well as electrical properties; they have found many applications in fuel cells, [46, 47, 48] organic photovoltaics, [49, 50, 51] organic field effect transistors (as a gate dielectric), [52, 53] humidity and chemical sensors, [54, 55] and electro-active polymers as actuators ("artificial muscles" in micro fluidic systems for drug delivery). [56, 57, 58] Pc's electronic and optical properties can be tuned by substituting the central metal atom, the axial and peripheral group, as or by adding dopants and varying the polymerization condition. Pc's can have many different metal atoms at the center of the molecule, in which case they are called metal phthalocyanines (MePcs). One of the most widely studied MePcs is copper phthalocyanine (CuPc) which is shown in fig. 3.1. The CuPc molecule does not have a dipole moment because of its symmetry, however the large

delocalization of the π-electrons within the phthalocyanine ring leads to a high electronic polarizability of 1.2×10^{-22} cm^3, which enhances the dielectric constant. [22] It has been suggested [37a, 59]that extrinsic factors may cause the giant values of the dielectric constant, including water uptake, [18] oxygen exposure, [60] treatment by different solvents, [16, 19] and relative orientation of Pc molecules when exposed to an external electric field. [61, 62, 63] It has already been shown that extrinsic factors can produce high values of the dielectric constant in inorganic semiconductors.[64]

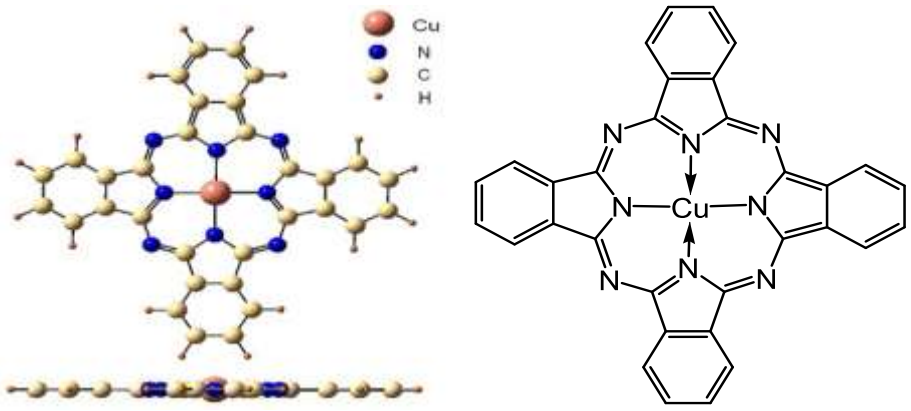

Figure 3.1 Standard CuPc structure.

Since Nalwa *et al*. reported the existence of what was assumed to be a CuPc "tetramer" [65a] (fig. 3.2) these materials received much attention due to their potential in many applications. Nalwa's group studied different metal-phathlocyanine (Cu, Co, Zn, and Fe) "tetramers" dielectric constant behavior as a function of temperature and frequency. They found that these materials exhibit a very high dielectric constant as the temperature increases, reaching ~ $>10^5$ at 1 KHz (for CuPc "tetramer"), then it drops suddenly at a certain temperature. Dielectric constant behavior was attributed to a hyperelectronic nomadic polarization. A similar explanation was introduced by Pohl and Hartman *et al*. [66] for polyacene quinone radical polymer based on pheothiaxine and metallic tri-anhydride (a semiconductor polymer), the dielectric constant could reach ~1800 at 1 KHz.

Electrical properties of these MePc "tetramer" compounds which exhibiting a high dielectric constant ($\varepsilon > 10^3$), have been studied extensively. Zhang *et al*. [67] and others[68] published a dozen of publications[31] based on CuPc "oligimers" which are used as filler in a polymer matrix for an all-organic composite actuator material.

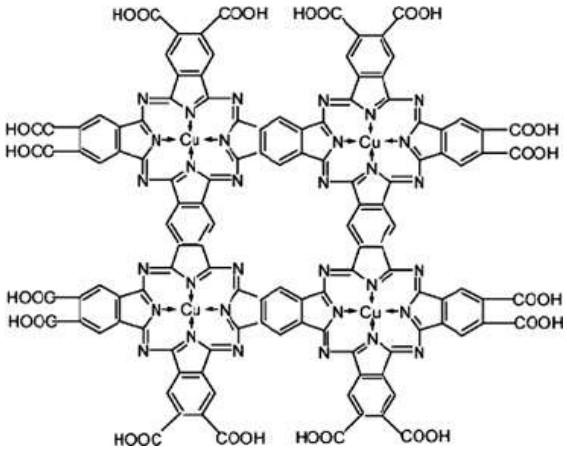

Figure 3.2 The CuPc "tetramer".

In 2008, Opris *et al*. [69] reported that the high dielectric constant could be associated with a monomeric octacarboxylic CuPc, which forms from dipentyl-4, 5-dicyanophthalate without any formation of tetramer CuPc. Recently, Mezei *et al.* [70] using a mass spectroscopic analysis confirmed that what has been proposed to be as a "tetramer" or "oligmer" is actually a monomer. Dr. Mezei's group called the Monomer octacarboxylic CuPc or CuPc*; we will use this abbreviation through the rest of the work.

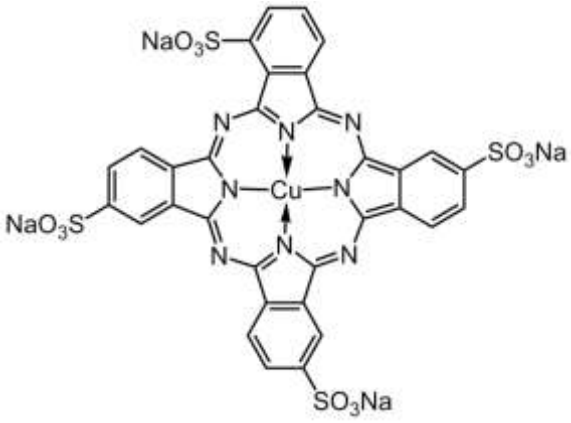

Figure 3.3 Copper phthalocyanine 3, 4', 4", 4"'-tetrasulfonic acid tetra sodium salt (CuPc_TS) structure.

Copper phthalocyanine-3, 4′, 4″, 4‴-tetrasulfonic acid tetrasodium salt (85%) (CuPc_TS) was purchased from Sigma-Aldrich (Fig. 3.3). CuPc_TS is water soluble due to the sulphonic acid group on its periphery, making it interesting for electronic applications which require solution

processing instead of regular physical vapor deposition "PVD" systems. CuPc_TS has been used in organic photovoltaic devices, [71, 72, 73] as a dye, [74, 75] and it has been used as an antiviral drug (against HIV). [76]

Materials synthesized by Gellert Mezei group were:

i) CuPc* is shown in fig. 3.4, it was synthesized following the method described by Poole and Owens *et al*. [77] with a modifications of the copper source, that is, using $CuSO_4 \cdot 5H_2O$ instead of $CuCl_2$. [70, 78] Other MePc's were synthesized such as $(ZnPc)_4$.

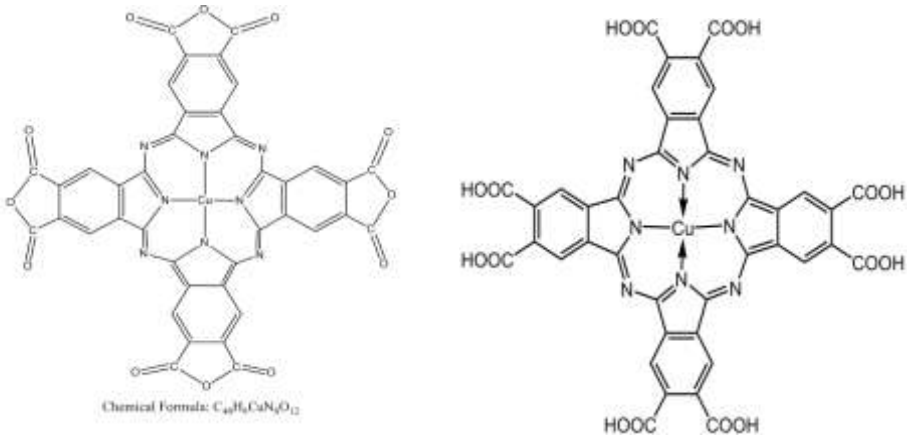

a) b)

Figure 3.4 Copper phthalocyanine monomer a) Anhydride monomer CuPc. b) CuPc*.

ii) Hyper branched dendrimer CuPc

The dendrimic copper phthalocyanine structure is shown in fig. 3.5, the dendrimer CuPc was one of the possible choices for our proposed efficient organic solar cell. It exhibits a high dielectric constant of ~46 for pellets and 15 for thin films as published by Guo *et al*., [79] at frequencies up to 1 MHz. The dielectric loss is very remarkable, about ~ 0.01 and .001 at 1 MHz for pellets and thin film, respectively. Material was synthesized using procedure described by ref. [79]

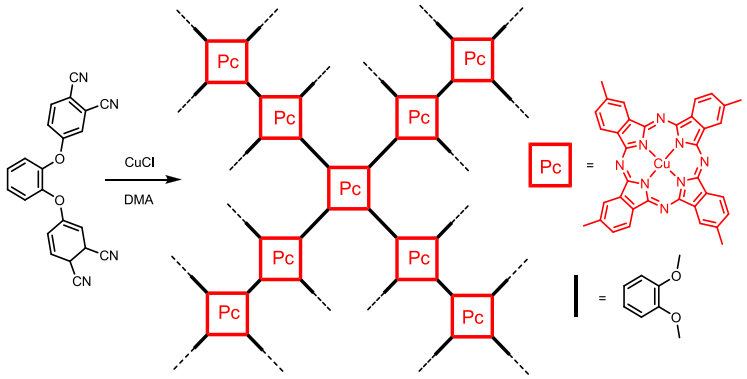

Figure 3.5 Dendrimer CuPc structure.

3.2 Polyaniline [80]

The most interesting conducting polymer is polyaniline (PANI). The PANI structure is shown in fig. 3.7; where n represents the amine group and m represents the imine group (m+n=1). It is probably one of the most intensively investigated polymers throughout the last twenty years, due to its interesting electrochemical, electrical and optical properties, in addition to its stability. [81, 82, 83] Polyaniline can be found in three oxidation states: leucoemeraldine, emeraldine, and pernigraniline. Leucoemeraldine, pernigraniline and emeraldine base show insulating properties, but the emeraldine salt shows conducting properties. As shown in fig. 3.7, when n=1, and m=0 a full reduction state is produced where amine groups link together, which is known as Leucoemeraldine (it has a brown color). When n=0, and m=1, the imine group links together, a full oxidation state shows up through the pernigraniline (black color). But when n and m are equal to 0.5, then the emeraldine is produced in a half oxidation state, and this form of polyaniline is referred to as emeraldine base (blue color). The emeraldine base is regarded as the most useful form of polyaniline due to its high conductivity and stability at room temperature.[84] The basic site (imine and amine group) in the polymer backbone of the emeraldine base can be protonated with strong acid to produce emeraldine salt leading to an increase in conductivity due to the effect of charge transfer in the polymer backbone. So in terms of conductivity, emeraldine salt is the most conductive polymer. Leucoemeraldine is easily degraded due to easily oxidization so it is not stable compared to the pernigraniline. The polaron and bi-polaron movement of charge carriers in

emeraldine salt along the polymer chain upon applying an electric field are responsible for electrical conductivity. The concentration and mobility of this charge carrier determine the electrical conductivity. In general polyaniline is insoluble in water; polyaniline salt is soluble in strong acids like sulphonic acid and hydrochloric acid. Polyaniline salt and base were purchased from Alfa Aesar.

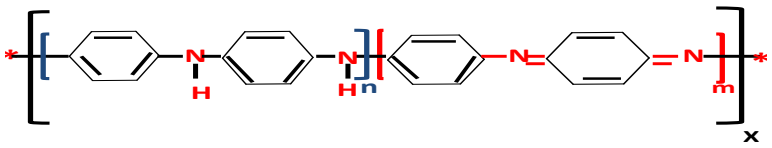

Figure 3.7 Polyaniline structure.

CHAPTER IV

EXPERIMENTAL

4.1 Dielectric constant measurements

The complex linear dielectric constant is given by $\varepsilon^*(\omega) = \varepsilon' - i\varepsilon''$ where ε' and ε'' are the dielectric constant and the dielectric loss respectively. Different techniques can be used to measure the dielectric constant of materials. One of them is the cavity perturbation technique, where electromagnetic waves frequencies (microwaves) were used, [85, 86] another technique is ellipsometery, which depends on Maxwell's equations. One of the most convenient methods is the parallel plate capacitor

$$\varepsilon' = \frac{C\,d}{\varepsilon_o A} \tag{4.1}$$

where C is the capacitance of the sample, and A is the surface area of the electrode. No corrections were made for fringing fields along the edges.

All materials were ground and pressed into 12 mm diameter pellets with a disk shape, under a pressure of ~40-55 MPa using a hydraulic press at room temperature. We also made measurements on thin films for CuPc_TS, CuPc*, and dendrimer CuPc. Solutions were made with concentration of 0.2 M for CuPc_TS. CuPc* was prepared by mixing 100 mg of CuPc* and 0.04g of NaOH into 10 ml distilled water. Dendrimer CuPc solution was prepared by mixing 100mg with 20ml N, N-dimethylacetymide (DAMC). All solutions were stirred for a week at least before using them. Indium-tin oxide (ITO) coated glass slide was used as the lower contact. Slides were cleaned before using them by acetone, iso-propanol, and distilled water in subsequent rinses for 15 minutes each. Finally, the UV-Ozone cleaner from Bioforce-nanosciences was used for 30 minutes to clean the ITO surface and achieve a good wetting (coating). Solutions were spin-coated on the ITO at 300 rpm for 20sec then 1000 rpm for 60 sec for CuPc_Ts, 500 rpm for 20 sec and 2500 rpm for 40 sec for CuPc*, while the dendrimer CucPc solution was drop cast. Thickness was determined using

an Atomic Force Microscope (AFM) from ThermoMicroscopes Auto Probes, except the dendrimer CuPc thin film was determined by WYKO-RST. Finally, 100 nm of silver electrode was thermally evaporated on the top of the thin film to provide the upper contact. We measured the capacitance of our sandwiched samples between two parallel copper electrodes using a Quadtech 1920 meter as a function of frequency from 20 Hz to 1 MHz. The pellet had the same diameter as the electrodes. The amplitude of the applied ac signal to the sample was 1V. A Gartner ellipsometer L126B was refurbished and used to find out the dielectric constant at optical frequencies for CuPc thin films.

4.1.1 Temperature dependence

Temperature measurements for the pellets electrode system were taken inside an isolated box using thick walls of Teflon material, heating was controlled by a Lakeshore 340 temperature controller. A cartridge (200 watt, 30V) was used as a heater, and resistance temperature detector (RTD-Pt100) as a thermometer. The temperature range was 20-200 C°.

4.1.2 Relative humidity dependence

Through the temperature dependence measurements, we noticed a water content effect on the dielectric constant values while in ambient atmosphere. The influence of water content on the dielectric constant values was studied for all samples, CuPc_TS, CuPc* and dendrimer CuPc Pellets were dried by being placed in a closed environmental chamber with Drieritea (calcium sulfate), which is 0% relative humidity (RH). Humidity and temperature were monitored in situ using a wireless sensor (OM-62 from Omega Corporation with error ±2% RH). RH was increased from 0% to 75% RH using partial water pressure over various saturated aqueous salt solutions in a closed environment (dessicator jar) as shown in fig. 4.1. We achieved 11% RH using lithium chloride,

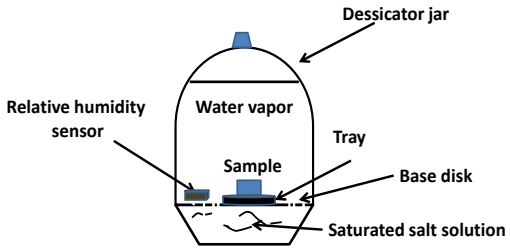

Figure 4.1 Dessicator jar used to control sample's moisture content.

43% RH using potassium carbonate and 75% RH using sodium chloride. [87] A similar procedure was used in Ref. 69.

Samples were kept under these conditions until equilibrium was reached by monitoring the reading steadiness of the relative humidity sensor. It took two days to equilibrate at 0% RH, five days to reach 11% RH, two further days to reach 43% RH, and a week to reach 75% RH. Pellets were measured at room temperature and humidity immediately upon removal from the environmental chamber to minimize changes in the water concentration in the sample. A typical measurement took about 5 minutes to carry out.

4.2 Optical Absorption

The most broadly used technique to find the absorption in materials is UV-VIS (ultraviolet-visible) absorption spectroscopy. The UV-VIS for different materials depends on their molecular structure and solvents. The relationship between the incident intensity I_o and transmitted intensity I is given by Beer-Lambert law [88]

$$I = I_o e^{-\alpha t} \tag{4.2}$$

$$A = ln\frac{I_o}{I} = \alpha t = \varepsilon\, c\, t \tag{4.3}$$

Where (A) is the absorption of the material, (C) is the concentration in molarity unit (M), ε is the molar extinction coefficient at wavelength λ with units M^{-1} cm^{-1}, and t is the distance in cm that light passes through the material. The PerkinElmer Lambda 35 was used as a UV-VIS machine.

4.3 Time-resolved photoluminescence (TR-PL) measurements

TR-PL is a non contact method to monitor the recombination and transport of excitons in materials. It is measured by exciting the material with a pulsed light source, and monitoring the photoluminescence (PL) as a function of time. The detectors that can be used for TR-PL are photomultiplier tube (PMT) in the case of single-photon counting which can provide a time resolution of 1 nanosecond. [89]

For the case of better time resolution, a streak camera can be used that can provide picoseconds time resolution. For femtosecond time resolution, electronics are not sufficient. So, optical delay between a gate pulse and luminescence from sample are used to achieve femtosecond time resolution by a technique of fluorescence upconversion.

The exiton lifetime measurements give an idea about the exciton type (weakly or strongly bound excitons) produced in the material after photo-excitation. Lifetime measurements give an idea about the critical diffusion length needed for organic materials involved in OPV cells to better harvest excitons before decaying (recombination). [90] Time-resolved luminescence anisotropy is one other important parameter that can provide interesting information about the exciton localization/delocalization in the materials. This can be determined by placing polarizers in the excitation and emission channels, and measuring the luminescence decay of the parallel and perpendicular components. The preferred excitation for molecule is the one whose transition dipole moments are oriented parallel to the light's electric field vector E. With polarized excitation, the materials whose dipole is parallel or in the cone of photoselection will be excited. Most of the time, the luminescence will come in the parallel channel and as time progresses, the

dipolar orientation will be lost due to rotational relaxation. By monitoring the luminescence in parallel and perpendicular polarizations, one can determine the fluorescence anisotropy. [88, 91]

For excitation with linearly polarized light the fluorescence anisotropy r, and polarization P, are defined by [91, 88]

$$r = \frac{I_{par} - I_{per}}{I_{par} + 2I_{per}} \quad (4.4)$$

$$P = \frac{I_{par} - I_{per}}{I_{par} + I_{per}} \quad (4.5)$$

where, I_{par} is the fluorescence intensity measured parallel to the excitation light, and I_{per} is the measured emission perpendicular to the excitation. The anisotropy and intrinsic polarization depend on the angle θ between the excitation and the emission transition moment given by [91, 88]

$$r_o = \frac{3\cos^2\theta - 1}{5} \quad (4.6)$$

$$p_o = \frac{3\cos^2\theta - 1}{\cos^2\theta + 3} \quad (4.7)$$

The anisotropy r_o values give an idea about the nature of localization on the same molecule or delocalization of the excitation. If the anisotropy reading is 0.4, it means a localized excitation. As values getting closer to 0, the delocalized excitation exists. [92, 90] Ultrafast optical physics were studied using the Tsunami Ti: Sapphire, femtosecond laser from Spectra Physics. For steady-state measurements, Edinburgh fluorescence spectrometer (FLS900) was used. Steady state measurements and upconversion measurements were measured under the supervision of Dr. Guda Ramakrishna (Chemistry Department).

4.4 Thermogravimetric analysis (TGA)

TGA investigations where done for CuPc_TS using a Q-500 machine from TA Instruments to study water content inside the material and the thermal stability of the CuPc_TS. The samples were heated from 15 to 600 °C in a nitrogen atmosphere with a flow rate of 40 ml/minute with a heating rate of 10 °C min^{-1}.

4.5 Organic PV cells preparation and measurements

4.5.1 Transparent conductive oxide (TCO) substrates

The substrate of organic solar cells is glass coated with ITO, the most used transparent conducting oxide (TCO) in the photovoltaic industry. It was purchased from Sigma-Aldrich, and was used as the anode for our PV cells. ITO substrate slide dimensions were 25 mm × 25 mm × 1.1 mm, 1,200-1,600 Å thicknesses, with 8-12 Ω/sq surface resistivity, and 84% optical transmittance. At the earlier stages of our research we used the ITO as received but we found that there were electrical shorts in our devices due to the high ITO surface roughness; the very thin layers that we used were not able to cover and smooth the roughness of the surface. Another issue is the heat of the evaporated top (cathode) electrode makes it easy to destroy the upper part of active material and then make a short. Another problem was our hand pressure through pushing the copper wires to be adhesive with silver paste. Itching the ITO surface chemically by diluted HCl (20%) for short period of time (10 minutes) was one of the ways to prevent shortage in our devices, due to time consumption and improvement in performance of our cells; we started seeking other ways to prevent shorts. We found that ITO surface has to be cleaned using three different organic solvents in a bath-sonicator starting with acetone, then iso-propanol, and finally with distilled water of 15 minutes each respectively. That helps to get the ITO surface cleaner and makes it smoother. Later on, we found that some of the ITO surface should be removed totally at the region where the electric contact had to be placed to avoid shortage and active area destruction. The area of ITO needed to be used, was covered by an anti-acid tape, making sure that there is no air bubbles or pin holes on the tape surface, to prevent HCl from diffusing through them into the ITO surface. We used different methods like concentrated HCl for 30 minutes, but later we used 20% HCl heated for 15min at 50°C to obtain the desired pattern for device fabrication as shown in fig. 4.2.

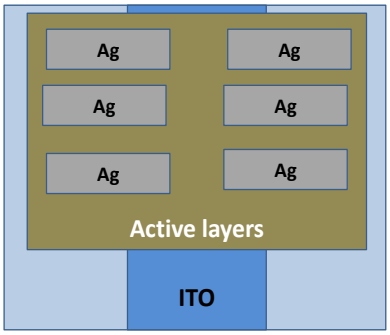

Figure 4.2 Final pattern of the ITO substrate.

The final cleaning step was the ultra violet ozone cleaning (UV-Ozone) using machine from Bioforce-nanosciences. UV-ozone was used for 30 min to clean the ITO surface from organic residuals and to achieve good wetting between the ITO surface and solutions.

One of the efficient materials that we used to improve PV performance was poly (3, 4-ethylenedioxythiophene)-poly (styrenesulfonate), known as PEDOT:PSS. It was purchased from Sigma-Aldrich with 1.3 wt % dispersed in water. It works as (i) a short preventer by reducing ITO surface roughness (smoothing ITO surface), (ii) an electron blocking layer (EBL), to stop electrons leakage through the ITO. The work function of PEDOT:PSS film is 0.2 to 0.3V higher than the ITO, which helps to give ohmic contact between ITO and photoactive material (donor), and gain extra open-circuit voltage. PEDOT:PSS is also known to help adhesion of photoactive film to ITO, thus decreasing the series resistance of the device.[93,94] To conduct current we used copper foil strips, two different types of silver epoxy were used. The first one was purchased from Lakeshore which needs annealing at 120°C for 15 min to dry. So we decided to switch to another silver epoxy, Dotite silver paint D-550 purchased from SPI supplies, due to its ability to be cured at room temperature without affecting our materials by annealing.

4.5.2 Thermal physical vapor deposition (PVD)

We rebuilt a Denton DV-502 thermal evaporator system donated from Pfizer company, as shown in fig. 4.3, to fit our needs. We built an aluminum base below the evaporator bell jar with four inlets to allow us to insert any probe or tool in the future, one inlet was used to install a Q-pod quartz crystal monitor (QCM) from Inficon for monitoring thin film thickness which is an

extremely useful tool for not only measuring the amount of material that has been deposited at any point in time on a substrate but also the rate at which that deposition is taking place. The principle behind this technique is measuring the amount of material deposited on a piezo crystal sensor mounted in a holder during the deposition cycle. This technique is based on the assumption that a similar quantity of the material being deposited on the substrate will also be deposited on the crystal sensor head, which is mounted in position near the substrate and in the same orientation towards the deposition source. The measurement technique uses the changes in the resonant frequency of the quartz crystal as more material is deposited on it. The frequency change is proportional to the amount of evaporated material deposited on the crystal; the more film deposited, the lower the resonant frequency becomes. Our sensor crystals have a resonant frequency of 6 MHz. Due to their sensitivity to any contamination, it is important to handle quartz crystals carefully since small amount of material deposited on them can make them unusable. It is necessary to use laboratory gloves and plastic tweezers during handling and set up. The opposite inlet was used to install a shutter to control the evaporation process, and prevent any impurities imbedded in the material which have sublimation temperature less than the desired material from being deposited on the substrate. Masks were made for both sample fabrication as sample holders and for metal electrode evaporation. The deposition system (Fig. 4.3a and fig. 4.3b) includes two resistive heating evaporation sources (Alumina coated boats) located at the bottom of the evaporating chamber which came from R.D. Mathis. The devices top electrode was deposited thermally through a shadow mask, all evaporation was done at a base pressure of 10^{-8} torr. This vacuum pressure value can only be maintained by changing the diffusion pump oil every 12 months. The top electrode material used in this thesis is silver (Ag) 99.99%, which was obtained from Sigma Aldrich. Our machine has two different voltage power supply sources to enable us to do co-evaporation; the evaporation rate can be controlled by the applied electrical power.

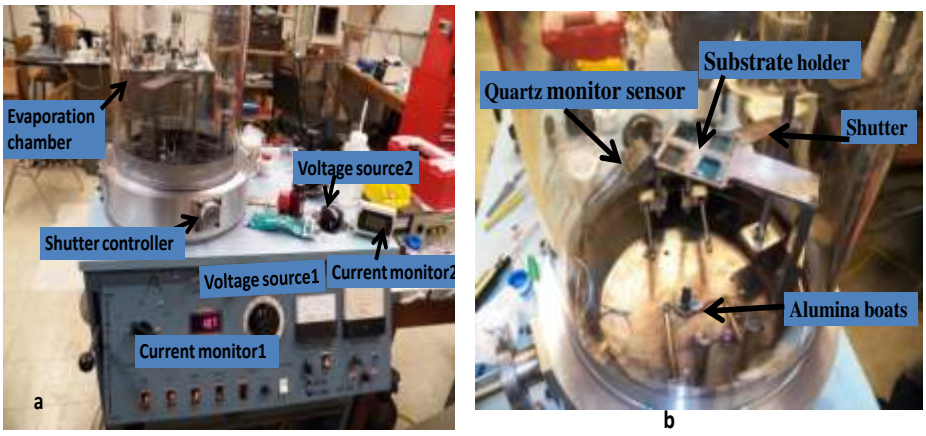

Figure 4.3 a) Denton DV-502 thermal evaporator. b) Deposition chamber.

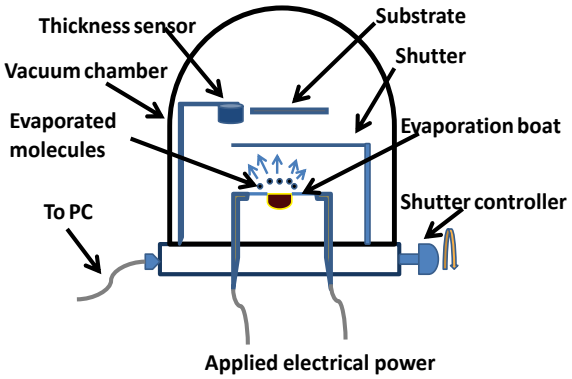

Figure 4.4 Cross sectional view for the deposition chamber.

We started by reproducing the basic devices like the original C.W. Tang bilayer heterojunction published in 1986. [10] Tang used copper phthalocyanine (CuPc) as p-type and perylene derivatives 3,4,9,10-perylene tetracarboxylic-bisbenzimidazole (PTCBI) as n-type, and he got power conversion efficiency ~1% . In our case we used CuPc 95% and another type of perlene derivative which was 3, 4, 9, 10-Perylenetetracarboxylic dianhydride (PTCDI 98%), and 4, 9, 10-perylenetetracarboxylic diimide (PTCDA 98%); all above materials were purchased from Alfa Aesar. We picked those materials because of their closest structure to PTCBI. Our cells were not efficient as Tang's cells, but the work gave us an opportunity to understand the device fabrication procedure and gave us training how to improve devices performances. Table 4.1 shows the main

materials we used and data useful for thermal evaporation, the minimum rate of evaporation associated with these data were 0.45A/s, except for silver where it was 1.3A/s. Over time we involved other materials to improve cells efficiency such as PEDOT:PSS as a hole transport layer (HTL) or electron blocking layer (EBL) and electron transport layer (ETL) like Bathocuproine (BCP).

The z-factor is used to match the acoustic impedance of the deposited material to the sensor crystal, it corrects the stresses as the crystal is coated. It is recommended by the manufacture to change the crystal if crystal life is reduced by 10%. If you do not know the exact z-factor you can use 1 as can be seen from table 4.1 for organic materials. [95]

Some materials had impurities through the production process, so to achieve higher levels of purity, we used the thermal purification (to sublime impurities) at temperatures lower than sublimation points of the evaporated materials fig. 4.5, purification was done in Lindberg Blue-M model 55035 furnace, the oven has been programmed as shown in the table for CuPc as an example.

Material	Density (g/cm^3)	z-factor	Melting point (M.P) C°	I (A)	V (V)
CuPc (cupper phthalocyanine)	1.65	1	600	15.8	36
PTCDI (3,4,9,10-Perylenetetracarboxylic diimide)	1.68	1	350	15	32
PTCDA (Perylenetetracarboxylic dianhydride)	1.764	1	350	15	34
C_{60} (fullerene)	1.65	1	527	16	36
BCP (bathocurpine)	1.173	1	270	6	14
Ag (Silver)	10.5	0.529	981	23	60

Table 4.1 Materials physical properties and electrical conditions associated with evaporation.

SP	Tune	LC	R1	L1	D1	R2	L2	D2	HB
20	Off	1	10	200 C°	120 min	9.00	560 C°	180 min	20

Table 4.2 Lindberg Blue-M heating program.

SP is the set point, LC is the number of cycles, R1is the temperature increment, L1and L2 are the desired temperature for each period, D1, D2 are operation time for first and second cycles respectively.

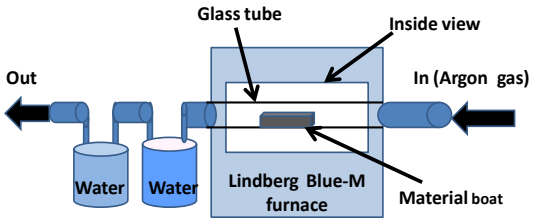

Figure 4.5 Purification process for our materials.

Solutions were prepared in our laboratory using a digital balance, bath-sonicator and magnetic plate stirrer; solutions were spin coated using a Chemat KW-4A spin coater and the devices are fabricated under ambient environment. At the end of solar cell fabrication, the substrate was glued on a microscope slide, to reduce any tension between the copper connectors and the cell surface when measuring probes (Alligators clips) were used which may pull out the electrode connections, flat copper foils were used instead of wires due to easy handling and less inertia when glued with silver epoxy.

4.5.3 Surface morphology and thickness measurements

ThermoMicroscopes Auto Probes AFM was used for surface morphology and thickness measurements for thin films. Dielectric constant at optical frequencies was measured using Gartner ellipsometry L126B which was refurbished by us. Our machine used a photometric ellipsomtery

with a rotating analyzer ellipsometer (RAE) where the intensity is measured at the detector at different analyzer angles. A HeNe Laser beam was used by the machine; for more details about calculation and working principle see appendix II.

WYKO-RST (rough surface tester) is a non-contact optical instrument, surface profilometry, and surface roughness characterization, the VSI (vertical-scanning interferometry) mode was used. The instrument produces interference fringes, when the light is reflected from the sample surface and a reference mirror. It had been used to determine samples thicknesses when the AFM was down.

4.5.4 Current–voltage (J-V curve) characteristic

At the beginning the simple circuit setup we used included a resistor box and two 34401A meters to measure voltage and current. Values of current and voltage was recorded using a LabView program at different resistances. A voltage sweep using Keithly 2400 source–meter instead of the previous setup was used later to achieve more accurate JV characteristics measurements. GreenMountain software was used to get all JV characterization parameters including V_{oc}, J_{sc}, R_{sh}, R_s, FF and η. A solar light simulator was used for all devices providing 1 sun (100mw/cm^2) at a distance of 53 cm from the light source (calibrated by the manufacturer). JV characteristic set up is shown in fig. 4.6.

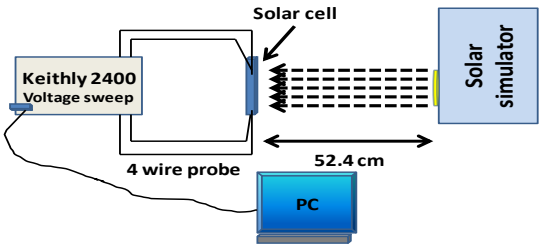

Figure 4.6 J-V characterization set up, a voltage seep is applied by Keithly 2400, the V_{oc}, J_{sc}, FF and η are extracted by the PC software.

CHAPTER V

DIELECTRIC CONSTANT MEASUREMENTS AND OPTICAL PROPERTIES

In this chapter we include our research results on investigated materials. Dielectric constant values and their behavior with temperature and frequency were recorded. We studied standard CuPc to understand the dielectric constant without any additional groups (modification), then we studied CuPc modified by carboxylated group (CuPc*), sulphonated CuPc (CuPc_TS) and anhydrate monomer CuPc as well. Dendrimer CuPc was produced due to its interesting dielectric constant value and behavior. Optical absorption was recorded for each one, life time measurements for CuPc*, and dendrimer CuPc. Finally, polyaniline (PANI) materials dielectric behavior was studied as well.

5.1 Standard CuPc

The dielectric constant and dielectric loss tangent behavior at different frequencies for standard CuPc is shown in fig. 5.1a the dielectric constant values for standard CuPc at low frequencies up to 10^3 Hz was about 7. As the frequencies increase the dielectric values decrease, then it become flat (constant) at higher frequencies reaching ~3.5 which is the intrinsic dielectric constant of CuPc. Quantitatively similar values have been found for dielectric constant of CuPc thin film by Gould,[96] and Saleh,[97] this value was confirmed by ellipsometery measurements at optical frequencies (10^{15}Hz) to be 3.5±0.75. The dielectric loss tangent for CuPc was small in average recording ~.001 at 1MHz. CuPc shows a strong frequency dependence at low frequencies up to 10^4 Hz which can be attributed by the interfacial polarization mechanism.[15, 16]

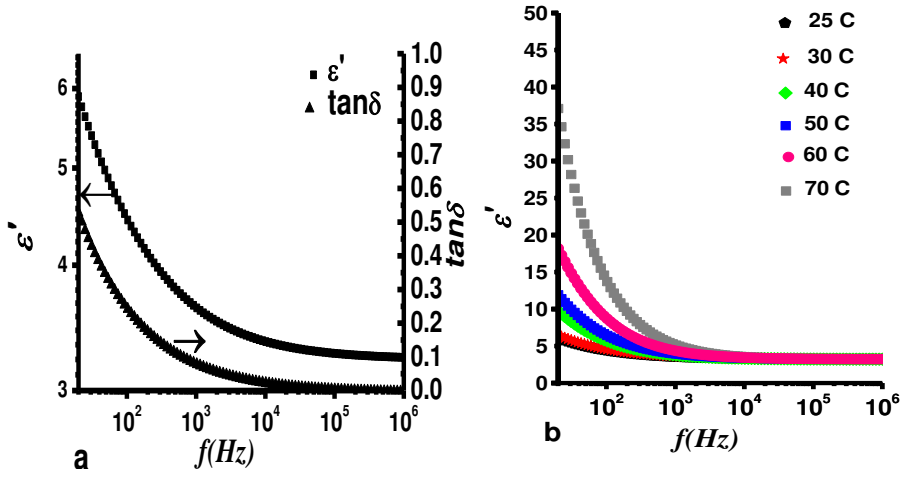

Figure 5.1 a) Dielectric constant and dielectric loss tangent at room temperature. b) Dielectric constant behavior as a function of temperature.

Optical absorption spectra of 500nm thickness CuPc is shown in fig. 5.2, and we see the two intense characteristic bands: Q band (π-π* transition) in the visible region and B-band (π-π* transition) in the ultraviolet region. The Q band shows two peaks located at the wavelength of 617 nm and 693 nm, which is almost similar to the absorption spectra for α-CuPc films.[98] The B-band (Soret band) is at 333 nm.

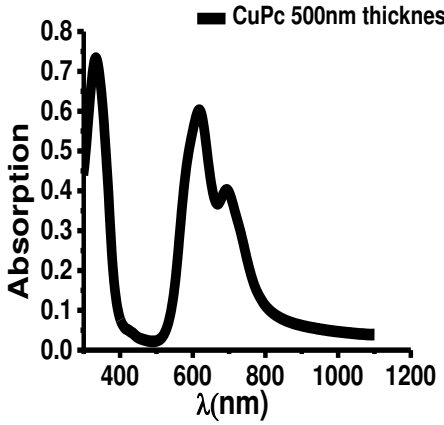

Figure 5.2 Absolute absorption spectrum for CuPc.

5.2 CuPc*, and MePc

We synthesized a modified CuPc, ZnPc and CoPc by a carboxylic group, the physical properties reported for these materials shows a high dielectric constant ranges between 30-50 for CoPc and ZnPc up to ~10^5 for CuPc tetramers. Nalwa *et al.* [65] reported the existence of the "tetramer" formed as a carboxylic copper phthalocyanine. Our results for tetramer zinc phthalocyanine dielectric constant as pellets was studied as function of temperate as shown in fig. 5.3 and we get very close values of the dielectric constant and same behavior the literature reports.

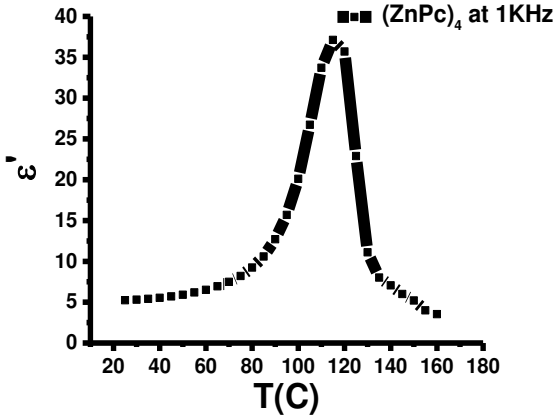

Figure 5.3 The temperature dependence for $(ZnPc)_4$.

The polarizability increases as the temperature increases, but the dielectric constant values were smaller compared to CuPc* (fig. 5.4),

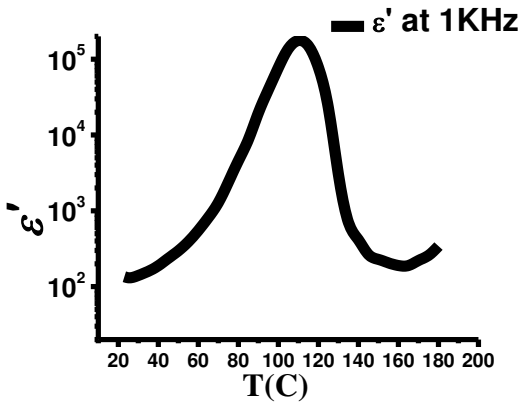

Figure 5.4 The temperature dependence of the dielectric constant for CuPc*.

For both zinc phthalocyanine and copper phthalocyanine tetramers, the dielectric constant increases as the temperature increase then an abrupt decrease occurs at 110 C°. This transition behavior was explained by Pohl [66] and Nalwa [65] by nomadic polarization, where the increase in temperature leads to an increase of the number of free carriers. The same behavior was observed for other materials; this phenomenon is common in dipolar materials like water molecules where orientational polarization mechanisms are prevailing. On the other hand, the increase of dielectric constant with temperature can be attributed to the fact that the orientional polarization is sensitive to the thermal motion of molecules, so dipoles cannot orient themselves at low temperatures. When the temperature is increased, the orientation of dipole is facilitated and this increases the value of orientational polarization, which leads to the increase of the polarizability and therefore the dielectric constant.

The temperature dependence of the dielectric constant can be represented by Arrhenius equation

$$\varepsilon(T) = \varepsilon_{\circ}\, e^{-(E/k_B T)} \qquad (5.1)$$

Where $\varepsilon_{\circ}$ is a constant which represents the pre-exponent dielectric constant (initial value), as the temperature increase the dielectric constant increases. The increase in the dielectric constant can be attributed to the increase in the molecules thermal energy as the temperature increase. It has been observed by relative humidity dependence measurements and TGA measurements that at least 8-10% of the samples weight was water, which leads to more ionization of the carboxylic and sulphonic acid groups in the material, therefore formation of hydronium ions, and the dipole nature of hydronium ions increase the orientational polarization mechanisms. The loss of water starts for the CuPc_TS and CuPc* [69] at a temperature consistent with the temperature found by the TGA measurements where the loss of polarizability (decrease in dielectric constant) occurs.

Dielectric constant behavior was investigated for different frequencies at room temperature (20° C) and average lab humidity (25 %) for CuPc* (fig. 5.5). The values at low frequencies are very high $>10^6$, decreased dramatically as the frequency increases to reach values of ~10 at 1 MHz.

Qualitatively similar behavior was observed in what other scholars thought to be oligomer carboxylic CuPc. [69]

The high dielectric constant values at low frequencies can be explained as follows: the charge carriers can hop easily from site to site with low free energy barriers in the direction of the electric field and accumulate at sites with high free energy barriers. This produces a high dielectric constant due to the net polarization, but at high frequency, the charge carriers cannot relax as fast as the field varies with time, so the charge oscillation will begin to lag behind this field, resulting in a decrease of dielectric constant. [99]

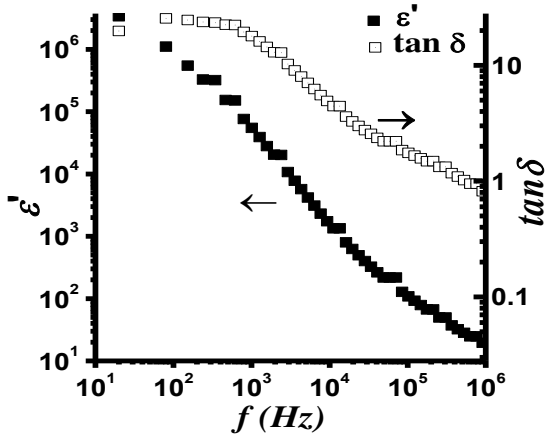

Figure 5.5 Frequency dependence of the dielectric constant, and the dielectric loss tangent for CuPc*, at room temperature and 25% RH.

Fig. 5.6 shows a comparison between two CuPc derivatives, the anhydrate monomer CuPc and the CuPc* (structure is shown in figure 3.4) where the dielectric constant values shows different values, the first one without the carboxylic group fig. 5.6a where dielectric constant values are lower than the second material fig. 5.6b. Both show high dielectric constant at low frequencies, and decreased as long as the frequency went up to 1 MHz. The first graph in fig. 5.6a has a plateau at higher frequencies starting from 10^4 Hz. If we make a comparison to the standard CuPc, we can notice the effect of the attached group on the dielectric constant values which arises from the interfacial polarization mechanism at low frequencies.

The CuPc* shows higher values up to 1 MHz without any plateau at any frequency range like the first one, the absence of the plateau may indicates more than one polarization mechanism still

contributes to the dielectric constant. We think that the orientational mechanism, due to the carboxylic group and it can ionize easily into hydronium ion when water exists. The dielectric constant values were decreasing as the frequency was increasing.

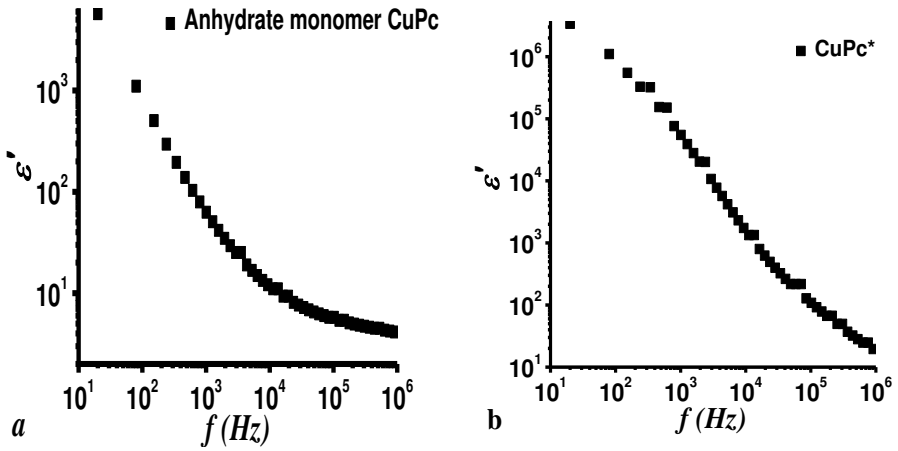

Figure 5.6 Frequency dependence of the dielectric constant; a) the anhydrate monomer CuPc and b) the CuPc*.

Opris *et al*. synthesized a monomer carboxylic CuPc, the ability to uptake moisture, which was attributed due to the ionization of the carboxylic acid. The presence of water resulted in protons being released into the material due to uptake water. [69] We synthesized the same material using different reaction and we got qualitatively the same behavior which supports the idea that water absorption by the carboxylic group is the reason behind the high dielectric constant of this material.

Fig. 5.7 shows the relative humidity dependence of dielectric constant (a), dielectric loss factor (b), and ac conductivity (c) for CuPc*. As relative humidity increases the dielectric constant increases, but in general as the frequency increases the dielectric constant and loss factor decrease. The electrical conductivity as shown in fig. 5.7c shows a plateau of dc conductivity as the relative humidity increases, the dc plateau extends over a short range of frequencies for low relative humidity.

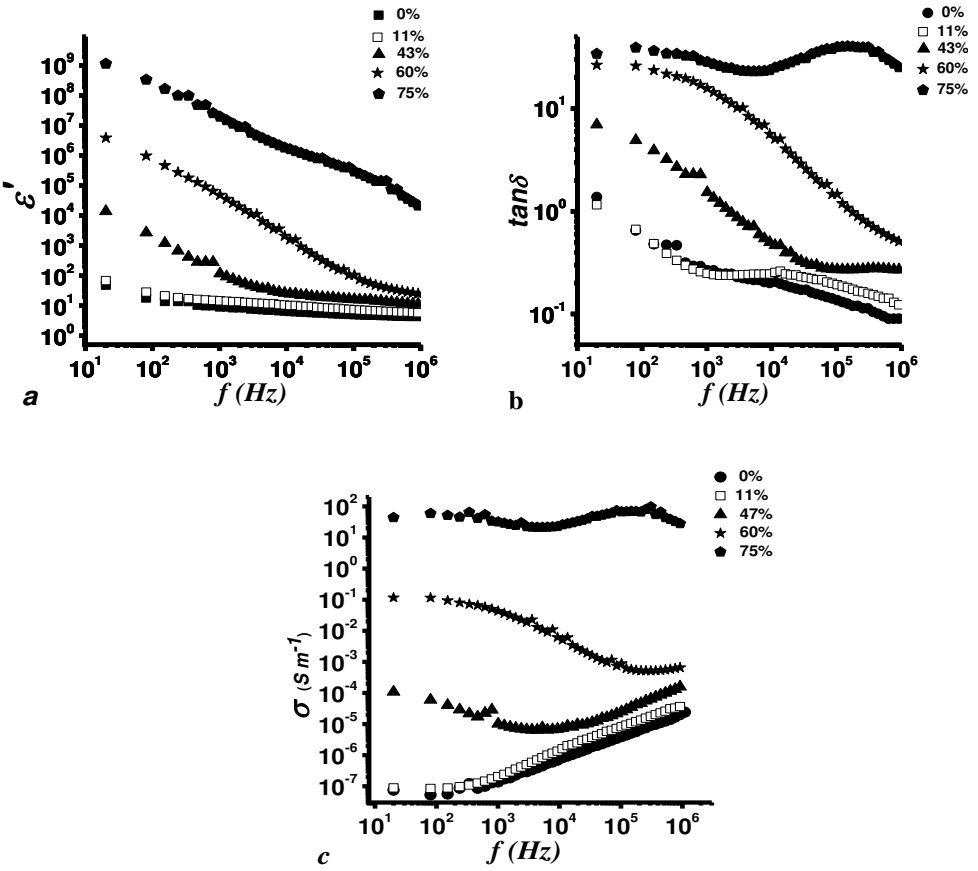

Figure 5.7 CuPc* Frequency dependence of a) dielectric constant, b) dielectric loss tangent, and c) conductivity under different relative humidity conditions.

Surface morphology atomic force microscopy (AFM) is shown in fig. 5.8. Small grains are covering the glass (substrate) surface, the white crystals are due to the existence of NaOH which was used during making the CuPc* solution as shown in fig. 5.8a where a wider area was taken. If we go down into a smaller area as in fig. 5.8c, we can notice the grainy small particles which make a lot of interfacial surfaces in a nano-size which could be the reason behind the huge interfacial polarization response in the dielectric constant.

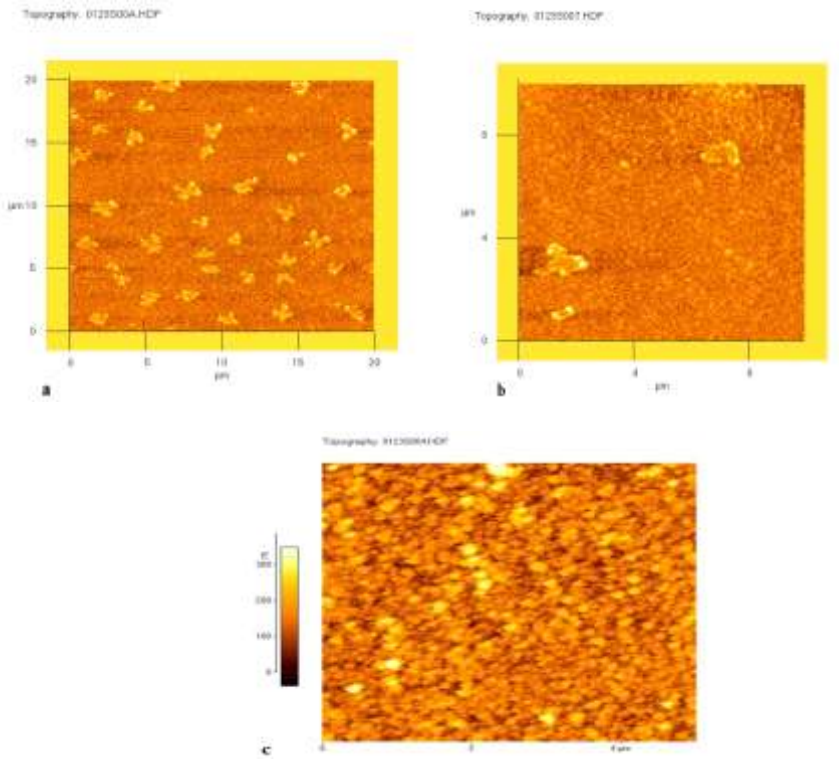

Figure 5.8 CuPc* surface morphology using atomic force microscopy (AFM), different scanned areas from the larger as in (a and b) area to smaller as in (c).

5.2.1 CuPc* time-resolved photoluminescence (TR-PL) measurements

The TR-PL decay of CuPc* solution in water is shown in fig. 5.9. We excited using a laser pulse of 400 nm and the emission was monitored at 690nm, where a weak luminescence was observed. For the steady state measurements, we excited at 390 nm and 400 nm, but no emission was observed in the visible wavelengths suggesting the absence of luminescence from higher excited states. However, after excitation at 650 nm, a weak emission peak at 700 nm was observed that is attributed to the luminescence from the singlet state of the molecule. Femtosecond luminescence decay of CuPc* was fitted with a bi-exponential function with lifetimes of 870 ± 80 fs (93.9%) and 11 ± 8ps (6.1%). Faster lifetime suggest that the singlet exciton decay faster giving rise to probably a triplet exciton because of the presence of copper atom in the middle. The spin orbit coupling is very efficient in the presence of transition metal ions with vacant d-orbitals which lead to efficient inter-system crossing. The anisotropy measurements have shown an initial value of 0.07 which is

closer to 0.1suggesting that the excitation is delocalized in a plane. [102] Faster luminescence lifetime in CuPc* indicates the presence of efficient non-radiative decay pathway that can be attributed to intersystem crossing.

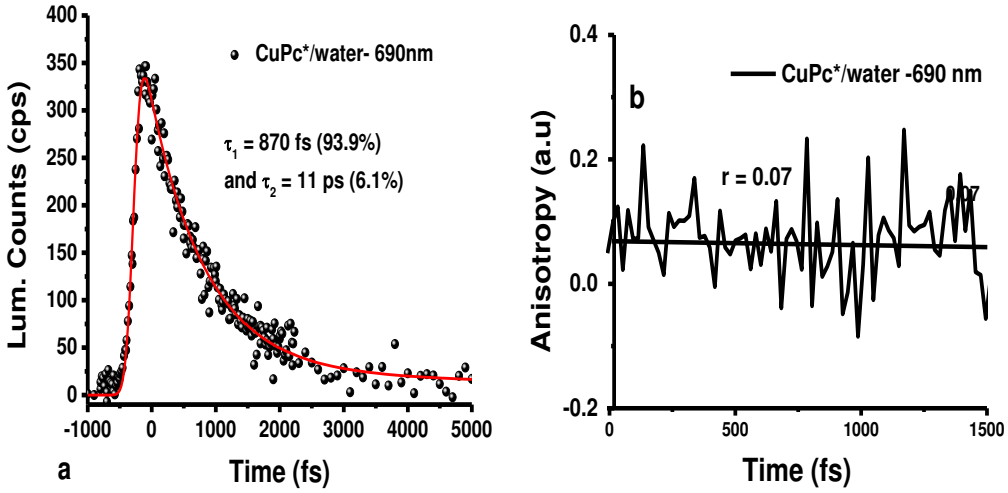

Figure 5.9 a) Photoluminescence decay of CuPc* in water at 690 nm after excitation at 400 nm. b) Anisotropy decay of CuPc* in water monitored at 690 nm.

5.3 Hyperbranched dendrimer CuPc

The most interesting material was the dendrimer CuPc, as we mentioned in chapter 3, it was one of the best available choices to achieve our proposed goal of increasing the solar cell efficiency using higher dielectric constant. However, we did not find a large dielectric constant as seen by previous researchers. The dielectric values were constant for all frequencies (frequency independent) as can be seen from fig. 5.10. We recorded a dielectric constant around 3.5 as shown in fig. 5.10. The reason for constant values of the dielectric constant, is the absence of dielectric constant dispersion, due to interfacial polarization (Maxwell-Wagner effect), which is usually results in an inhomogeneous materials (heterogeneous) as can be observed in most materials like polymeric MePc composites. [52, 53, 63] On the other hand, there is no evidence of an orientational polarization effect, like what we already found on CuPc*, or as we will see later for CuPc_TS.

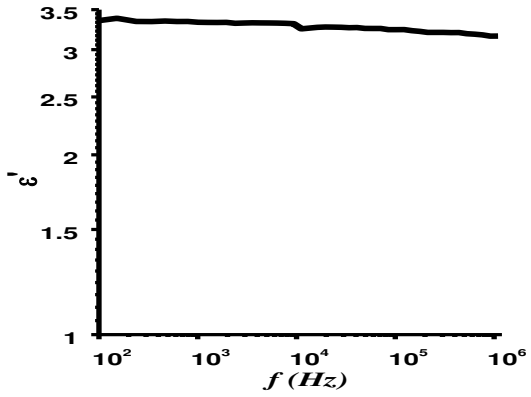

Figure 5.10 Dendrimer CuPc pellet at room temperature.

Temperature variation does not show any transition peaks (temperature independent) as shown in fig. 5.11, which give an indication of the absence of any dipoles sources or energy barriers. No orientational polarization was observed like other CuPc derivatives like CuPc* or CuPc_TS where the dielectric dispersion was high. On the other hand, the dielectric loss was small, recording 0.01 and 0.001 at 1MHz for pellet and thin film samples respectively.

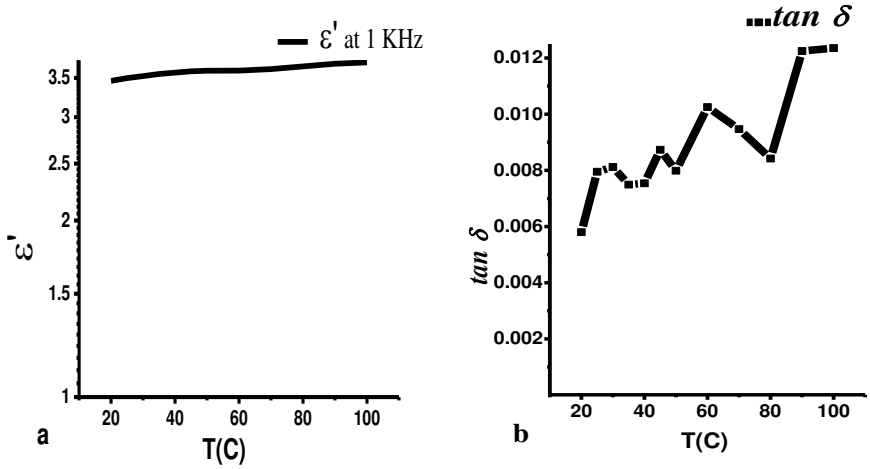

Figure 5.11 Dendrimer CuPc pellet factor as function of temperature a) dielectric constant and b) dielectric loss factor.

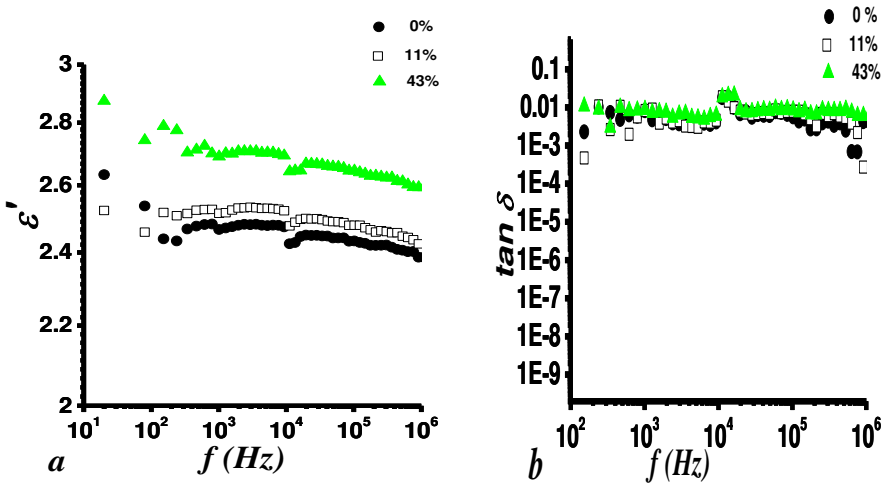

Figure 5.12 Dendrimer CuPc pellet under different relative humidity levels conditions at room temperature as a frequency dependence a) dielectric constant and b) dielectric loss factor.

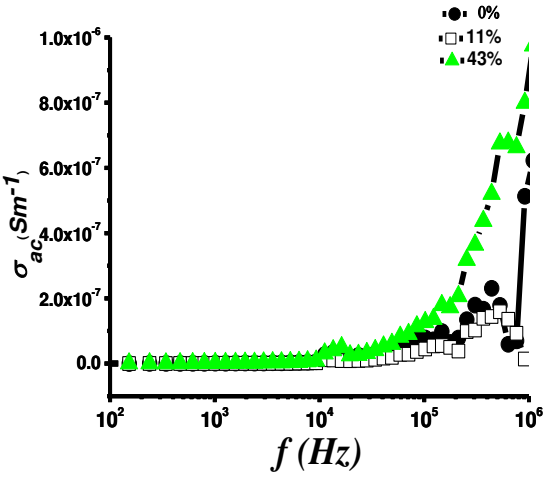

Figure 5.13 Dendrimer CuPc pellet conductivity as a function of frequency under different humidity levels.

The relative humidity effect on the dendrimer CuPc is shown in fig. 5.12. The moisture effect on the dielectric constant behavior was studied extensively by our group for sulphonated, and carboxylic CuPc derivatives. Bao *et al*. [100] and Melcher *et al.* [101] also studied polymer and glassy samples where they show how water content (moisture) effects the dielectric constant measurements, where the dielectric constant readings were shifted up as the moisture content increase.

Dendrimer thin film samples with 50 µm thickness (using WYKO-plus), were measured under ambient atmosphere, a constant values of the dielectric constant at all frequencies were recorded, and the values were higher than pellets.

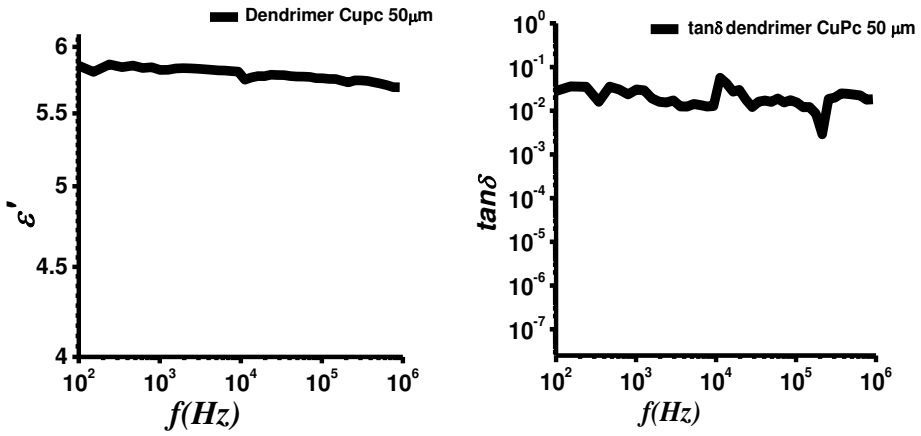

Figure 5.14 Dendrimer CuPc thin film dielectric constant frequency dependant under room temperature.

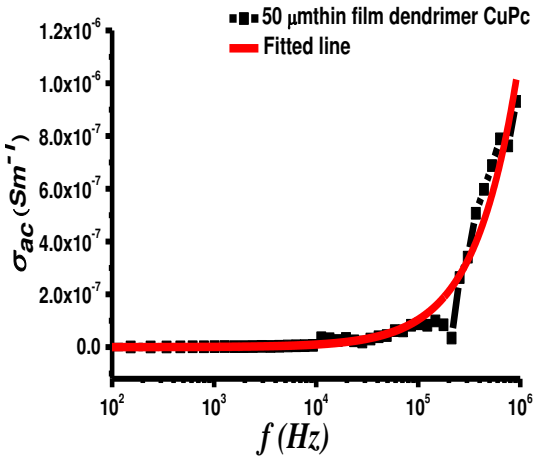

Figure 5.15 Dendrimer CuPc thin film conductivity as a function of frequency under room temperature and humidity (~20%RH).

Electrical conductivity for dendrimer CuPc thin film and pellets (fig. 5.12 and fig. 5.14 respectively) shows two distinguished regions, one is a plateau extending to 10^5 Hz which represents a frequency independent conductivity (constant with frequency), where we can call it the dc conductivity region. The other region, which has strong frequency dependence, is presented

at frequency more than 10^5 Hz. This behavior was explained by universal power law in equation 2.32. The ac conductivity can be computed using the empirical relation:

$$\sigma_{ac} = 2\pi f \varepsilon_0 \varepsilon' \tan\delta \quad (5.2)$$

Here f is the frequency and tanδ is the dielectric loss tangent. The universal dielectric response has already been observed in CuPc where the ac conductivity of the Pc samples showed a frequency dependence [16, 22, 24]. Conductivity which was fitted by universal power law $\sigma(\omega) = A\,\omega^s + \sigma(0)$, where ω is the angular frequency, s is the frequency exponent factor, A is constant represent the ac conductivity factor, and $\sigma(0)$ is the dc conductivity. Frequency exponent factor was s= 0.99 ~ 1 as it can be found from the curve in fig. 5.15.

When thin film samples were left in the vacuum chamber (10^{-8} torr) for 3 days, the readings were shifted down compared with ambient readings. That could be attributed to the loss of moisture content inside the material which is opposite behavior to the samples in fig. 5.12.

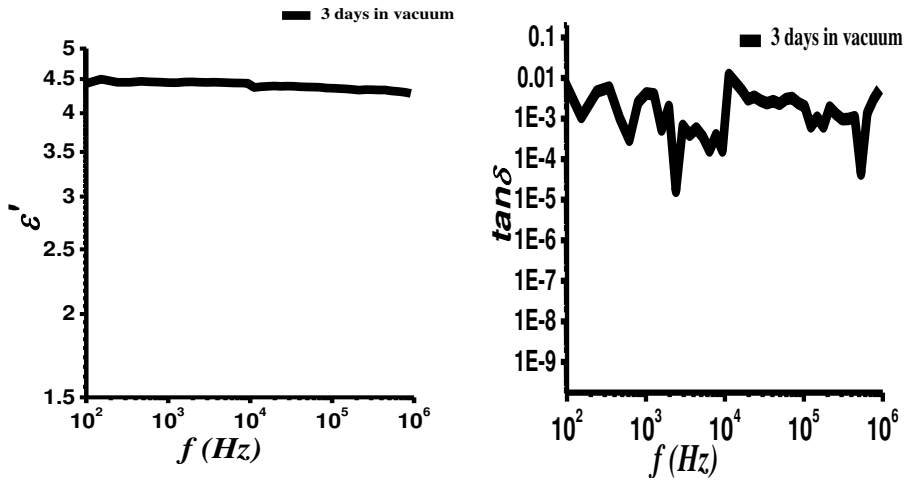

Figure 5.16 Dendrimer CuPc thin film dielectric constant at different frequencies under room temperature, after 3 days under vacuum.

5.3.1 Dedrimer CuPc optical and time-resolved photoluminescence (TR-PL) measurements

Optical absorption spectra for dendrimer CuPc shows absorption peaks at in the visible region and shows a peak at 678 nm in two different solvents N, N dimethylactymide (DCMA) and

dichloromethyl methyl ether (DMCE). The peaks are consistent with the Q-band and soret bands of copper phthalocyanines.

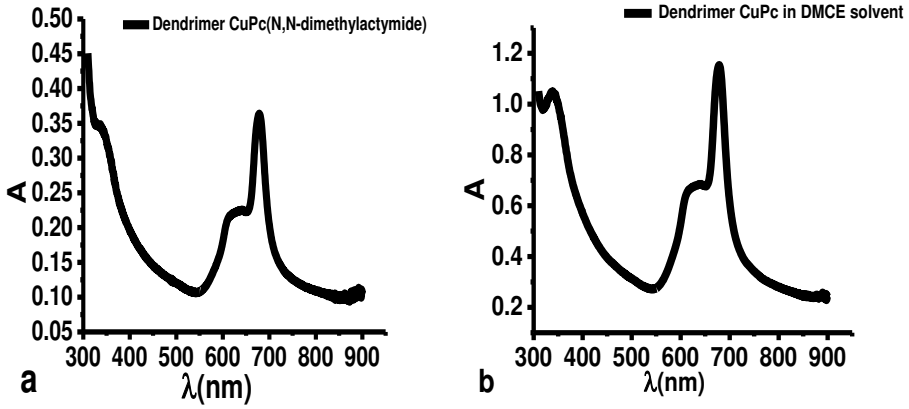

Figure 5.17 Absorption spectrum for dendrimer CuPc solution in a) N, N dimethylactymide and b) dichloromethyl methyl ether (DMCE).

The TR-PL was carried out for dendrimer CuPc solution in DMAC after excitation at 400 nm and corresponding decay at 690 nm as shown in fig. 5.18a. We have monitored emission at 690 nm and observed a weak luminescence counts. Furthermore, no emission in the higher energies was observed after excitation at 400 nm suggesting ultrafast relaxation to singlet state. The luminescence decay at 690 nm was fitted with a bi-exponential function with lifetime of 380 ± 50 fs (90.5) and 12 ± 4 ps (9.5%). It can be observed that the lifetimes of dendrimer CuPc are relatively faster than that of the CuPc* suggesting the interaction between different phthalocyanines in the dendritic unit. The anisotropy measurements (fig. 5.18b) value was estimated to be 0.04 which is closer to 0 and provides an indication of three dimensional delocalization of the excitation in the material. [102, 103] Here again, faster intersystem crossing to triplet state might be the main reason behind ultrafast singlet state decay.

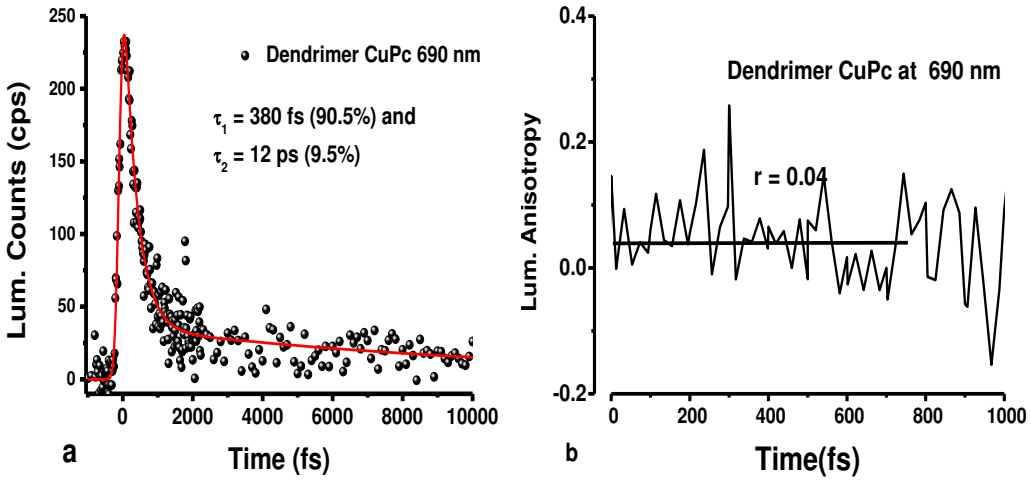

Figure 5. 18 a) Photoluminescence decay of CuPc dendrimer at 690nm in DMAC b) Anisotropy measurements of CuPc dendrimer.

5.4 Copper phthalocyanine-3, 4′, 4″, 4‴-tetrasulfonic acid tetrasodium salt (CuPc_TS)

The dielectric constant and dielectric loss tangent behavior at different frequencies for CuPc_TS are shown in Fig. 5.19 CuPc_TS has a giant dielectric constant at low frequencies recording values more than 10^6, where we can assume the influence of all kinds of polarization mechanisms takes a place here, dielectric constant values shows a continuous decrease (except for a plateau near 200 Hz) as the frequency increased until 1MHz recording a values about 200.

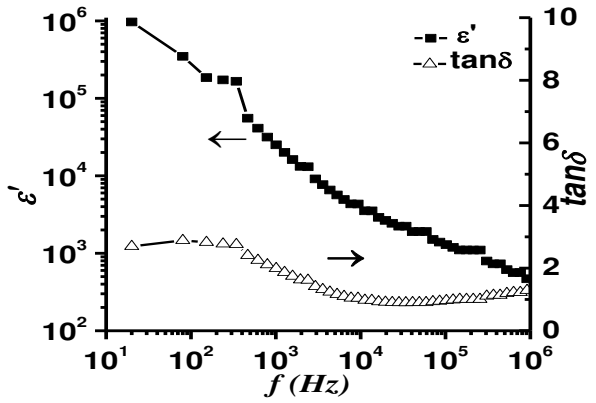

Figure 5.19 Frequency dependence of the dielectric constant, and the dielectric loss tangent for CuPc_TS, under room temperature, and 25% RH.

The temperature dependence of the CuPc_TS's dielectric constant as a function of frequency (fig. 5.20), the dielectric constant values were observed to increase as the temperature increase, a very high value $>10^6$ at 20 Hz was recorded, the reason behind the large dielectric constant value at low frequency can be attributed to the interfacial polarization, the dielectric constant values decreasing as the frequency increases up to 1 MHz, the high values at high frequency could be because of the orientational polarization contribution, this effect may indicate a disordered random orientation of molecules in the material, so when the temperature is raised, thermal energy of molecules increases which reduces the internal molecular forces (reduce bonds energy) [104] which leads to enhancement of the orientational vibration, then increases the polarization due to more alignment of dipoles with the field. Polarization peak "phase transition" for CuPc_TS was observed at 70 C°, qualitatively similar behavior has been reported for what assumed to be for CuPc* at 1 KHz. The phase transition associated with temperature dependence measurements for CuPc_TS or CuPc* is not an evidence of the spontaneous polarization [74, 71] which is a characteristic of typical ferroelectric materials.

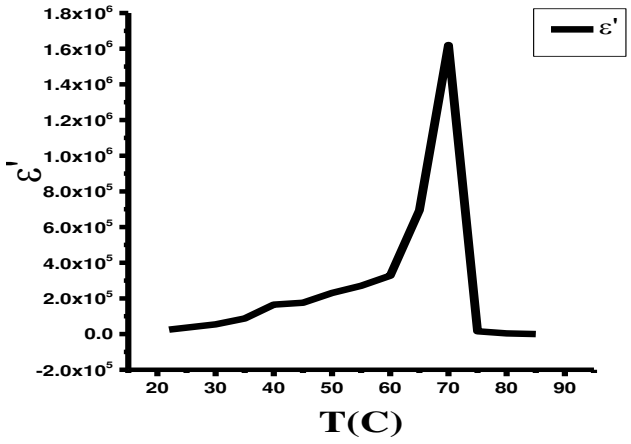

Figure 5.20 Dielectric constant of CuPc_TS as temperature dependence at 1 KHz.

Modified CuPc* was found to have the ability to absorb moisture by Opris *et al.* [69] CuPc_TS has a sulphonated functional group, which is the reason behind the water solubility of this kind of CuPc; we studied the moisture effect on the modified CuPc with sulphonated group, we observed

similar behavior of water absorption by CuPc_TS. We recorded the humidity effect on the dielectric constant, dielectric loss, and dielectric loss factor values for CuPc_TS as shown in fig. 5.21a, in fig. 5.21b, and in fig. 5.22a respectively. The recorded dielectric constant, dielectric loss, and dielectric loss factor decreased as the relative humidity decreased.

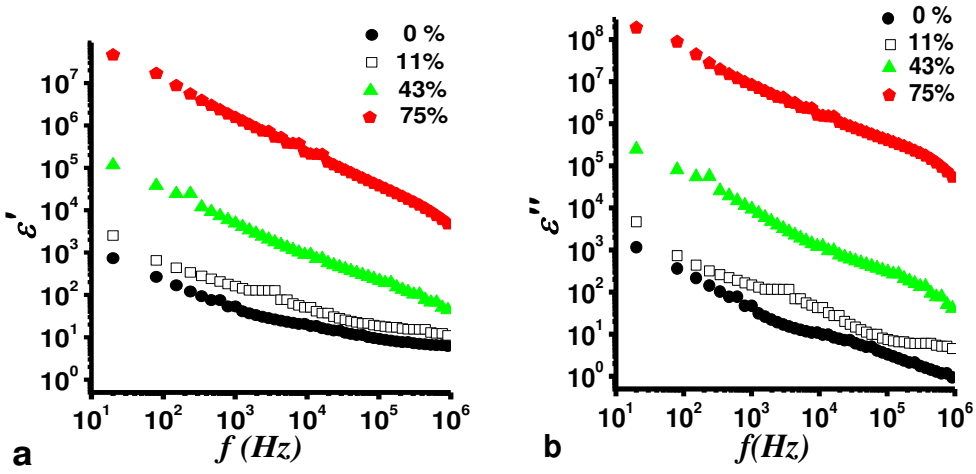

Figure 5.21 a) Dielectric constant and b) dielectric loss at different humidity levels (frequency dependence), for CuPc_TS at room temperature and 25% RH.

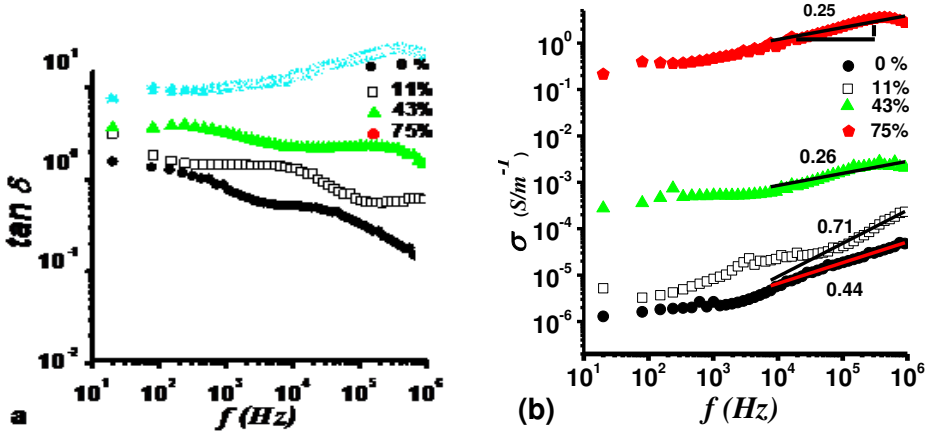

Figure 5.22 a) The dielectric loss tangent and b) electrical conductivity of CuPc_TS. The frequency exponent values for s (slope of graphs) at different relative humidity levels.

The ac conductivity is given by equation 5.2. The s values were derived from the slope of the curves of fig. 5.22b, where the values of s were < 1 (between 0.25 - 0.71). The value of the frequency exponent gives information regarding the type of charge transport mechanism inside the material, which suggests that, a non-Debye relaxation caused by hopping (tunneling of charges);

the charge conductivity was attributed to movement of the proton released from the sulphonated group. Measurements of the CuPc_TS thin film dielectric constant and dielectric loss are shown in fig.5.23, the data shows qualitatively same behavior as seen for pellets in terms of moisture dependence; we can note that the surface is not uniform, but CuPc_TS tends to solidify in long structures that look roughly like tapered cylinders. The aggregation of metalosulphonated phthalocyanine is an important characteristic of this material, due to planarity of the system and the π-π stacking that occurs, which forms stacked aggregates perpendicular to the axis of the plane.[105,106] The aggregation may help to improve the dielectric properties of thin film by providing a lot of interfaces as can be observed from the huge dielectric constant at low frequencies. AFM image of CuPc_TS thin film with 50 nm (RMS=11 nm) thickness is shown in Fig. 24.

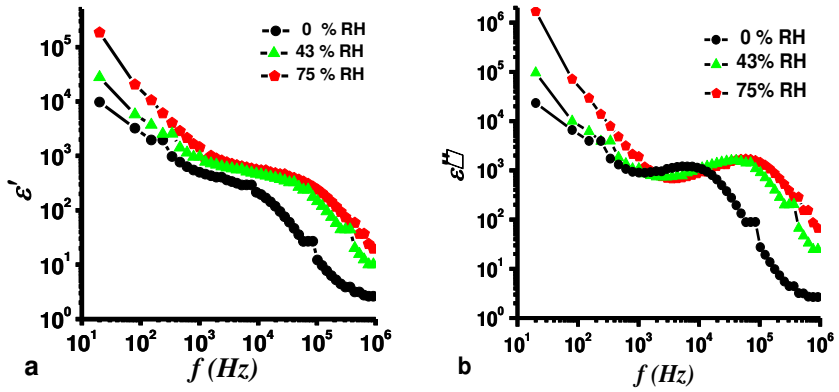

Figure 5.23 a) Dielectric constant and b) dielectric loss for CuPc_TS thin film under various relative humidity conditions.

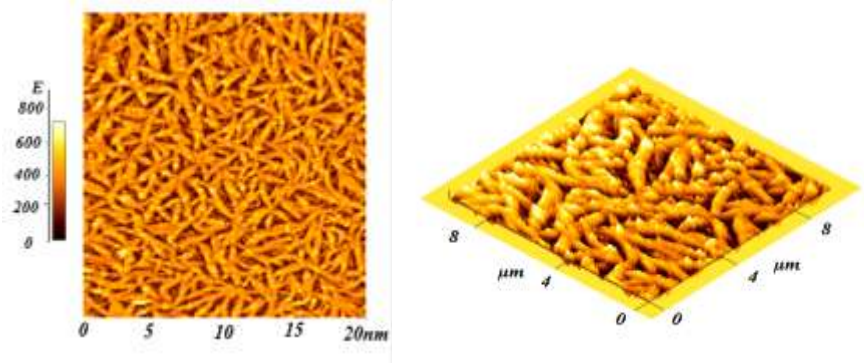

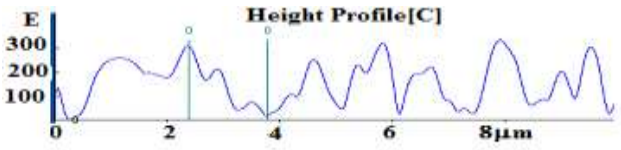

Figure 5.24 AFM surface and thickness measurements of CuPc_TS thin film, RMS=11nm.

Fig. 5.25 shows the results of the Thermogravimetric (TGA) investigation for CuPc_TS material. The material starts losing weight below 100 °C which is attributed to absorbed water. The loss of weight continues up to the point of decomposition at 470 °C, where the material had lost around 10 % of its weight. If the four attached links loses four water molecules then the weight ratio of the water molecules to the total molecular weight of the material (984 g/mol) is about ~8%. So the weight loss is mainly due to the removal of water from the system. The inset shows at what temperature the absorbed water starts leaving the material which is very close to the point where the polarizibility was lost when temperature of the material was raised.

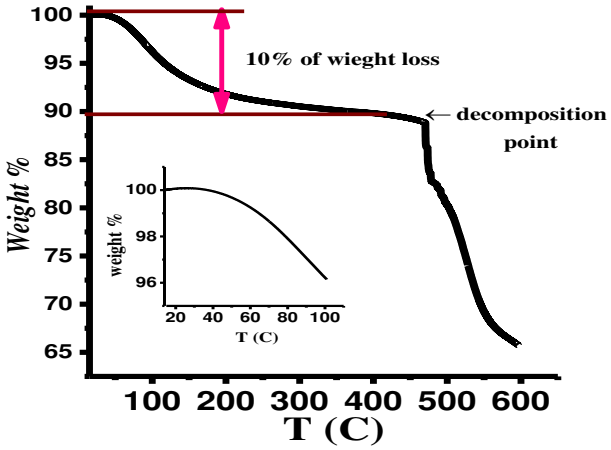

Figure 5.25 Thermogravimetric analysis (TGA) for CuPc_TS.

Fig. 5.26a shows the absorption peaks for CuPc_TS compared to standard CuPc, where the absorption for CuPc_Ts is narrower than standard CuPc in Q-band at 614 nm. CuPc_TS has one single absorption peak in the visible region. Fig. 5.26b shows the CuPc_Ts solution (0.2 M) and thin film absorption peaks are same.

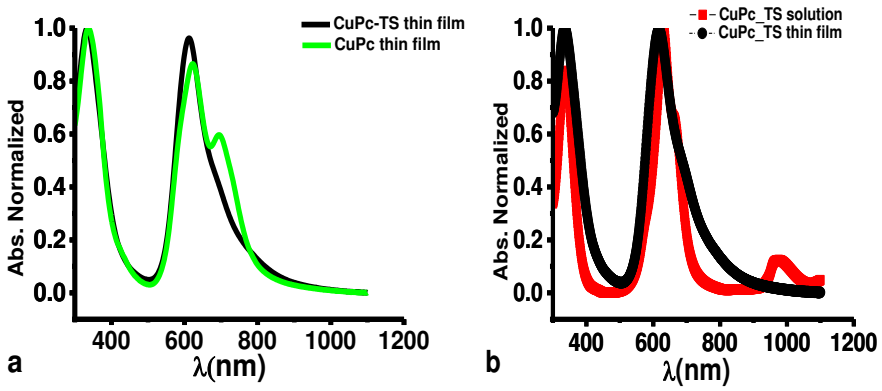

Figure 5.26 Absorption peaks for a) standard CuPc and CuPc_TS b) CuPc_TS in solution and solid states.

5.5 Polyaniline (PANI)

5.5.1 Polyaniline salt (PANI_salt)

The dielectric constant, dielectric loss, and dielectric loss factor for compressed pellets of Polyaniline salt were recorded at room temperature as shown in fig. 5.27, the dielectric constant values were very high reaching 10^8, with a plateau at low-frequency. The dielectric constant decreased almost linearly as the frequency increases, and it reaches a final plateau at high frequencies (close to 1MHz). The dielectric loss is very high and forms a plateau at low frequencies up to 10^3 that's attributed to the higher conductivity of polyaniline salt. The peak of ε' and ε'' had the same plateau at low frequency until suddenly decreasing, which could be due to the effect of the interfacial polarizability between the electrodes and the material, which extends up to 10^3.

Absorption spectra in two different solvents showed different behavior. In ethanol, the PANI-salt does not dissolve totally it was closer to a nano-size composite rather than a solution, the absorption spectrum was broader in the red and infra-red regions and had high values of absolute absorption as shown on fig. 5.28a.

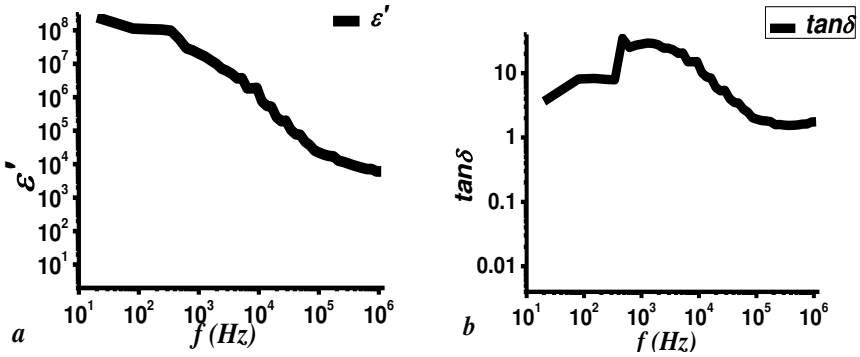

Figure 5.27 Polyaniline salt pellets a) dielectric constant b) tangent loss factor.

The other solvent was sulfuric acid where it dissolves completely but unfortunately the solution cannot be used in practical solar cells due to the ITO surface corrosion. The mixing of the PANI_salt with CuPc_TS resulted in reducing the broader absorption as can be seen from fig. 5.28b, but still extended to the infra-red region edge with absolute absorption reaching 50%. The material in a solar cell did not give a high current, which may be attributed to charge traps. The energy band gap in PANI-salt is small which leads to a fast recombination between generated excitons in the material.

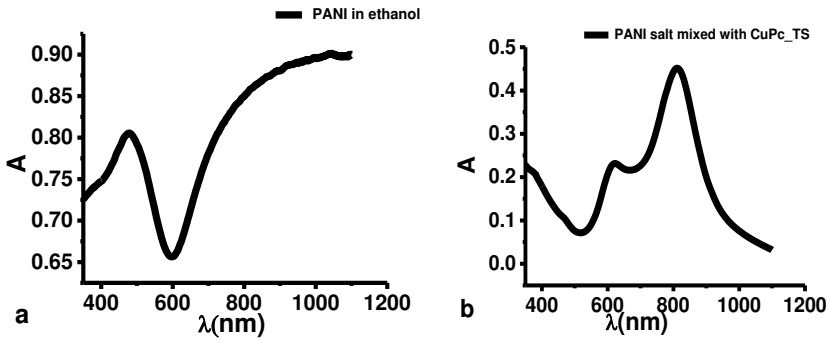

Figure 5.28 Polyaniline salt a) solution in ethanol b) thin film mixed with CuPc_TS.

5.5.2 Polyaniline base (PANI_base)

The dielectric constant measurements for polyaniline base behave similarly to the polynailine salt and modified CuPc, where readings went down as the frequency increased, which is attributed to the space charge or interfacial polarization.

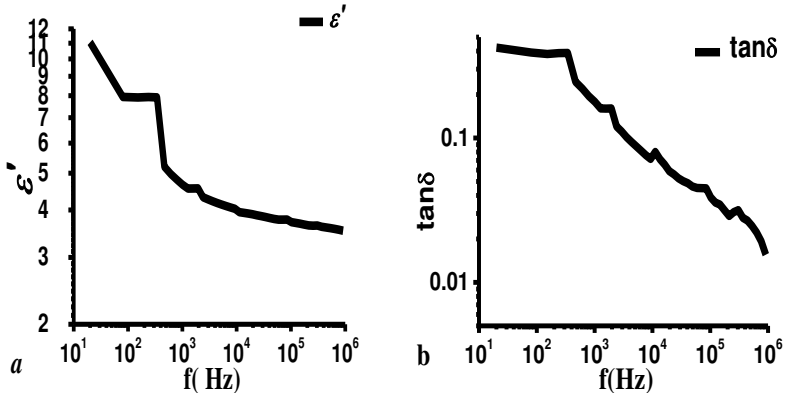

Figure 5.29 Polyaniline base a) dielectric constant b) dielectric loss factor.

CHAPTER VI

ORGANIC PHOTOVOLTAIC CELLS

In this chapter we will discuss the results of organic photovoltaic cell fabrication and characterization, when we used the investigated materials with high dielectric constant discussed in the previous chapter. The bilayer photovoltaic structure was used for our fabricated cells.

Our early values for cells containing CuPc/PTCDI were very low in open circuit voltage and short circuit current and therefore had a low efficiency. Sample I_{sc} values do not exceed 30 µA and V_{oc} was 5 mV, which was attributed to a short between the evaporated upper electrode and the non-etched ITO surface. To overcome the shortage problem PEDOT:PSS was used, which smoothes and improves the conductivity between the active area and the ITO.

To reduce the possibility of a short between the upper and lower electrodes, we etched the required ITO surface where we intend to make the electrodes connector as shown in fig. 6.1a, so the active area will be kept safe from any pressure or epoxy diffusion to the other side (i.e. the ITO).

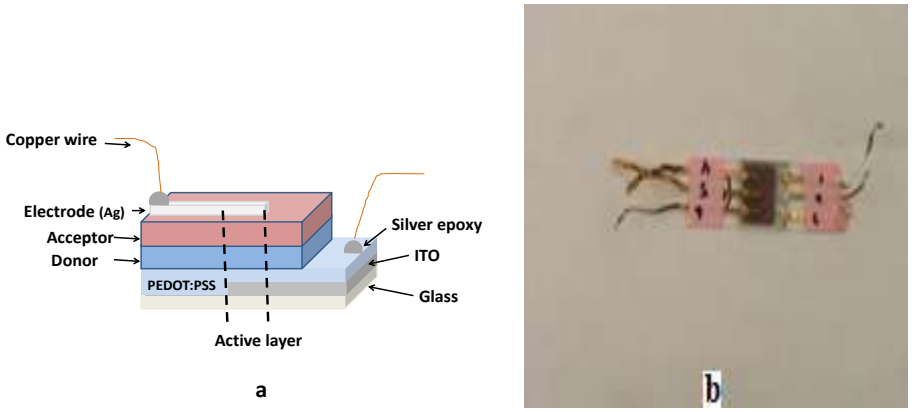

Figure 6.1 Bilayer organic solar cell structure a) cross section b) fabricated solar cell.

The V_{oc} improved significantly to 425 mV (~100 times) and the I_{sc} increased to 100 μA (~3 times). The active area for all cells was 0.08 cm^2 (the overlap area between the bottom and upper electrodes), the efficiency was very poor ~ 0.01.

6.1 Standard CuPc/PTCDI OPVs

The cell structure was ITO/PEDOT:PSS/CuPc/PTCDI/Ag. Different thicknesses of CuPc and PTCDI were evaporated. The PEDOT: PSS layer was constant for all cells. It was spin coated at 500 rpm for 9sec, and then 2500 rpm for 40 sec. The best readings of open circuit voltage and short circuit current were found for cells with CuPc5nm/PTCDI40nm where the efficiency recorded 0.4.

CuPc (nm)	PTCDI (nm)	J(mA/$cm^{2)}$	V_{OC} (mV)	FF	η(%)
2.5	40	1	320	29	0.1
5	10	1.63	420	30	0.2
5	20	1.63	410	29	0.2
5	30	0.9	380	29	0.1
5	**40**	2.85	**489**	**30**	**0.42**
5	60	0.41	408	29	0.05
10	40	1.4	468	28	0.2
15	30	1.34	438	29	0.2
15	40	2.06	220	29	0.13
20	40	1.38	410	29	0.2
30	50	0.35	330	28	0.03

Table 6.1 CuPc(nm)/PTCDI(nm) different thicknesses PV cells V_{oc} and J_{sc}.

Fig. 6.2 shows one of the {PEDOT: PSS/CuPc5nm/PTCDI40nm/BCP6nm/Ag} cells. A fill factor of 28%, V_{oc} of 0.45 V, I_{sc} 1.5 mA/cm^2 and efficiency (η) of 0.2 was recorded.

The low FF value reflects on the curvature of the IV curve which could be attributed to the effect of cell the resistances (series and shunt). The FF factor can be improved using a clean room or a glove box filled with a nitrogen gas through the manufacturing process.

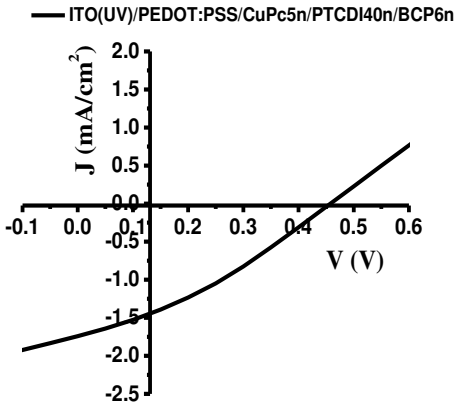

Figure 6.2 J-V characteristic for the cell consists of ITO/PEDOT: PSS/CuPc5nm/PTCDI40nm/BCP6nm.

6.2 Solar cells with the modified CuPc

6.2.1 Octacarboxylic CuPc (CuPc*)

Solar cells with CuPc* have been studied as an active layer. Using CuPc* in our solar cells improved its life time and fill factor. Different external effects on the cells stability had been studied such as oxygen and water content. The results of this material have been published in solar energy materials and solar cells Journal by Elsevier. [78]

6.2.2 Sulphonated CuPc (CuPc_TS)

One promising high dielectric constant material was CuPc_TS. It was spin coated at low speed at 400 rpm and then different high speeds were performed to achieve different thicknesses. Although, we did not have a significant improvement in their efficiency, but it was interesting in terms of increasing cells lifetime compared to other organic solar cells, similar to what we already got with CuPc* cells.

CuPc_TS and PEDOT:PSS dissolve in the same solvent which is water. This makes a problem for us to use them above each other, it was hard to keep PEDOT:PSS on the ITO surface. So we tried to dissolve the CuPc_TS in DMSO (Dimethyl sulphoxide), but the values of the current and voltage were not better than water solution, we tried to use different hole transport layer to avoid the matching solubility problem to replace PEDOT:PSS like spin coated TPD (N,N'-bis (3-

methylphenyl)-N,N'-bis(phenyl)-benzidine), [107] and thermal evaporated tungsten trioxide (WO_3), [108] but this did not work.

We used different materials as n-type with CuPc_TS, to find a good combination with CuPc_TS to reach higher efficieny compared to the old OPV fabricated in our lab. The best values were achieved when we used PTCDA instead of PTCDI as n-type. It achieved a superior a high open cell voltage (V_{oc}= 740 mV) compared to values of the standard CuPc/PTCDA (V_{OC} = 550 mV) or cells with PTCDI.

1) PTCDI

Cell's ID.	Cell structure	Results (average values)			
		J_{sc} (mA/cm^2)	V_{oc} (mV)	FF	η (%)
1	ITO/CuPc_TS(1000-20sec)/PTCDI40nm	0.012	30	25	9×10^{-5}
2	ITO/PEDOT:PSS/CuPc10nm/CuPc_TS1000-30s)/ PCTDI40nm	0.5	110	26	0.01
3	ITO/PEDOT:PSS/CuPc40nm/CuPc_TS(500rpm-18s)/PCTDI 7nm	0.25	200	26	0.013
4	ITO/PEDOT:PSS/CuPc10nm/CuPc_TS(500rpm-18s)/PCTDI 7nm	1.3	200	30	0.08
5	ITO/PEDOT:PSS/CuPc10nm/CuPc_TS(500rpm-18s)/PCTDI 40nm	0.26	160	26	0.01
6	ITO/PEDOT:PSS/CuPc_TS(2500rpm20s)/CuPc10nm /PCTDI 7nm	0.9	140	28	0.04
7	ITO/PEDOT:PSS/CuPc10nm/CuPc_TS(2500rpm-18s)/PCTDI 7nm	1	180	29	0.05
8	ITO/CuPc_TS(1000rpm-60s)/CuPc5nm/PCTDI 40nm/BCP6nm	0.38	450	29	0.05
9	ITO/ CuPc5nm/CuPc_TS(1000rpm-60s)/ PCTDI 40nm/BCP6nm	2	460	32	0.3
10	ITO/ CuPc_TS(2000rpm-60s)/ PCTDI 40nm/BCP6nm	0.13	500	30	0.02
11	ITO/ CuPc_TS(700rpm-60s)/ PCTDI 40nm/BCP6nm	0.13	500	30	0.02
12	ITO/ CuPc_TS(2500rpm-40s)/ PCTDI 40nm/BCP6nm	0.25	580	30	0.04

Table 6.2 CuPc_TS/PTCDI PV cells V_{oc} and J_{sc} average readings and cells duration time.

From table 6.2 we can observe the effect of using the buffer layers on the general performance of the cells, either of hole blocking layer (PEDOT:PSS) or/and electron blocking layer (BCP). Solar

cell parameters improved significantly when we used a buffer layer as can be seen with cells 2 to 7, where PEDOT:PSS was used. The involvement of PEDOT:PSS as a buffer layer has many advantages for organic solar cell performance, [109, 130] but the similarity of solvents between the PEDOT:PSS and CuPc_TS makes it difficult to keep the PEDOT:PSS on the ITO surface. So we tried to introduce a layer of evaporated standard CuPc on the PEDOT: PSS before spin coating the CuPc_TS. When a layer of BCP was evaporated on the top of PTCDI, the V_{oc} jumped significantly as seen on devices 8 to 12. Introducing a buffer layer either an electron or a hole blocking layer has a great influence on the open circuit voltage of the organic solar cells. From the table we can notice the effect of PTCDI thickness on V_{oc}, which increase as the thickness increases. Addition of the standard CuPc layer, make an additional contribution to the output current, the critical thickness of standard CuPc was the 5-10 nm, either before or after spin coating the CuPc_TS.

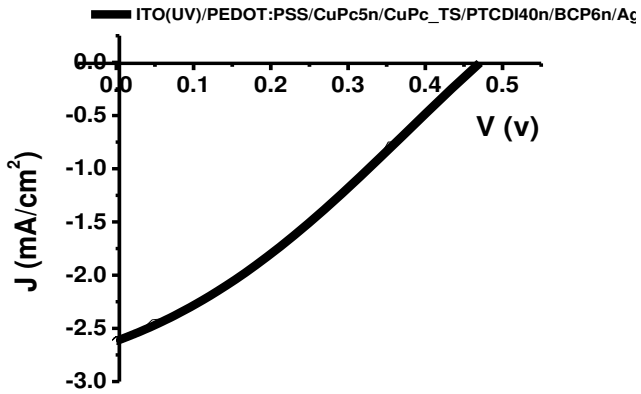

Figure 6.3 J-V curve for cell ITO/PEDOT: PSS/CuPc5nm/CuPc_TS/PTCDI40nm/BCP6nm.

2) PTCDA

Using PTCDA as n-type material is shown in table 6.3. Many tests were done on PTCDA to find the suitable thickness to be used with phthalocyanine layers. In general we used the same thickness as PTCDI which is 40nm. When we used the PTCDA, the open circuit voltage of the devices improved significantly. Using the CuPc_TS as a p-type material shows relatively high voltage and low current as recorded by Schumann *et al.* [72] Similar behavior was recorded for ZnPc_TS, as studied by Rayan *et al.* [73] In their work they used C_{60} as n-type material as a rich electron material;

it can be electrochemically reduced up to 6 electrons. [4, 49] they attributed the low current density due to many factors, the first was the small Δ_{LUMO} between CuPc_TS (ZnPc_TS) and the C_{60} to overcome the exciton bound state by a Columbic force which is in order of ~0.4-1.6eV. [110] The second reason is the absorption spectrum for CuPc_TS is limited to a narrow region in the solar spectrum around 617 nm as shown by fig. 6.5a, which affected the absorption efficiency. In addition, there was high recombination in the CuPc_TS layer. [111] The CuPc_TS was not pure, so there is a large possibility of charge traps, in addition to non uniform thin film after spinning. CuPc_TS aggregated in different directions as we see from the AFM pictures.

We note that V_{oc} also depends on the BCP thickness and the CuPc thickness, which means that the built-in voltage was increased in the cells as predicted by Rajaputra *et al.* [111]

Cell's ID.	Cell structure	Results (average values)			
		J_{sc} (mA/cm^2)	V(mV)	FF	η (%)
I	ITO/ CuPc_TS(2500rpm-40s)/ PCTDA40nm/BCP6nm	0.25	580	29	0.04
II	ITO/ CuPc_TS(2500rpm-40s)/ PCTDA40nm/BCP6nm	0.19	500	28	0.03
III	ITO/CuPc_TS(5000rpm-40s)/CuPc5nm /PCTDA40nm/BCP9nm	0.6	740	32	0.14
IV	ITO/PEDOT:PSS/CuPc_TS(5000rpm-18s)/PCTDA40nm/BCP9nm	0.6	550	31	0.1
V	ITO/CuPc_TS(3000rpm-18s)/PCTDA40nm/BCP9nm	0.4	600	30	0.07
VI	ITO/CuPc_TS(2500rpm-18s)/PCTDA40nm/BCP9nm	0.15	600	28	0.03

Table 6.3 CuPc_TS/PTCDA PV cells V_{oc} and J_{sc} average readings.

Using CuPc_TS with PTCDA without the standard CuPc layer, has advantages on V_{oc}, here we tried to use different CuPc_TS thicknesses to achieve better output current, the best readings was for high speed spinning (at 5000 rpm speed), which means low thickness.

Table 6.4 shows samples of fabricated OPV cells, and it shows how the current had been improved a little bit while the voltage dropped, when we used the PEDOT:PSS. In this case we used a thick layer of standard CuPc to protect the PEDOT:PSS layer. The FF was between 0.25-0.3 and the efficiency was around ~0.07%.

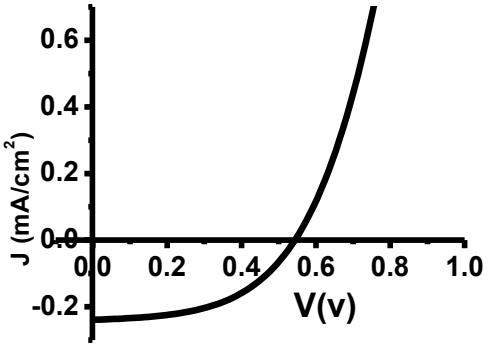

Figure 6.4 J-V characteristics of ITO/CuPc_TS(2500rpm-40s)/PTCDA40nm/BCP6nm.

Cell structure	Results (average values)			
	J_{sc} (mA/cm^2)	V(mV)	FF	η (%)
ITO/ PEDOT:PSS/CuPc25nm/CuPc_TS(4000rpm-60s)/ PCTDA40nm/BCP9nm	0.45	500	30	0.07
ITO/ PEDOT:PSS/CuPc50nm/CuPc_TS(4000rpm-60s)/ PCTDA40nm/BCP9nm	0.37	500	29	0.05
ITO/ PEDOT:PSS/CuPc75nm/CuPc_TS(4000rpm-60s)/ PCTDA40nm/BCP9nm	0.31	500	25	0.04

Table 6.4 ITO/PEDOT: PSS/CuPc/CuPc_TS/PTCDA PV cells V_{oc} and J_{sc} average readings.

The absorbance of the materials involved in the cells structure is shown in fig. 6.5 for CuPc_TS (fig. 6.5a), the PTCDA (fig. 6.5b), and the whole cell (fig. 6.5c), a broader absorbance of the solar spectrum have been achieved 500 nm to almost 700 nm.

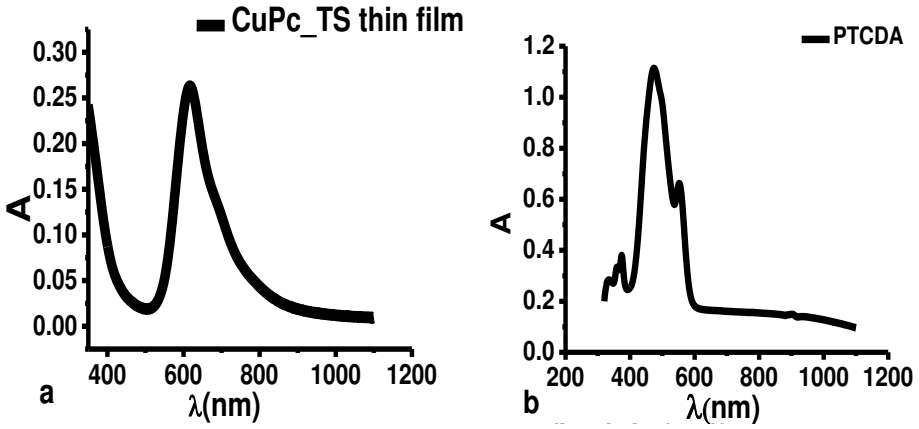

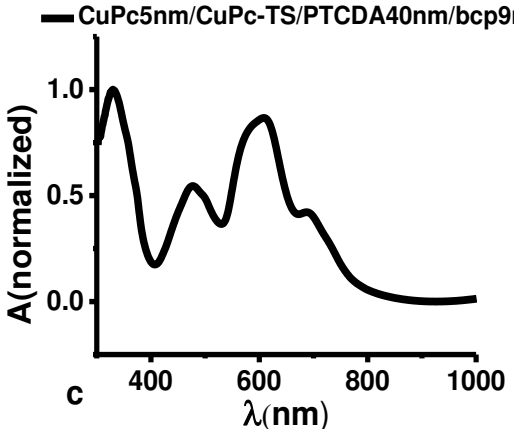

Figure 6.5 Absorption of a) spin coated CuPc_TS, b) thermal evaporated PTCDA, and c) normalized absorbance of the whole cell ITO/CuPc5nm/CuPc-TS/PTCDA40nm/BCP9nm.

3) Fullerene (C_{60})

The C_{60} has been used as small molecule material with regular CuPc as replacement for perelyne derivatives as an electron acceptor (n-type). The C_{60} was thermally evaporated.

Cell structure	Results (average values)			
	J_{sc} (mA/cm^2)	V_{oc} (mV)	FF	η (%)
ITO/ CuPc_TS(2500rpm)/ 350nm C_{60}/9nm BCP	0.25	480	29	0.04
ITO/ CuPc_TS(3000rpm)/ 350nm C_{60}/9nm BCP	0.37	480	30	0.05

Table 6.5 CuPc_TS/ C_{60} PV structure V_{oc} and J_{sc} average measurements.

4) Phenyl-C_{61}-butyric acid methyl ester (PCBM)

PCBM is one of the fullerene derivatives, which was synthesized for the first time in 1995. [112] It has been used for efficient organic solar cells instead of the C_{60} due to its solubility which matches with P3HT (Poly (3-hexylthiophene)), PCBM and P3HT mixture is the most widely used and efficient materials in plastic (printed) solar cells. [113, 114] 50 mg of PCBM were dissolved into 5 ml toluene and dichlorobenzene. We used the dichlorobenzene solution in our cells due to its good solubility and a better thin film formation compared to toluene solutions where aggregation had been observed. Samples were placed in the sonication tub for one hour at 90 C°, solutions were spin coated at 400 rpm for 20 sec then 2500 rpm for 60 sec.

The table 6.6 shows the one of the best samples, where we notice almost the same readings as other materials used before for n-type materials. Not much improvement had been observed, except on the FF where it recorded 60, but unfortunately poor harvested current as shown in fig. 6.6.

Cell structure	Results (average values)			
	J_{sc} (mA/cm^2)	V_{oc} (mv)	FF	η (%)
ITO/CuPc_TS(2500rpm-40s)/PCBM/BCP9nm	0.19	480	60	0.06

Table 6.6 ITO/CuPc_TS/PCBM PV structure V_{oc} and J_{sc} average measurements.

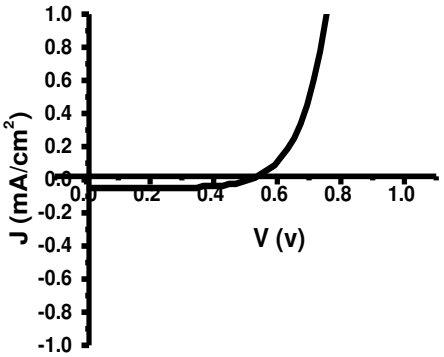

Figure 6.6 J-V curve for ITO/CuPc_TS (2500rpm-40s)/PCBM/BCP9nm.

6.3 Polyaniline solar cells

Polyaniline (PANI) was one of our choices to achieve the higher efficiency due to its high dielectric constant. Polyaniline and CuPc derivatives have been already used to prepare high dielectric constant materials, their composites were employed for electrostriction due to their flexibility which is one of the organic materials advantages.[39, 48] By adding the polyaniline to the CuPc_TS, we tried to improve the excitons medium by improving the permittivity constant, a similar approach was done by other researchers to mix organic materials with inorganic (hybrid solar cells) to improve cells efficiency like mixing P3HT with CdTe nanorods. [115]

Generally, our fabricated cells with PANI only as a donor were not efficient, the generated current was very low about 5μA, but voltage was around 500 mV using evaporated C_{60} as n-type. Then polyaniline solution (into N-Methylpyrrolidone (NMP)) was mixed with the CuPc_TS (water solution) into different ratios by volume (8%, 16%, and 24%), "0.2, 0.4, 0.6 ml polyaniline into 2.5 ml of 0.02 M CuPc_TS" the results except for the 8% samples did not work.

In general PANI-salt thin films were not smooth, because of the poor solubility and miscibility with organic solvents, it tends to aggregate and make pinhole layers. We tried to use chemical polymer binders like ethocel STD-4 and polyox WSR N-80 from Dow chemical's to increase PANI solution viscosity and make better thin film layer. But we noticed a sharp decrease of the PANI thin film surface conductivity using four probes measurements. Fig. 6.7 shows some results of using the PANI in the solar cell, the harvested photocurrent still low; the overall performance is poor where efficiency was 0.05%.

Cell structure	Results (average values)			
	J_{sc} (mA/cm^2)	Voc (mV)	FF	η (%)
ITO/ 0.4polyaniline:CuPc_TS(5000rpm-40s)/350nmC_{60}/BCP7nm	0.19	397	28	0.02
ITO/ 0.6polyaniline:CuPc_TS(5000rpm-40s)/350nmC_{60}/BCP7nm	0.19	470	29	0.03

Table 6.7 CuPc_TS/PANI PV structure V_{oc} and J_{sc}.

6.4 Solar cells stability

One of the advantages that we observed during our research on modified CuPc materials was the stability of our cells compared to what reported for polymer solar cells or other small molecules solar cells. Generally OPV devices when examined after fabrication always suffer from poor performance and terrible stability. The reason that the organic photovoltaics have not been disregarded yet is the possibility of very promising low cost, easier fabrication and the use of very abundant materials which in case of succeed makes a giant step towards a development of the ultimate energy technology. Researchers are trying to find new methods and material to get higher OPV efficiencies, and at the same time they are studying its stability which is an important

parameter as well as the efficiency for commercialization. A stable solar cell is cell with no change in performance over time regardless of the conditions that it is exposed to. Studying the stability of solar cells is usually easy and directly observed through the solar cell performance. But, to understand the factors under which conditions stable cells can fail, cells need to be studied with different relative humidity conditions, different illumination period, varying light intensity and high temperatures or any combination of those conditions. [116] Recently, some studies have been made to understand the reasons and mechanisms behind degradation of OPVs. [117, 118, 119, 120] The reason behind unencapsulated OPV cells degradation is likely to be due to the oxygen diffusion into the material where electrons are trapped. [117] Water absorption by solar cell materials like PEDOT:PSS, [118, 120] using unstable materials such for buffer layers or active layers and finally electrodes oxidization. [119, 121]

Lifetime stability of up to 2000h under continuous illumination has been reported for devices protected from oxygen and water. [122] Krebs made polymer solar cell under ambient conditions without vacuum or fullerene which when stored in the dark lasts for 6 months. [123] It can be noticed from different literature that the OPV device performance is enhanced slightly during the first few hours after being removed from the vacuum. Usually, this trend is thought to be caused by an annealing effect in polymer solar cells which are usually a bulk heterojunction structure. The highest open-circuit voltage, short-circuit current density and efficiency all appeared an hour after fabrication. [119, 124 , 130]

In the earlier polymer solar cells which contain the poly-phenylenevinylene (PPV) type, the main source of degradation was the photochemical reaction (the photo oxidation). [125] Later it was replaced by P3HT which is stabile relative to PPV, especially when PCBM was added to it. [126] Oxygen was the reason for degradation as reported by Manceau *et al*. [127] and Motaung *et al*. [128] Many types of new materials which show a superior stability to P3HT had been synthesized. For more details about these materials, see the literature review by Jorgensen *et al*. [129] The stability is still limited to ~4000 hours, under full sun 100 mA/cm. [2, 126]

In our organic solar cells, we found very poor values for open circuit voltage and short circuit current when removed from the vacuum chamber. Characteristic values improved gradually with time to reach their maximum values of V_{oc} and J_{sc} after days, and then kept steady on average for more than 8 months (figs. 6.8 and fig. 6.10). We studied CuPc modified by sulphonated functional groups (CuPc_TS) and a perylene derivative PTCDI and PTCDA, we used a BCP as a buffer layer (an exciton blocking layer EBL), which improved the performance of OPV's efficiency [49, 130] and protects the active materials by blocking the hot electrode atoms. [131] The PTCDA was used due to its long exciton diffusion length (880 ± 60A°) [132] and deep HOMO/LUMO level (2.1eV). [133, 134]

Energy level diagrams for the materials involve in our cells is shown in fig. 6.7.

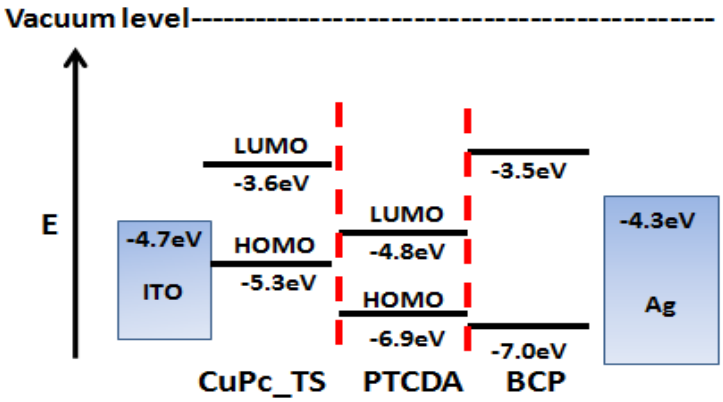

Figure 6.7 Energy level diagram for cell components.

For sulphonated CuPc, many cells have been fabricated; some devices had the standard CuPc to increase the harvested current. The open circuit voltage was recorded and compared to regular CuPc/perylene derivatives. Table 6.8 shows cells structure fabricated where two kinds of structure have been used one with PEDOT:PSS (cell C) and the other is free of PEDOT:PSS (cell A, B, D). J_{sc} and V_{oc} were recorded as an average value after stabilization. Cells free of PEDOT:PSS exhibits higher V_{oc} and more stability compared to cells with PEDOT:PSS.

Cell	Samples structure	J_{sc} (mA/cm^2)	V_{oc} (mV)	FF	η (%)	Time (months)
A	ITO/ CuPc_TS(1000rpm-40s)/ CuPc5nm/PCTDA55nm/BCP9nm	0.25	700	26	0.05	9
B	ITO/ CuPc_TS(5000rpm-40s)/ CuPc5nm /PCTDA40nm/BCP9nm	0.6	740	32	0.14	9
C	ITO/PEDOT:PSS/CuPc_TS(5000rpm40s)/PCTDA40nm/BCP9nm	0.5	550	28	0.08	8
D	ITO/CuPc_TS(3000rpm-40s)/PCTDA40nm/BCP9nm	0.38	600	27	0.06	9

Table 6.8 Devices structure with PTCDA layer as n-type.

Figures 6.8, 6.9 and 6.10 shows an interesting behavior of the cells parameters, where the performance increases gradually with time, the average time it took the devices to reach its maximum readings was 3-7 days, then keep steady in average (a little fluctuations around the maximum value). The average time for light exposure on our cell was from 15 to 20 minutes to measure the cell parameters, and then it was left under ambient environment until failed.

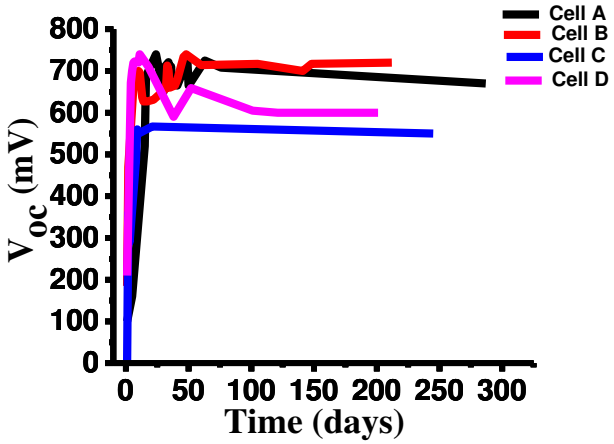

Figure 6.8 V_{oc} as a function of time for devices involved PTCDA.

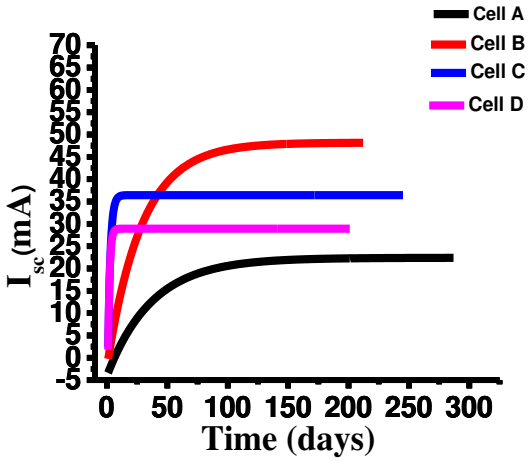

Figure 6.9 Fitted I_{sc} values as function of time.

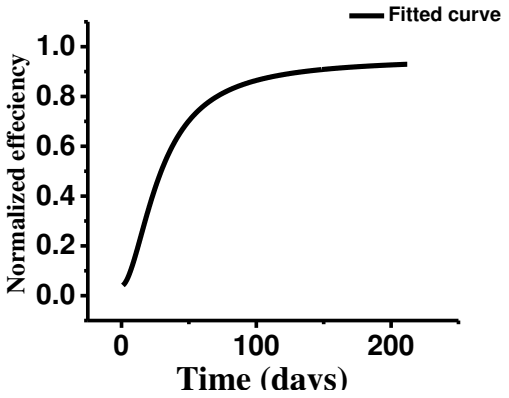

Figure 6.10 General efficiency behavior of our cells versus time.

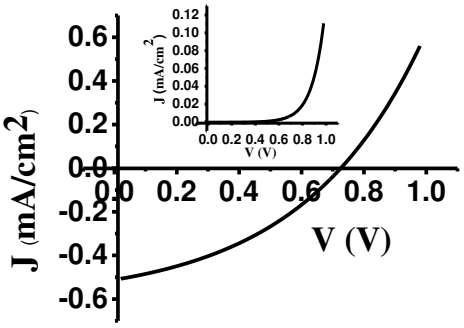

Figure 6.11 J-V curve under illumination and when dark for cell A.

The nature of the open circuit voltage, V_{oc} is theoretically known. In general devices made by electron donor and acceptor organic layers, the V_{oc} is given by the difference between the highest occupied molecular orbital of the electron donor ($HOMO_D$) and the lowest unoccupied molecular orbital of the electron acceptor ($LUMO_A$) that is to say Δ ($HOMO_D$–$LUMO_A$), [135, 136] Rand *et al*. [137] found a linearly relationship between the energy levels offset and the open circuit voltage for small molecules bilayer heterojunction cells; the same relationship was found by Scharber *et al*. [138] for bulk heterojunction cells.

Samples A and B were studied under different storage environments vacuum, 0% RH, and 75% RH; during the period of testing, The observed collected output current decreased, which is expected due to increasing in the trapping sites and scattering centers in the cell. The open circuit voltage increased by 20%.

The other devices made using PTCDI, do not show the same stability as devices with PTCDA, some had 60 days stability but less V_{oc} values as shown in table 6.9. We used the same thicknesses as used for PTCDA cells.

Other workers such as Song *et al*. [139] studied the stability of for a small molecules based on $CuPc/C_{60}$ with power conversion efficiency of 0.24% for three days. The device efficiency dropped by 40% in the first half hour after fabrication until they failed by the third day. In our samples with almost the same efficiency (0.29 %), the cells efficiency was going up. We can see from table 6.9

that sample 2 lasts for 6 days. In our devices we used BCP as an EBL which did not show a degradation as had been published when it used by other workers. [140, 141]

Cell	Sample structure	J_{sc} (mA/cm^2)	V_{oc} (mV)	FF	η (%)	Average time (days)
1	ITO/CuPc_TS(1000rpm-60s)/CuPc(5nm)/PCTDI 40nm/BCP6nm	0.38	450	29	0.05	12
2	ITO/CuPc(5nm)/CuPc_TS(1000rpm-60s)/PCTDI 40nm/BCP6nm	1.9	460	32	0.28	6
3	ITO/CuPc_TS(700rpm-60s)/PCTDI 40nm/BCP6nm	0.13	500	26	0.02	10
4	ITO/CuPc_TS(2000rpm-60s)/PCTDI 40nm/BCP6nm	0.13	500	26	0.02	60
5	ITO/CuPc_TS(2500rpm-40s)/PCTDI 40nm/BCP6nm	0.25	580	30	0.04	60

Table 6.9 Devices structure with PTCDI layer as n-type.

Cell B was exposed to continuous illumination for three hours; we observed a gradual decreasing of mainly the cell current, the voltage was decreased only slightly with time. In the vacuum chamber the current was increased which may indicate that water molecules had been released from the cells which reduce the trapping sources in the cell and decrease series resistance.

CHAPTER VII

CONCLUSION

The dielectric constant values of standard CuPc, hyperbranched CuPc and modified CuPc by sulphonated or carboxylic groups were studied as a function of frequency from 20 Hz to 1 MHz and temperature from 20 C° up to 120 C°. The high dielectric constant values associated with the monomer CuPc ($>10^5$ at 1 KHz) was similar to dielectric constant values reported for tetramer or oligmer CuPc (whose structure was incorrectly reported). The effect of the functional groups on the large dielectric constant values for modified CuPc were attributed to the easily ionization of acidic groups into a hydroniom ions under the existence of moisture. These ions contribute to the huge orientational polarization in the material, was behind the large dielectric constant observed at frequency range 20Hz- 1MHz. The ellipsometry measurements on modified CuPc materials in addition to measurements on the standard CuPc show that the dielectric constant values are not an intrinsic property of these materials, but due to extrinsic factors. The hyberbranched CuPc shows an interesting behavior of the dielectric constant values which was steady under frequency and temperature variation. The dielectric loss factor was small recording 0.001 at high frequencies and 100 C° which could be used for electrical and capacitance applications. Applying modified CuPc into an organic solar cells leads to an interesting improvement into their stability rather than increasing its efficiency. CuPc_TS/PTCDA Solar cell leads to a significant improvement on the open circuit voltage (740 mV) compared to cells with standard CuPc (550 mV), in addition to a superior stability of the cells for at least 8 months.

Appendix A

Surface topography and thickness measurements

CuPc_TS samples were spin coated on glass (fisher microscope slides), topography and thickness (if any) was found using Atomic Force Microscope (AFM) from ThermoMicroscopes Auto Probes, thickness measurements was taken by making a grave on the sample (scratched) to reach the sample substrates:

i) CuPc_TS with water solvent with concentration of 0.2M:

1) At 1000 rpm/1min, thickness ~ 40 nm, RMS= 11 nm

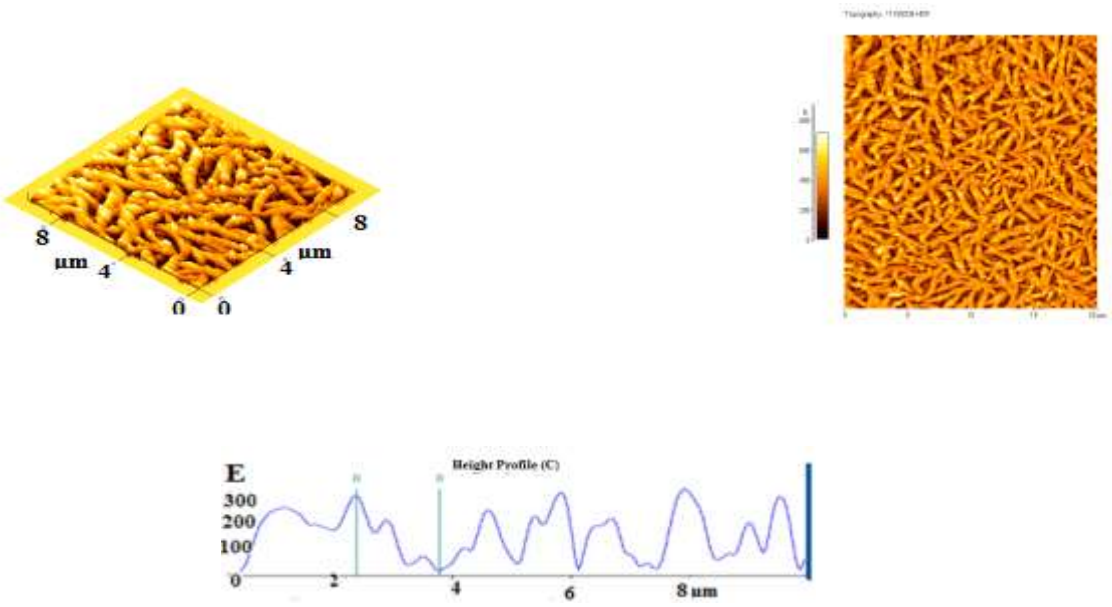

Fig. A.1 CuPc_TS in water (0.2M) At 1000 rpm/1min, thickness ~ 40 nm, RMS= 11 nm.

2) At 2000rpm/1min, thickness ~ 25 nm, RMS=8 nm

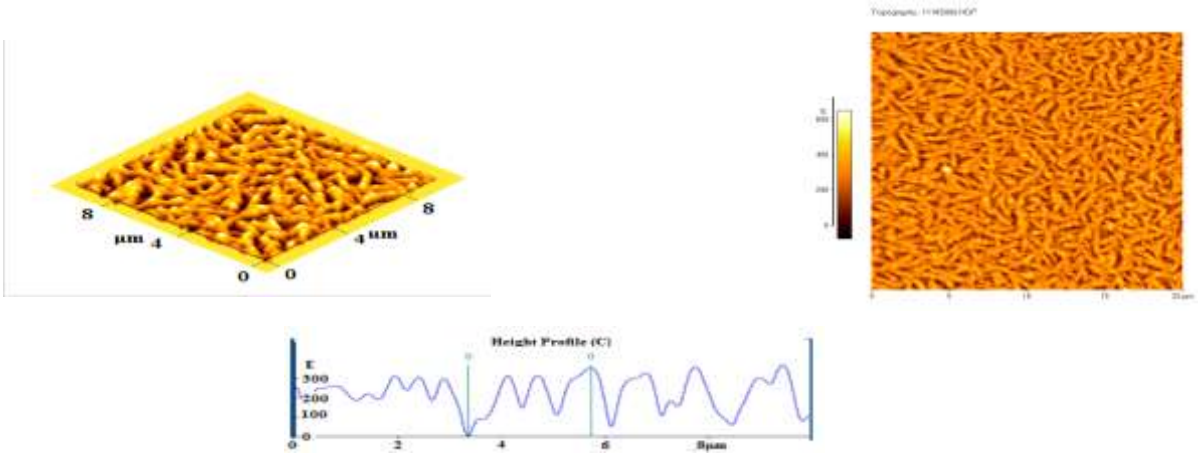

Fig. A.2 CuPc_TS in water (0.2M) At 2000rpm/1min, thickness ~ 25 nm, RMS=8 nm.

3) At 300rpm/20sec then 700rpm/1min, Thickness ~ 50 nm, RMS=1.4 nm

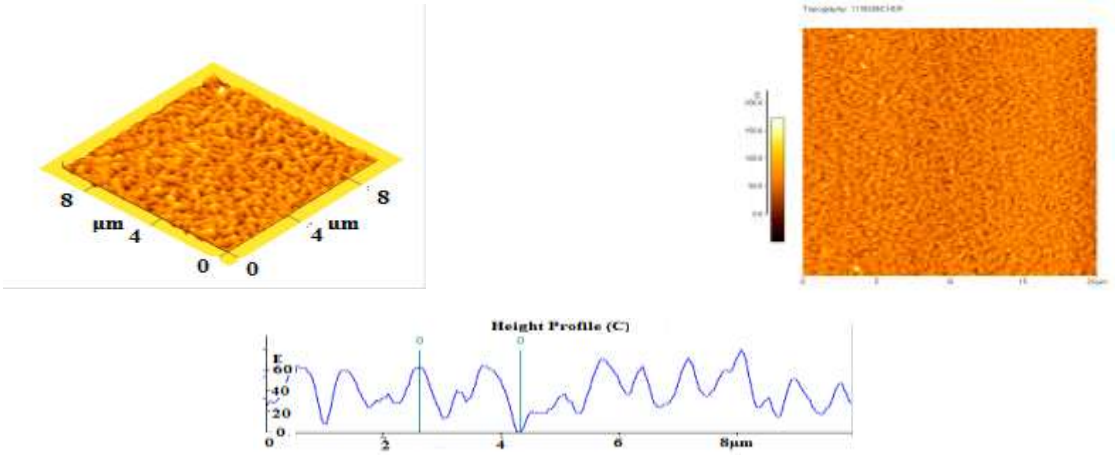

Fig. A.3 CuPc_TS in water (0.2M) At 300rpm/20sec then 700rpm/1min, thickness ~ 50 nm, RMS= 1.4 nm.

ii) CuPc_TS with DMSO as a solvent:

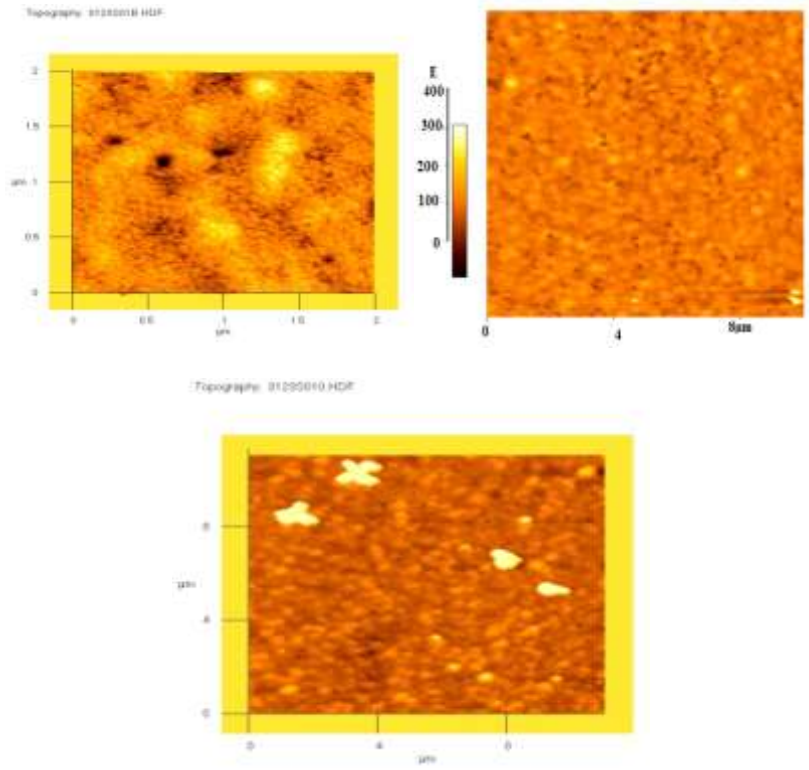

Fig. A.4 Surface morphology for CuPc_TS in DMSO.

We can note the difference between CuPc_TS water and DMSO solutions thin films where cylindrical tubes had gone in DMSO solution more “grainy” shape as shown by AFM pictures.

Appendix B

Ellipsomertry

1. Introduction

Ellipsometry is a non-destructive measurement technique, which it can be used to obtain optical properties of materials by means of reflected light waves. The technique measures a relative change in polarization and is therefore not dependent on absolute intensity as long as the absolute intensity is sufficient. A linearly polarized light at an angle incidence to a surface changes polarization state when it is reflected. It becomes elliptically polarized, that is why it is called "ellipsometry". We have a Gartner model L126B with HeNe light source (633nm) operated manually based on photometric ellipsometry.

2. Theoretical background

There are different kinds of ellipsometry depending on how the ellipsometry is arranged and optical components are used. We used photometric ellipsometry with a rotating analyzer ellipsometer (RAE) where the intensity is measured at the detector at different analyzer angles. In photometric ellipsometry one or more conditions are varied while the light intensity at the detector is measured. Zero light intensity is not necessary at the photometric detector like null ellipsometry.

3. Determination of ellipsometric parameters Δ and Ψ

We will follow ref. 142 and ref. 143 to show the theoretical background of calculations of ellipsometric parameters Δ and Ψ used to find the physical properties n (refractive index) and ε (optical dielectric constant).

Fig. A1 Shows a linearly polarized light source using Glan–Thomson prism; which then passes through a fixed polarizer at 45°.

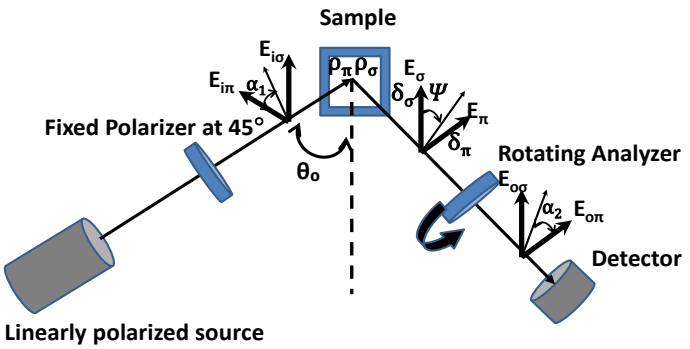

Figure B.1 RAE ellipsometer parameters.

The Jones vector of the light wave after the polarizer $E_i^{\sigma\pi}$ is:

$$\mathbf{E}_i^{\sigma\pi} = \begin{bmatrix} E_{i\pi} \\ E_{i\sigma} \end{bmatrix} = \begin{bmatrix} E_i \cos\alpha_1 \\ E_i \sin\alpha_1 \end{bmatrix} \tag{A.1}$$

Where E_i is the magnitude of the Jones vector $E_i^{\sigma\pi}$ and α_1 is the azimuth angle of the polarizer measured from the direction of the π eigenvector. The light is reflected by the surface, which in Jones notation corresponds to multiplication by the Jones matrix of the surface:

$$\mathbf{T}_s^{\sigma\pi} = \begin{bmatrix} \rho_\pi & 0 \\ 0 & \rho_\sigma \end{bmatrix} \tag{A.2}$$

Next the Jones vector of the light wave after the surface must be rotated to the coordinate system of the analyzer by the Jones transform matrix:

$$\mathbf{R}(\alpha_2) = \begin{bmatrix} \cos\alpha_2 & \sin\alpha_2 \\ -\sin\alpha_2 & \cos\alpha_2 \end{bmatrix} \tag{A.3}$$

With the Jones vector given in the coordinates system of the analyzer the Jones matrix of the analyzer is given by:

$$\mathbf{T}_A = \begin{bmatrix} 1 & 0 \\ 0 & 0 \end{bmatrix} \tag{A.4}$$

If the analyzer is consider to be ideal. The Jones vector at the detector can be written as:

$$\mathbf{E}_o = \mathbf{T}_A^{te}\mathbf{R}(\alpha_2)\,\mathbf{T}_s^{\sigma\pi}\mathbf{E}_i^{\sigma\pi} = \begin{bmatrix} 1 & 0 \\ 0 & 0 \end{bmatrix}\begin{bmatrix} \cos\alpha_2 & \sin\alpha_2 \\ -\sin\alpha_2 & \cos\alpha_2 \end{bmatrix}\begin{bmatrix} \rho_\pi & 0 \\ 0 & \rho_\sigma \end{bmatrix}\begin{bmatrix} E_i\cos\alpha_1 \\ E_i\sin\alpha_1 \end{bmatrix}$$

$$= \begin{bmatrix} cos\alpha_2\ \rho\pi\ \ Ei\ \ cos\alpha_1 + sin\alpha_2\ \ \rho\sigma\ \ Ei\ \ sin\alpha_1 \\ 0 \end{bmatrix} = \begin{bmatrix} cos\alpha_2\ E\pi + sin\alpha_2\ E\sigma \\ 0 \end{bmatrix} \quad (A.5)$$

Where $E_\pi = \rho_\pi\ E_i\ cos\alpha_1$ and $E_\sigma = \rho_\sigma\ \ E_i\ \ sin\alpha_1$.

The light wave intensity at the detector is given by

$$\mathbf{I}o = \mathbf{E}_o^\dagger \mathbf{E}_o = [cos\,\alpha_2\ E_\pi^* + sin\,\alpha_2\ E_\sigma^* \quad 0] \begin{bmatrix} cos\alpha_2\ E\pi + sin\alpha_2\ E\sigma \\ 0 \end{bmatrix}$$

$$= (\cos\alpha_2)^2 E_\pi^* E_\pi + (sin\,\alpha_2)^2 E_\sigma^* E_\sigma + cos\,\alpha_2\ sin\,\alpha_2\ (E_\pi\ E_\sigma^* + E_\pi^* E_\sigma\ ) \quad (A.6)$$

Using trigonometric functions we can rewrite equation as:

$$\mathbf{I}o = \frac{1}{2}\{\left(E_\pi^* E_\pi\ + E_\sigma^* E_\sigma\ + (E_\pi^* E_\pi\ - E_\sigma^* E_\sigma\ )\ (2\cos\alpha_2) + \left(E_\pi^* E_\pi\ + E_\sigma^* E_\sigma\ \right)(2\ sin\ \alpha_2)\}$$

$$= \frac{1}{2}\{S1 + S2\ (2\ \cos\alpha_2) + S3\,(2\ sin\ \alpha_2)\} \quad (A.7)$$

Where $S_1 = E_\pi^* E_\pi$, $S_2 = E_\pi^* E_\pi\ - E_\sigma^* E_\sigma$ and $S_3 = E_\pi^* E_\pi\ + E_\sigma^* E_\sigma$

From equation 7 we can get simple equations for intensity at the detector at different analyzer angles starting from 0° increased by 45° each time which will give simple expressions in terms of S1, S2, and S3

$$I_o\,(0°) = \frac{1}{2}(S1 + S2) \quad (A.8)$$

$$I_o\,(45°) = \frac{1}{2}(S1 + S3) \quad (A.9)$$

$$I_o\,(90°) = \frac{1}{2}(S1 - S2) \quad (A.10)$$

$$I_o\,(135°) = \frac{1}{2}(S1 - S3) \quad (A.11)$$

Combining these equations and rewrite using expressions for $E_\pi^*, E_\pi\ , E_\pi\ , E_\sigma\ , E_\sigma^*$ in terms of reflection coefficients ρ_π ,ρ_σ

$$\cos(2\Psi') = -\frac{S2}{S1} = \frac{Io\,(90°) - Io\,(0°)}{Io\,(90°) + Io\,(0°)} \quad (A.12)$$

$$\sin 2\Psi'\ \cos\Delta = \frac{S3}{S1} = \frac{Io\,(45°) - Io\,(135°)}{Io\,(90°) + Io\,(0°)} \quad (A.13)$$

where $\tan\Psi' = \frac{\tan\Psi}{\tan\alpha 1}$, in our case where polarizer angle fixed at $\alpha_1 = 45°$ then

$$\tan\Psi' = \tan\Psi \quad (A.14)$$

Then $\Psi' = \Psi$

I used Maple software for calculations, starting with known material like silicon to check our ellipsometer is working properly using refractive index formula (n):

$$n = \frac{\left[\sqrt{1-4(\sin\theta_0)^2\tan\Psi e^{i\Delta}+2\tan\Psi e^{i\Delta}+(\tan\Psi)^2 e^{i\Delta}}\right] n_0 \sin\theta_0}{\cos\theta_0(1+\tan\Psi e^{i\Delta})} \quad \text{(A.15)}$$

Where n is the complex index of refractive of the material and n_o is air refractive index =1 and dielectric constant is given by

$$\varepsilon = (\sin\theta_0)^2 + (\sin\theta_0)^2.(\tan\theta_0)^2.\left[\frac{1-\rho}{1+\rho}\right]^2 \quad \text{(A.16)}$$

Or simply using Maxwell's equations

$$\varepsilon = n^2 \quad \text{(A.17)}$$

BIBLIOGRAPHY

1) http://www.oecd-ilibrary.org/economics/oecd-factbook-2010/world-electricity-generation-by-source-of-energy-figure_factbook-2010-graph119-en, (2011).

2) W. Brutting, “Physics of Organic Semiconductors”, Wiley-VCHVerlag, GmbH & Co.KGaA, Weinheim, Germany, (2005).

3) M. Pope, C. E. Swenberg, “Electronic Processes in Organic Crystals and Polymers”, 2nd ed., Oxford University Press, N.Y, (1983).

4) S. Sun, N. S. Sariciftci, “Organic Photovoltaics Mechanisms, Materials, and Devices”, Taylor & Francis Group, LLC, (2005).

5) F. So, “Organic Electronics; Materials, Processing, Devices and Applications”, CRC Press, Taylor & Francis Group, (2010).

6) ftp://ftp.cordis.europa.eu/pub/fp7/energy/docs/weto-h2_en.pdf, (2012).

7) http://www.worldenergy.org/documents/scenarios_study_online.pdf, (2012)

8) C. J. Barbec, V. Dyakonov, J. Parisi, N. S. Sariciftci, “Organic photovoltaics concepts and realization”, Springer, Berlin, (2003).

9) B. A. Gregg, S. C. Chen, R. A. Cormier, “Coulomb Forces and Doping in Organic Semiconductors”. Chem. Mater., 16, 4586-4599, (2004).

10) C. W. Tang, “Two-layer organic photovoltaic cell”, Appl. Phys. Lett., 48, 183–185, (1986).

11) F. Yang, K. Sun and S. R. Forrest, "Efficient solar cells using all-organic nanocrystalline networks," Adv. Mater. 19, 4166-4171, (2007).

12) J. Xue, S. Uchida, B. P. Rand, S. R. Forrest, "Asymmetric tandem organic photovoltaic cells with hybrid planar-mixed molecular heterojunctions", Appl. Phys. Lett. 85, 5757-5759, (2004).

13) http://www.heliatek.com/?p=1923&lang=en., (2013)

14) J. Y. Kim, K. Lee, N. E. Coates, D. Moses, T. Q. Nguyen, M. Dante, and A. J. Heeger, "Efficient Tandem Polymer Solar Cell Fabricated by All-Solution Processing", Science, 317, 222, (2007).

15) M. A. Green, K. Emery, Y. Hishikawa, W. Warta, "Solar cell efficiency tables (version37)" Prog. Photovolt, Res. Appl., 19, 84–92, (2011).

16) C. Lungenschmied, G. Dennler, H. Neugebauer, S. Sariciftci, M. Glatthaar, T. Meyer, A. Meyer, "Flexible long-lived large-area organic solar cells", Solar Energy Materials and Solar Cells, 91, 379-384, (2007).

17) D. S. Ginger, N. C. Greenham, "Photoinduced electron transfer from conjugated polymers to CdSe nanocrystals", Phys. B, 59, 624–629, (1999).

18) H. Gommans, S. Schols, A. Kadashchuk, P. Heremans, "Exciton Diffusion Length and Lifetime in Subphthalocyanine Films", Phys. Chem. C, 113, 2974–2979, (2009).

19) A. E. Becquerel, "Mémoire sur les effets électriques produits sous l'influence des rayons solaires", Compt. Rend. Acad. Sci., 9, 561, (1839).

20) S. R. Wenham, M. A. Green, M. E. Watt, R. Corkish, "Applied Photovoltaics", Earthscan, 2nd Ed., (2007).

21) J. Nelson, "The physics of solar cells", Imperial College Press, (2003).

22)http://4.bp.blogspot.com/_fa6AZDCsHnY/S_xmXr6HTaI/AAAAAAAAACw/weKj6XTaf4M/s1600/Solar_Spectrum.png, (2012).

23) http://www.astm.org/Standards/E927.htm, (2010).

24) J. M. Halls, R. H. Friend, "Organic Photovoltaic Devices", Clean Electricity from Photovoltaics, Imperial College Press, London, 377-445, (2001).

25) M. Knupfer, "Exciton binding energies in organic semiconductors", App. Phys. A, 77, 623-626, (2003).

26) C. Klingshirn, "Semiconductor optics; Springer", 3rd Ed., (2007).

27) H. Ibach, H. Luth, “Solid-State Physics: An Introduction to Principles of Materials Science”, Springer; 4th Ed., (2009).

28) M. Grundmann, “The Physics of Semiconductors, An Introduction Including Devices and Nanophysics”, Springer, 1st Ed., (2006).

29) P. Yu, “M.Cardona;Fundamentals of semiconductors: physics and materials properties”, Springer; 3rd Ed., (2005).

30) C. Hamaguchi, “Basic semiconductor physics”, Springer, 2nd Ed., (2010).

31) D. D. Sell, “Resolved Free-Exciton Transitions in the Optical-Absorption Spectrum of GaAs”, Phys. Rev. B 6, 3750–3753, (1972).

32) N. Shi, R. Ramprasad, “Dielectric properties of Cu-phthalocyanine systems from first principles”, Appl. Phys. Lett., 89, 102904, (2006).

33) N. Ueno, K. Sugita, “Parabolic dispersion and effective mass of hot electrons in oriented thin films of copper phthalocyanine determined by means of low-energy-electron transmission”, Phys. Rev. B. 44, 6472–6476, (1991).

34) K. M. Kadish, K. M. Smith, R. Guilard "The Porphyrin Handbook: Applications of Phthalocyanines”, Vol. 19, Elsevier, U.S.A (2003).

35) I. G. Hill, A. Kahn, Z. G. Soos, R. A. Pascal Jr., “Charge-separation energy in films of π-conjugated organic molecules”, Chem. Phys. Lett., 327, 181, (2000).

36) http://www.tf.unikiel.de/matwis/amat/admat_en/backbone.pdf., (2012).

37) R. P. Feynman, R. B. Leighton, M. Sands, “The Feynman Lectures on Physics”, Adison Wesley, Reading, PA, Chap. 11 (1966).

38) D. Griffiths, “Introduction to electrodynamics”, Prentice-Hall, 3rd Ed., (1999).

39) K. C. Kao, “Dielectric Phenomena in Solids with Emphasis on Physical Concepts of Electronic Processes”, Academic Press, London, UK (2004).

40) G. G. Raju, “Dielectrics in electric fields”, M. Dekker inc. N.Y., (2003).

41) C. Kittel, “Introduction to solid state physics”, John Wiley and Sons, 8th ed., (2005).

42) S. B. Lang, “Sourcebook of Pyroelectricity”, Gordon & Breach, Science, London, (1974).

43) a) A. K. Jonscher, "Dielectric Relaxation in solids", Chelsea dielectric press, London, p. 214, (1983). b) A. K. Jonscher, “The “Universal” Dielectric Response: Part I”, Royal Holloway and Bedford New college, Surrey, U. K.

44) D. D. Eley, “Phthalocyanines as Semiconductors”, Nature, 162, 819, (1948).

45) J. Simon, J. J. Andre, J. M. Lehn, C. W. Rees, “Molecular Semiconductors: Photoelectrical Properties and Solar Cells”, Springer, Berlin, (1985).

46) L. Dignard-Bailey, M. L. Trudeau, A. Joly, R. Schulz, G. Lalande, D. Guay, J. P. J. Dodelet, “Graphitization and particle size analysis of pyrolyzed cobalt phthalocyanine/carbon catalysts for oxygen reduction in fuel cells”, Mater. Res., 9, 3203, (1994).

47) N. Kobayashi, Y. J. Nishiyama; “Catalytic electroreduction of molecular oxygen using iron or cobalt 4,4',4",4'"-tetracarboxyphthalocyanine”, Phys. Chem.89, 1167, (1985).

48) R. J. Jasinski, “A New Fuel Cell Cathode Catalyst”, Nature, 201, 1212, (1964).

49) P. Peumans, A .Yakimov; S. R. Forrest, “Small molecular weight organic thin-film photodetectors and solar cells”, J. Appl. Phys. 93, 3693, (2003).

50) C. Hamann, H. J. Hoehne, M. Naegler, **“**Parameters of lead phthalocyanine solar cells and their improvement”, Mater. Sci., 10, 105, (1984).

51) A. M. Hor, R. O. Loutfy, C. K. Hsiao, “Photovoltaic properties of cadmium sulfide/trivalent-metal phthalocyanine heterojunction devices”, Appl. Phys. Lett., 42, 165, (1983).

52) K. Muller, I. Paloumpa, K. Henkel, D. Schmeisser, “A polymer high-k dielectric insulator for organic field-effect transistors”, J. Appl. Phys., 98, 056104, (2005).

53) M. Madru, G. Guillaud, M. Al Sadoun, M. Maitrot, C. Clarisse, M. Le Contellec, J. J Simon, J. Chem. Phys. Lett., 142, 103, (1987).

54) M. Bouvet, A. Pauly, “Molecular based gas sensors –dans-” The Encyclopedia of Sensors, vol. 6 p. 227-270, American Scientific Publishers, (2006).

55) M. L. Rodriguez-Mendez, “Gas Sensing Properties of Phthalocyanines”, The Encyclopedia of Sensors, American Scientific Publishers, vol. 9, 111-134, (2005).

56) X. Zhang, C. Löwe, M. Wissler, B. Jähne, G. Kovacs, “Dielectric elastomers in actuator technology”, Adv. Eng. Mater. 7, 361, (2005).

57) Y. Bar-Cohen, “Electroactive Polymers (EAP) Actuators as Artificial Muscles Reality, Potential, and Challenges”, 2nd ed., SPIE, Bellingham, WA, (2004).

58) a) V. Bobnar, A. Levstik, C. Huang, Q. M. Zhang, “Intrinsic dielectric properties and charge transport in oligomers of organic semiconductor copper phthalocyanine”, Phys. Rev. B, 71, 041202 (2005). b) C. Huang, Q. M.Zhang, G. deBotton and K. Bhattacharya, “All-organic dielectric-percolative three-component composite materials with high electromechanical response”, Appl. Phys. Lett., 84, 4391, (2004). (c) V. Bobnar, A. Levstik, C. Huang, Q. M. Zhang, “Glass Dynamics in Electron-irradiated P(VDF-TrFE) Copolymer System”, Phys. Rev. Lett., 92, 047604, (2004). (d) C. Huang, Q. M. Zhang, J. Y. Li, M. Rabeony, “Colossal dielectric and electromechanical responses in self-assembled polymeric nanocomposites”, Appl. Phys. Lett., 87, 182901, (2005).

59) M. Martin, J. J. Andre, J. Simon, “Influence of dioxygen on the junction properties of metallophthalocyanine based devices”, J. Appl. Phys., 54, 2792, (1983).

60) K. Maex, M. R. Baklanov, D. Shamiryan, F. Iacopi,S. H. Brongersma,Z. S. Yanovitskaya, “Low dielectric constant materials for microelectronics”, J. Appl. Phys., 93, (2003).

61) K. Hayashi, S.Kawato, Y.Fujii, T. Horiuchi, K.Matsushige, “Effect of applied electric field on the molecular orientation of epitaxially grown organic films” Appl. Phys. Lett. 70, 1384-1386 (1997).

62) N. Shi, R. Ramprasad, “Dielectric properties of Cu-phthalocyanine systems from first principles”, Appl. Phys. Lett., 89, 102904, (2006).

63) R. D. Gould, A. K. Hassan, “AC electrical properties of thermally evaporated thin films of copper phthalocyanine”, Thin Solid Films, 223, 334, (1993).

64) P. Lunkenheimer, V. Bobnar, A. V. Pronin, A. I. Ritus, A. A.Volkov, A. Loidl, "Origin of apparent colossal dielectric constants", Phys. Rev. B, 66, 052105, (2002).

65) a) H. S. Nalwa, L. R. Dalton, P. Vasudevan, "Dielectric properties of copper-phthalocyanine polymer", Eur. Polym. J., 21, 943-947, (1985). b) N. Phougat, P. Vasudevan, H.S. Nalwa, "Handbook of low and High Dielectric Constant Materials and Their Applications", Academic Press, N. Y., vol.1, (1999). c) H. S. Nalwa, P. Vazudevan, "Dielectric properties of cobalt phthalocyanine", J. Matt. Sci Lett., 2, 22, (1983).

66) a) R. D. Hartman, "Hyperelectronic Polarization in Polymeric Semicondudors", proc. of the Okla. Acad. of sci., (1966). b) R. D. Hartman, H. A. Pohl, "Hyperelectronic polarization in macromolecular solids", J. Polymer Science, Part a-1-Polymer Chemistry 6, 1135, (1968). c) H. A. Pohl,"Nomadic polarization in quasi one dimensional solids", J. Chem. Phys., vol. 66, 4031-4040, (1971).

67) Q. M. Zhang, H. Li, M. Poh, F. Xia, Z.Y. Xu, H. Cheng, C. Huang, "An allorganic composite actuator material with a high dielectric constant", Nature, 419, 284, (2002).

68) R. Saha, B. K. Mandal, "New Copper Phthalocyanine Oligomers for High Dielectric Constant Polymer Films", J. Appl. Polym. Sci., 117, 122, (2010).

69) D. M. Opris, F. Nuesch, C. Lowe, M. Molberg, M. Nagel, "Synthesis, Characterization, and Dielectric Properties of Phthalocyanines with Ester and Carboxylic Acid Functionalities", Chem. Mater., 20, 6889–6896, (2008).

70) G. Mezei, A. R. Venter, J. W. Kreft, A. A. Urech, N. R. Mouch, "Monomeric, not tetrameric species are responsible for the colossal dielectric constant of copper phthalocyanine derived from pyromellitic dianhydride", RSC, Adv.**2**, 10466-10469, (2012).

71) R. Bechara, J. Petersen, V. Gernigon, P. Leveque, T. Heiser , V. Toniazzo , D. Ruch , M. Michel, "PEDOT:PSS-free organic solar cell susing tetrasulfonic copper phthalocyanine as buffer layer", Solar Energy Materials and Solar Cells; 98-482–485, (2012).

72) S. Schumann, R. A. Hatton, T. S. Jones, “Organic Photovoltaic Devices Based on Water-Soluble Copper Phthalocyanine”, J. Phys. Chem. C, 115, 4916–492, (2011).

73) J. W. Ryan, E. Anaya-Plaza, A. Escosura, T. Torres, E. Palomares, “Small molecule solar cells based on a series of water-soluble zinc phthalocyanine donors”, Chem. Com., 48, 6094-6096, (2012).

74) D.Wöhrle, "Phthalocyanines: Properties and Applications" Phthalocyanines in Polymer Phases. Inc, 55-132. VCH Publishers, Inc. N. Y., (1989).

75) A. L. Thomas, “Phthalocyanine Research and Applications”, CRC press, U.S.A, (1990).

76) A. N.Vzorov, L. G. Marzilli, R. W. Compans, D. W. Dixon, “Prevention of HIV-1 infection by phthalocyanines”, Antiviral Res., 59, 99-109, (2003).

77) C. P. Poole, F. J. Owens, “Introduction to nanotechnology”, John Wiley & Sons Inc., Hoboken, New Jersey, (2003).

78) M. M. AL-Amar, K. J. Hamam, G. Mezei, R. Guda, N. M. Hamdan, C. A. Burns, “A new method to improve the lifetime stability of small molecule bilayer heterojunction organic solar cells “, Sol. Energy Mater. Sol. Cells, 109, 270-274, (2013).

79) M. Guo, X. Yan, Y. Kwon, T. Hayakawa, M. Kakimoto, T. Goodson; “High Frequency Dielectric Response in a Branched Phthalocyanine”, J. Am. Chem. Soc., 128, 14820–14821, (2006).

80) S. N. Khan, “Electrospinning Polymer Nanofibers - Electrical and Optical Characterization”

81) H. Dong, S. Prasad, V. Nyame, W. Jones, “Sub-micrometer conducting polyaniline tubes prepared from polymer fiber templates”, Chem. Mater., 16, 371-373, (2004).

82) X. L. Wei, Y. Z. Wang, S. M. Long, C. Bobeczko, A. J. Epsteib, “Synthesis and physical properties of highly sulfonated polyaniline”, J. Am. Chem. Soc., 118, 2545 -2555, (1996).

83) B. C. Roy, M. D. Gupta, L. Bhowmik, J. K. Ray., “Studies on water soluble conducting polymer-Aniline initiated polymerization of m-aminobenzene sulfonic acid”, Synth. Met., 100, 233-236, (1999).

84) A. Mirmohseni, M. R. Houjaghan, "Synthesisand characterization of water-soluble conducting poly (3-amino-4-methoxybenzenesulfonic acid)", Mol. Cryst. Liq. Cryst., 484, 722-727, (2008).

85) Agilent Basics of Measuring the Dielectric Properties of Materials http://www3.imperial.ac.uk/pls/portallive/docs/1/11949698.PDF.

86) N. E. Bengtsson, P. O. Risman, "Dielectric properties of food at 3 GHz as determined by a cavity perturbation technique II: Measurements on food materials", J. Microwave Power, Vol. 6, No. 2, 107–123, (1971).

87) http://www.omega.com/temperature/z/pdf/z103.pdf., (2011).

88) J. Albani, "Principles and Applications of Fluorescence Spectroscopy", Blackwell, U.S.A (2007).

89) W. K. Metzger, R. K. Ahrenkiel, P. Dippo, J. Geisz, M. W. Wanlass, S. Kurt, "Time-Resolved Photoluminescence and Photovoltaics", NREL/CP-520-37028, (2005).

90) H. Gommans, S. Schols, A. Kadashchuk, P. Heremans, "Exciton Diffusion Length and Lifetime in Subphthalocyanine Films", J. Phys. Chem. C, 113, 2974–2979, (2009).

91) J. R. Lakowicz, "principles of fluorescence spectroscopy", 2nd ed., Kluwer academic, Plenum publisher, (1999).

92) T. Goodson, "Time-resolved spectroscopy of organic dendrimers and branched chromophores", Ann. Rev. Phys. Chem., 56, 581-603, (2005).

93) J. Huang, P. E. Miller, J. S. Wilson, A. J. de Mello, J. C. de Mello, D. D. C. Bradley, "Investigation of the effects of doping and post-deposition treatments on the conductivity, morphology, and work function of poly (3,4-ethylenedioxythiophene)/poly (styrenesulfonate) films", Adv. Funct. Mater., 15, 290, (2005).

94) F. Krebs, "Polymer photovoltaics: a practical approach", SPIE, (2008).

95) W. Umrath, "fundamentals of vacuum technology", Leybold vacuum, (2004).

96) R. D. Gould "D.C. Electrical measurements on evaporated thin films of copper phthalocyanine. Thin Solid Films", 125, 63, (1985).

97) A. M. Saleh, S. M. Hraibat, R. Kitaneh, M. M. Abu-Samreh, S. M. Musameh, "Dielectric response and electric properties of organic semiconducting phthalocyanine thin films", J. Semiconductors, 33, 8, (2012).

98) P. Sullivan, S. Heutz, S. M. Schultes, T. S. Jones, **"**Influence of codeposition on the performance of CuPc– C_{60} heterojunction photovoltaic devices", Appl. Phys. Lett., 84, 1210, (2004).

99) R. S. Kumar, K. Hariharan, "AC conductivity and electrical relaxation studies on 10CuI–60AgI–30V_2O_5 glasses", Mat. Chem. Phys, 60, 28, (1999).

100) J. Bao, M. L. Swicord, C. C. Davis, "Microwave dielectric characterization of binary mixtures of water, methanol, and ethanol", J. Chem. Phys., 104, 4441-4450, (1996).

101) J. Melcher, Y. Daben, G. Arlt, "Dielectric effects of moisture in polyimide", IEEE Trans. Elec. Insul., 24, 31-38, (1989).

102) S.Varaganti, G. Ramakrishna, "Dynamics of Interfacial Charge Transfer Emission in Small Molecule Sensitized TiO2 Nanoparticles: Is It Localized or Delocalized?", J. Phys. Chem. C, 114, 13917–13925, (2010).

103) M. Guo, X. Yan, T. Goodson, "Electron Mobility in a Novel Hyper-branched Phthalocyanine Dendrimer", Adv. Mat., 20, 4167–4171, (2008).

104) A. A. Bahgat, Y. M. Abou-Zeid, "Mixed alkali effect in the K_2O–Na_2O–TeO_2 glass system", Phys. Chem. Glasses, 42, (2001).

105) J. P. Zelina, C. K.Njue, J. F.Rusling, G. N. Kamau, M. Masila, J. Kibugu, "Influence of surfactant-based microheterogeneous fluids on aggregation of copper phthalocyanine tetrasulfonate", J. Porph. Phthalo., 3, 188-195, (1999).

106) P. J. Camp, A. C. Jones, R. K. Neely, N. M. Speirs, "Aggregation of copper (II) tetrasulfonatedphthalocyanine in aqueous salt solutions", J. Phys. Chem. A 106, 10725-10732 (2002).

107) Z. R. Li, H. Meng,"Organic Light-Emitting Materials and Devices", CRC press, (2007).

108) S. Han , W. S. Shin , M. Seo , D. Gupta , S. Moon, S. Yoo, “Improving performance of organic solar cells using amorphous tungsten oxides as an interfacial buffer layer on transparent anodes”, Organic Electronics, 10, 791–797, (2009).

109) H. Frohne, S. Shaheen, C. Brabec, D. Muller, N. S. Sariciftci, , K. Meerholz, “Influence of the anodic work function on the performance of organic solar cells“, Chem. Phys. Chem., 9, 795, (2002).

110) M. Muntwiler, Q. Yang, W. A. Tisdale, X. Y. Zhu, “Coulomb Barrier for Charge Separation at an Organic Semiconductor Interface”, PRL 101, 196403, (2008).

111) S. Rajaputra, S. Vallurupalli, V. P. Singh, “Copper phthalocyanine based Schottky diode solar cells”, J. Mater Sci. Mater. Electron, 18, 1147–1150, (2007).

112) J. C. Hummelen, B. W. Knight, F. Lepeq, F. Wudl, J. Yao, C. L. Wilkins, "Preparation and Characterization of Fulleroid and Methanofullerene Derivatives", J. Org. Chem., 60, 532–538, (1995).

113) E. Perzon, X.Wang, F. Zhang, W. Mammo, J. L. Delgado, P. Cruz, O. Inganas, F. Langa, M. R. Andersson, “Design, Synthesis and Properties of Low Band Gap Polyfluorenes for Photovoltaic Devices”, Synthetic Metals, 154, 53-56, (2005).

114) M. Al-lbrahim, O. Ambacher, “Effects of solvent and annealing on the improved performance of solar cells based on poly(3-hexylthiophene): Fullerene”, Appl. Phys. Lett., 86, 201-120, (2005).

115) W. U. Huynh, J. J. Dittmer, A. P. Alivisatos, “Hybrid Nanorod-Polymer Solar Cells”, Science, 295, 2425-2427, (2002).

116) F. C. Krebs, “Stability and Degradation of Organic and Polymer Solar Cells”, John Wiley, UK, (2012).

117) M. M. AL-Amar, K. J. Hamam, G. Mezei, R. Guda, C. A. Burns, “Stability of unencapsulated ITO/PEDOT: PSS/CuPc/PTCDI/Ag bilayer heterojunction cells”, Sol. Energy Mater. Sol. Cells, submitted, (2013).

118) K. Kawano, R. Pacios, D. Poplavskyy, J. Nelson, D. D. C. Bradley, J. R. Durrant, "Degradation of organic solar cells due to air exposure", Sol. Energy Mater. Sol. Cells, 90, 3520–3530, (2006).

119) X. Xi, F. Li, Q. Meng, Y. Ding, J. Ji, Z. Shi, G. Li, "The investigation of the stability and optimal encapsulate on time for ITO/CuPc/C_{60}/Al bilayer cells", Sol. Energy Mater. Sol. Cells, 94924–929, (2010).

120) Q. L. Song, F.Y. Li, H. Yang, H. R. Wu, X. Z. Wang, W. Zhou, J. M. Zhao, X. M. Ding, C. H. Huang, X. Y. Hou, "Small-molecule organic solar cells with improved stability", Chem. Phys. Lett., 416, 42–46, (2005).

121) M. Tavakkoli , R. Ajeian, M. N. Badrabadi , S. S. Ardestani, S. M. H. Feiz, K. E. Nasab, "Progress in stability of organic solar cells exposed to air", Sol. Energy Mater. Sol.Cells, 95, 1964–1969, (2011).

122) C. J. Brabec, J. A. Hauch, P. Schilinsky, C. Waldauf, "Production aspects of organic photovoltaics and their impact on the commercialization of devices", MRS, Bull., 30; 50–52, (2005).

123) F. C. Krebs, "Air stable polymer photovoltaics based on a process free from vacuum steps and fullerenes", Sol. Energy Mater. Sol. Cells, 92, 715–726, (2008).

124) F. C. Krebs, S. A. Gevorgyan, B. Gholamkhass, "A round robin study of flexible large-area roll-to-roll processed polymer solar cell modules", Sol. Energy Mater. Sol. Cells, 93, 1968–1977, (2009).

125) S. Chambon, A. Rivaton, J. L. Gardette, M. Firon, L. Lutzen, "Ageing of organic solar cells: chemical studies of the degradation of MDMO-PPV", J. Polym. Sci. Part A, Polym. Chem., 45, 317, (2007).

126) F. C. Krebs, H. Spanggaard, "Significant improvement of polymer solar cell stability", Chem. Mater., 17, 5235–5237, (2005).

127) M. Manceau, A. Rivaton, J. L. Gardette, S. Guillerez, N. Lemaître, " The mechanism of photo- and thermooxidation of poly(3-hexylthiophene) (P3HT) reconsidered", Polym. Degrad. Stab., 94, 898, (2009).

128) D. E. Motaung, G. F. Malgas, C. J. Arendse, "Insights into the stability and thermal degradation of P3HT:C60 blended films for solar cell applications", J. Mater. Sci., 46, 4942, (2011).

129) M. Jorgensen, K. Norrman, S. A. Gevorgyan, T. Tromholt, B. Andreasen, F. C. Krebs, "Stability of Polymer Solar Cells" Adv. Mater., 24, 580-612, (2012).

130) J. Xue, S. Uchida, B. P. Rand, S. R. Forrest, "4.2% efficient organic photo- voltaic cells with low series resistances", Appl. Phys. Lett., 84, 3013–3015, (2004).

131) P. Peumans, V. Bulovic, S. R. Forrest, "Efficient photon harvesting at high optical intensities in ultrathin organic double-heterostructure photovoltaic diodes", Appl. Phys. Lett., 76, 2650–2652, (2000).

132) V. Bulovic, S. R. Forrest, "Study of localized and extended excitons in 3,4,9,10-perylenetetracarboxylic dianhydride (PTCDA) II. Photocurrent response at low electric fields", Chem. Phys. 210, 13, (1996).

133) I. G. Hill, A. Kahn, Z. G. Soos, R. A. Pascal, "Charge-separation energy in films of π-conjugated organic molecules", Chem. Phys. Lett., 327, 181, (2000).

134) A. Kahan, N. Koch,W. Gao, "Electronic Structure and Electrical Properties of Interfaces between Metals and π-Conjugated Molecular Films", J. polymer science part b,41, 2529, (2003).

135) B. Zimmermann, M. Glatthaar, M. Niggermann, M. Riede, A. Hinsch, "Organoc solar cells using inverted layer sequences", Thin Solid Films 493, 170, (2005).

136) S. Gunes, H. Neugebauer, N. S. Sariciftci, "conjugated polymer-based organic solar cells", Chem. Rev Lett.,107, 1324-1338, (2007).

137) B. P. Rand, D. P. Burk, S. R. Forrest, "Offset energies at organic semiconductor heterojunctions and their influence on the open-circuit voltage of thin-film solar cells", Phys. Rev. B, 75, 115327, (2007).

138) M. C. Scharber, D. Mühlbacher, M. Koppe, P. Denk, C. Waldauf, A. J. Heeger, C. J. Brabec, "Design Rules for Donors in Bulk-Heterojunction Solar Cells-Towards 10 % Energy-Conversion Efficiency", Adv. Mater., 18, 789, (2006).

139) Q.L. Song, F.Y. Li, H. Yang, H.R. Wu, X.Z. Wang, W. Zhou, J.M. Zhao,X.M. Ding, C.H. Huang, X.Y. Hou, "Small-molecule organic solar cells with improved stability",
Chem. Phys. Lett., 416, 42–46, (2005).

140) P. Peumans, S. R.Forrest, "Very-high-efficiency double-heterostructure copper phthalocyanine/C60 photovoltaic cells", Appl. Phys. Lett., 80, 338, (2002).

141) S. Heutz, P. Sullivan, B. M. Sanderson, S. M. Schultes, T. S. Jones, "Influence of molecular architecture and intermixing on the photovoltaic, morphological and spectroscopic properties of CuPc–C_{60} heterojunctions", Sol. Energ. Mater. Sol. Cells, 83, 229, (2004).

142) http://homes.nano.aau.dk/kp/Ellipsometry/main.pdf. J. Jung, J. Bork,T. Holmgaard, N. A. Kortbek, Kjeld Pedersen, "The Ellipsometry", Aalborg University, institute of Physics and nanotechnology, (2013).

143) H. G. Tompkins, E. A. Irene, "Handbook of ellipsometry", William Andrew, (2005).